UNIVERSITÀ DI PISA

Dottorato di Ricerca in Fisica - XIV ciclo

Tesi di Dottorato

Seismic Isolation for the Test Masses of the VIRGO Gravitational Wave Antenna

Author
Dott. Claudio Casciano

Supervisor
Prof. Adalberto Giazotto

Ottobre 2002

Alla mia famiglia

Contents

Introduction

The VIRGO project is an Italian–French collaboration for the realization of an interferometric antenna for gravitational wave detection and observation. Gravitational waves are predicted by Einstein's theory of general relativity and, up to now, they remain undetected. Nevertheless, the observation of PSR1913+16 binary pulsar has provided an indirect evidence of gravitational wave existence: the orbital period decay rate is in good agreement with general relativity predictions about the energy and angular momentum loss due to gravitational radiation emission.

The detection of gravitational waves is extremely difficult because of the weakness of their coupling with matter. Only in the last decade, the realization of detection apparatus with unprecedent sensitivity in a wide band of frequencies, from a few tens of Hz to some kHz, has become conceptually possible. The basic idea is to detect the passing through of a gravitational wave by measuring the small displacements induced on the mirrors of a suspended interferometer with a few kilometers long arms.

Among the interferometric gravitational wave detectors which will be operating in a few years, VIRGO is the only one whose optical components are being suspended by means of sophisticated devices capable of isolating the interferometer from the seismic noise. The vibrations of the soil, either natural or caused by human activities, if not attenuated, are transmitted to the interferometer mirrors throughout their suspensions, so inducing spurious displacements capable to mask the weak effects of a gravitational wave. Since such vibrations are larger at low frequencies, the sensitivity of a ground based antenna is limited in that spectral region where several gravitational signals are expected to be emitted by pulsars and coalescing binaries. Seismic attenuation allows to extend the detection band down to a few Hz.

For about ten years, Pisa VIRGO group has been engaged in the development of such suspension systems, called *superattenuators*. The below described work of thesis is part of this research field. At present, four superattenuators are working to suspend the optics of the interferometer central part, where the laser beams cross each other. The assembling of the last two suspension systems, those for the two end mirrors of the Fabry–Perot cavities, is in progress and will be terminated within the end of 2002.

This thesis concerns the development and the realization of three items of the complex suspension system:

1. **The magnetic antispring** allowing the reduction of the vertical resonant frequencies of the superattenuator.

2. **The absorption devices** designed to attenuate the internal modes.

3. **The steel blade springs** for the vertical attenuation.

The thesis is divided into 9 chapters. Chapter 1 and 2 are an introduction to the theory of gravitational waves, expected sources and interferometric detection techniques. In chapter 3 a description of the VIRGO apparatus and its expected sensitivity are found. In chapter 4 we describe in detail the superattenuator and its performances. The experimental work done is developed in the remaining chapters. Chapter 5 concerns the characterization of the magnetic antispring. The absorption devices for the internal modes are the subject of chapter 6. The creep problem related to the blade springs and its solution are described in chapter 7. Finally, in chapter 8 and 9 we show some important results about the performances of short and tall superattenuators, respectively.

Chapter 1

Gravitational waves

The description of an apparatus for detecting and studying gravitational waves cannot leave out of account from answering to a stringent question: what are gravitational waves? An exhaustive and formally rigorous answer is deferred to general relativity treatments[1, 2, 3]; in this thesis, since its experimental contents, we will just delineate some of the fundamental steps that lead to the definition of currently used quantities of gravitational wave physics.

The existence of gravitational waves is predicted by Einstein's theory of general relativity[4]. The basic idea is that the presence of mass curves the surrounding space–time and that sudden variations of mass distribution induce perturbations of the metrics which propagate at the speed of light: the gravitational waves.

Because gravitational waves weakly interact with matter, they can travel throughout very dense regions without suffering any alteration. Therefore, their detection, beside providing a further proof of the theory of relativity, would open a new investigation channel especially for those regions of the universe that are inaccessible through electromagnetic emission observation.

In order to realize a detector we need to estimate the order of magnitude of the effect that gravitational waves produce hence, it is opportune to remind some results of Einstein's general relativity.

1.1 Gravitational radiation

According to the theory of general relativity, Einstein's field equations determinate the form of the metric tensor $g_{\mu\nu}$ which describes the space–time metrics. In absence of gravitational field it is reduced to the Minkowski tensor

$$\eta_{\mu\nu} = \mathrm{Diag}\left\{-1, 1, 1, 1\right\}. \tag{1.1}$$

Einstein's equations are non linear and have no analytical solutions. Nevertheless, in the weak field approximation, we can treat them in a pertubative way. The metrics in regions of space–time where the gravitational field of astrophysical objects is weak, can be written as the Minkowski tensor plus a small perturbation describing the deviation from a flat space–time:

$$g_{\mu\nu} \simeq \eta_{\mu\nu} + h_{\mu\nu}, \tag{1.2}$$

with $|h_{\mu\nu}| \ll 1$. To the first order with respect to $h_{\mu\nu}$ the field equations are linear. With a suitable choice of gauge (*harmonic gauge*), Einstein's equations assume the familiarly form of wave equations

$$\left(\nabla^2 - \frac{1}{c^2}\frac{\partial^2}{\partial t^2}\right) h_{\mu\nu} = 0, \tag{1.3}$$

which describe the perturbation $h_{\mu\nu}$ as a wave propagating at speed c. The freedom in the choice of the coordinate system can be used again to impose the tensor $\mathbf{h}$ to be transverse and traceless (*TT gauge*). In this gauge the coordinates are marked by the world lines of freely falling masses, that is, the coordinates of freely falling test masses are constant.

Assuming $\hat{z}$ as the propagation direction, one can write the plane wave solutions of (1.3) in the form:

$$h^{TT}_{\mu\nu}(z,t) = (h_+ e^+_{\mu\nu} + h_\times e^\times_{\mu\nu}) e^{i(\omega t - kz)}, \tag{1.4}$$

where the tensor $\mathbf{h}$ has been divided into two independent polarization states of amplitude h_+ and $h_\times$, respectively, and represented by the tensors

$$e^+ = \begin{pmatrix} 0 & 0 & 0 & 0 \\ 0 & 1 & 0 & 0 \\ 0 & 0 & -1 & 0 \\ 0 & 0 & 0 & 0 \end{pmatrix} \quad \text{and} \quad e^\times = \begin{pmatrix} 0 & 0 & 0 & 0 \\ 0 & 0 & 1 & 0 \\ 0 & 1 & 0 & 0 \\ 0 & 0 & 0 & 0 \end{pmatrix}.$$

From these results we can conclude that, for the characterization of a gravitational wave, five parameters are necessary: two angles for the propagation direction, the amplitude of the two independent polarizations and their relative phase.

1.2 Generation of gravitational waves

The emission of gravitational waves is associated to mass acceleration as the emission of electromagnetic radiation is associated to charged particle acceleration. In the linear approximation regime, as in electromagnetism, if the size of the source is small compared to the wavelength and to the distance from the observation point, we can solve the non homogeneous Einstein's equations through a multipolar expansion of the emitted radiation.

The momentum and angular momentum conservation laws make vanishing the contribution of the equivalent of electric dipole and magnetic quadrupole[7] hence, the first term of the expansion which can be not vanishing is associated to the variation of the quadrupole moment tensor of a mass distribution, defined as:

$$Q_{ij} = \int_V \rho(\vec{x}) \left(x_i x_j - \frac{1}{3}|\vec{x}|^2 \right) dV, \tag{1.5}$$

where $\rho(\vec{x})$ is the mass distribution and we have supposed that the involved velocities are not relativistic. The amplitude at distance r of the gravitational wave emitted is given by[7]:

$$h_{ij}^{TT} = \frac{2G}{rc^4} \left[\frac{d^2 Q_{ij}^{TT}}{dt^2} \right]_{(t-\frac{r}{c})}, \tag{1.6}$$

where G is the gravitational constant and the acceleration of quadrupole moment is taken at *retarded time* $t - r/c$. The factor $G/c^4 \sim 10^{-44}$ in MKS units, justifies the assumption about the weakness of gravitational waves. Moreover, it comes out from (1.6) that gravitational waves cannot be emitted in spherically symmetric motion of matter.

The power emitted in form of gravitational radiation (luminosity) is:

$$\mathcal{L} = \frac{1}{5}\frac{G}{c^5} \langle \dddot{Q}_{ij} \dddot{Q}_{ij} \rangle, \tag{1.7}$$

where $\langle\rangle$ indicates the time average over several periods of the wave or over the wave burst duration. Equation (1.7) can be used to estimate the luminosity of an astrophysical source of mass M and characteristic radius R. Let T be the characteristic evolution time of the source and let ϵ be a factor measuring the asymmetry in the mass distribution. The quadrupole moment is roughly $Q \sim \epsilon M R^2$ and the luminosity is then:

$$\mathcal{L} \sim \epsilon^2 \frac{G}{c^5} \frac{M^2 R^4}{T^6}. \tag{1.8}$$

The factor G/c^5 strongly suppresses the gravitational emission. On the other hand, by expressing the source mass in terms of the Schwarzschild radius: $R_S = 2GM/c^2$ and introducing a characteristic speed $v = R/T$, the (1.8) reduces to:

$$\mathcal{L} \sim \epsilon^2 \mathcal{L}_0 \left(\frac{R_S}{R}\right)^2 \left(\frac{v}{c}\right)^6, \tag{1.9}$$

where we find that $\mathcal{L}_0$ is now $c^5/G = 3.2 \times 10^{52}$ W! In spite of our hypothesis of weak fields and slowly moving matter, this surprising result points out the relevance of gravitational waves emission for compact and relativistic objects.

1.3 Astrophysical sources

From the previous sections, in particular from equation (1.8), one can deduce how it is impracticable to construct a laboratory source of detectable gravitational waves. Astrophysical processes involving high acceleration of a great amount of matter are the sources of gravitational waves best accessible to detection. The predictions about the shape of such emissions and the number of events depend on the theoretical models adopted for describing each of these processes and are affected by large uncertainties.

According to their time behaviour, gravitational waves are usually classified into three categories: *burst*, *periodic waves* and *stochastic waves*. Similarly, it happens for the respective astrophysical sources[8].

1.3.1 Burst sources

Bursts are waves which last for only a few cycles or at most for times short compared to a typical observation run. This kind of gravitational signals are expected to be emitted in *supernova* explosions. Some years ago supernovæ were believed to be the gravitational wave sources most likely to be detected. Today it is clear that the theoretical models of emission in a stellar collapse are affected by serious uncertainties due to the approximation used into the numerical codes and to the wide range of possible initial conditions.

The intensity of the emitted radiation depends mostly on the amount of the stellar mass converted into gravitational waves and the non–spherical symmetry of the collapse dynamics. Indicating with ΔE the total energy radiated and with f the characteristic frequency (the inverse of the collapse time), the amplitude of the gravitational wave is[8]:

$$h \approx 2.7 \times 10^{-20} \left(\frac{\Delta E}{M_{\odot} c^2}\right)^{\frac{1}{2}} \left(\frac{1 \text{ kHz}}{f}\right)^{\frac{1}{2}} \left(\frac{10 \text{ Mpc}}{r}\right), \tag{1.10}$$

where r is the distance from the Earth and $M_{\odot}$ is the mass of the Sun. The rate of occurrence of supernovæ in our Galaxy is roughly three per century; out to the distance of the center of Virgo cluster of galaxies (10 Mpc) several per year. This cluster of hundreds of galaxies in the Virgo constellation is a good candidate to gravitational wave emission since an enormous amount of stars is localized, astronomically speaking, in a relatively small range of distances.

Another important process expected to involve emission of bursts is the *coalescence of compact binaries.* In binary systems formed by compact objects like neutron stars or black holes, the energy loss due to gravitational radiation reaction could be sufficient to drive the two bodies into coalescence in time less than the age of the universe. As the two bodies spiral together, they emit periodic gravitational waves (*coalescence chirp*) with a frequency that sweeps towards a maximum of some kHz immediately before coalescing. Probably, the process ends with the formation of an excited and asymmetric black hole also emitting gravitational waves.

By the way, it is important to notice that the only, though indirect, experimental evidence of gravitational radiation comes from a compact binary system. The orbital parameters of PSR1913+16, a pulsar moving in the strong gravitational field of a dark companion, have been accurately determined by measuring the Doppler shift of the radio pulses coming from the system: the orbital period rate of decay is in good agreement with general relativity predictions about the energy and angular momentum loss due to gravitational radiation emission[5, 6]. Unfortunately, detecting the gravitational waves emitted by this system is a hopeless attempt for a realistic ground based antenna since the orbital period is of about 8 hours: as it will be shown in the following, the sensibility of such detectors is limited by the seismic noise below few Hz. The system is expected to coalesce in 3.5×10^8 years.

In the Newtonian part of the frequency sweep, $f \ll f_{max}$, the amplitude of the wave is easily computed from the quadrupole formalism[8]; if M and μ indicate the total mass and the reduced mass of the system, respectively, and r is the distance from the source, one can find:

$$h \approx 10^{-23} \left(\frac{M}{M_\odot}\right)^{\frac{2}{3}} \left(\frac{\mu}{M_\odot}\right) \left(\frac{f}{100\ \text{Hz}}\right)^{\frac{2}{3}} \left(\frac{100\ \text{Mpc}}{r}\right), \tag{1.11}$$

where $M_\odot$ is the solar mass and f is the frequency of the signal, that is twice the orbital frequency. Moreover, the time τ the signal spends in the vicinity of the frequency f, defined as the ratio $f/(df/dt)$, is given by:

$$\tau \approx 7.8 \left(\frac{M_\odot}{M}\right)^{\frac{2}{3}} \left(\frac{M_\odot}{\mu}\right) \left(\frac{100\ \text{Hz}}{f}\right)^{\frac{8}{3}} \text{ s.} \tag{1.12}$$

As it will be shown in the next chapter, the sensibility of a detector at a certain frequency is proportional to the square root of the observation time. Equation (1.12) shows that the time we can observe the signal at a frequency f increases as f decreases, thus the gravitational signals coming from coalescing binaries can be detected also in the low frequency region in spite of their lower amplitude.

The estimated event rate for coalescing neutron stars and black holes of a few solar masses at 100 Mpc, is some unit per year. Bursts can be generated in other processes like the collapse of a star or a cluster of stars to form a black hole or the fall of stars or small black holes into supermassive black holes. It is important to stress that all this processes could be, in principle, strictly connected with other observable phenomena like light emissions and neutrinos or gamma ray bursts.

1.3.2 Periodic sources

Periodic sources emit gravitational signals whose frequency remains constant over a long period with respect to the observation time. *Pulsars* could be such kind of sources. A pulsar is interpreted as a rotating neutron star with magnetic moment

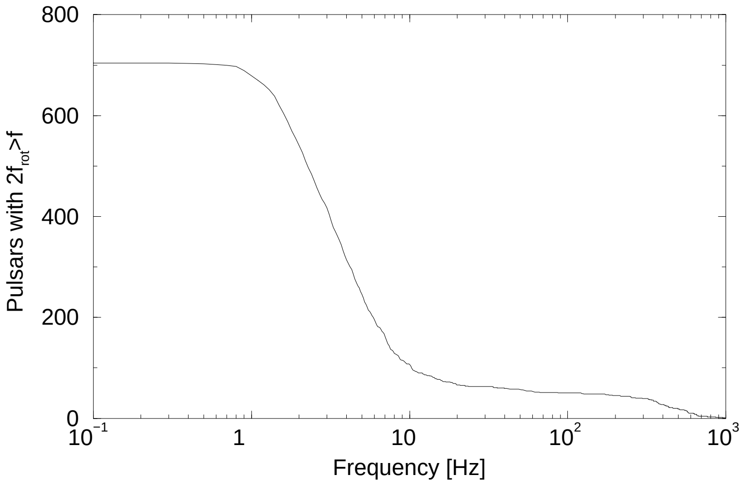

Figure 1.1: *The integrated distribution of 703 galactic pulsars with to respect to the gravitational wave emission frequency[10].*

not parallel to the rotation axis. According to (1.6), deviations from axisymmetry in distribution of mass can be responsible of the emission of gravitational waves. An estimation of the amplitude of this waves is given by[8]:

$$h \approx 7.7 \times 10^{-20} \varepsilon \left(\frac{I_{zz}}{10^{45}\text{g cm}^2} \right) \left(\frac{f}{10\text{Hz}} \right)^2 \left(\frac{10\text{kpc}}{r} \right), \tag{1.13}$$

where I_{zz} is the moment of inertia of the star about its rotation axis and ε is its "gravitational ellipticity" in the equatorial plane. An upper limit for this ellipticity is suggested to be $\sim 10^{-4}$ ([9] and references therein).

The gravitational waves emitted by these sources are weak but the Signal–to–Noise Ratio can be increased by integrating the signal for a long time. Moreover, it is possible to go up to the polarization state and to the origin direction of the observed signal by exploiting the variations of the antenna orientation due to the Earth motion. It is a good feel that in our Galaxy there are 10^6 pulsars and, among these, thousands are candidate to emit gravitational waves with frequencies varying from fraction of Hz to more than 100 Hz (see fig. 1.1).

Periodic gravitational signals are also emitted by binary stars and, if these are visible, all the parameters that determine the emission of gravitational waves can be evaluated by means of electromagnetic measurements. The amplitude of these periodic waves is given by an equation very similar to that for coalescing binaries in newtonian phase:

$$h \approx 8.7 \times 10^{-21} \left(\frac{M}{M_{\odot}}\right)^{\frac{2}{3}} \left(\frac{\mu}{M_{\odot}}\right) \left(\frac{100\ \mathrm{pc}}{r}\right) \left(\frac{f}{10^{-3}\ \mathrm{Hz}}\right)^{\frac{2}{3}}, \tag{1.14}$$

where M and μ are the total and the reduced mass of the system, respectively, $M_{\odot}$ is the solar mass, f the frequency of the signal (twice the orbital one) and r is the distance from the source.

Unfortunately, ordinary binaries have orbital periods not shorter than one hour and correspondent frequencies of emitted gravitational waves lower than 10^{-3} Hz. As mentioned above (and shown in next chapter), the detection of signals with so much low frequency is not achievable by ground based antennæ because of the seismic noise.

1.3.3 Stochastic background

The stochastic gravitational radiation consists of randomly superimposed individual components which form an isotropic background. The possible sources are several: neutron stars, binary stars, pregalactic population of massive stars and unknown sources plus a probable relic background of cosmological origin[8].

Probably, a stochastic signals that could be detected by a ground based interferometric antenna is emitted by the about 10^6 neutron stars grouped in the center of the Galaxy; their incoherent noise would be modulated with a period of 12 hours since the effect of the Earth rotation on the antenna orientation and thus would become observable.

1.4 Detection of gravitational waves

The experimental search for cosmic gravitational waves started with Joseph Weber[11] in the sixties. He used, as detectors in coincidence, two *resonant bars* laying in two different sites of USA. A resonant bar detector is essentially a suspended cylinder, about one ton weight, whose main internal mode of oscillation is excited by the impinging gravitational wave. A transducer transforms the small vibrations of the test mass in electric signals. Once reduced all the sources of noise, this kind of detector is efficient only in a narrow band of frequency around its main resonant frequency (typically of the order of one kHz).

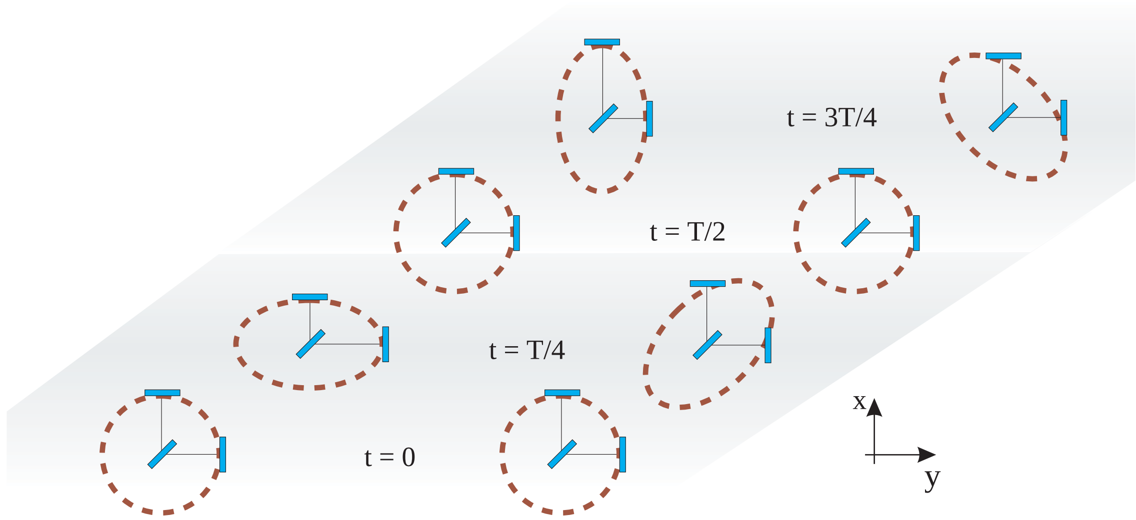

Figure 1.2: *Laboratory view of the effect over a circle of freely falling test masses, located in the x-y plane, of a "+" polarized (on the left) and a "×" polarized (on the right) gravitational wave of period T, propagating in the z direction. A Michelson interferometer, whose beam splitter is placed to the center of the circle and whose two end mirrors are along the axes x and y, is also shown.*

Considerable improvements have been done since Weber's first detector to enhance the sensitivity, till to get over, in narrow band, the expected level for the *interferometric antennæ*. These kind of newly conceived detection apparatus are the aim of several research projects all over the world. VIRGO is one of these. The working principle of an interferometric detector is described below.

Let us consider a "+" polarized gravitational plane wave of frequency f propagating in the z direction. According to (1.2) and (1.4), the metric element is written:

$$ds^2 = -c^2dt^2 + [1 + h(z,t)]\, dx^2 + [1 - h(z,t)]\, dy^2 + dz^2. \tag{1.15}$$

Suppose now to have a Michelson interferometer whose beam splitter is placed in the origin of the reference frame. Its two end mirrors lie at a distance L along the x and y axis, respectively. Let the optics of the interferometer be freely falling masses. For a photon $ds^2 = 0$ holds, hence it is possible to calculate from (1.15) the time the light takes to complete a round trip in each arm of the interferometer. In the x arm the light travel time from the beam splitter to the end mirror is:

$$\tau_x^{(1)} = \int_0^{t_1} dt = \frac{1}{c}\int_0^L \sqrt{1 + h(t)}dx \simeq \frac{1}{c}\int_0^L \left(1 + \frac{1}{2}h(t)\right) dx. \tag{1.16}$$

In the same way, the return trip takes a time

$$\tau_x^{(2)} \simeq \frac{1}{c}\int_L^0 \left(1+\frac{1}{2}h(t)\right) dx. \tag{1.17}$$

The two integrals can be easily calculated by replacing $h(t)$ with $h_0 e^{i2\pi ft}$ and remembering that $t = x/c$ in (1.16) and $t = (2L-x)/c$ in (1.17). Hence, the resulting travel time is:

$$\tau_x = \tau_x^{(1)} + \tau_x^{(2)} = \tau_0 + \frac{h_0}{i4\pi f}\left[e^{i2\pi f\tau_0} - 1\right], \tag{1.18}$$

where $\tau_0 = 2L/c$ is the *classical* travel time for a complete round trip.

Along the y axis the light picks the effect of $h_{22} = -h_{11}$ and one gets:

$$\tau_y = \tau_0 - \frac{h_0}{i4\pi f}\left[e^{i2\pi f\tau_0} - 1\right]. \tag{1.19}$$

For low frequency wave ($f\tau_0 \ll 1$), the perturbation h can be considered constant during the light round trip, so the second term in right hand side of (1.18) and (1.19) can be approximated to $h\tau_0/2$.

From the point of view of an observer in the laboratory, the variation of travel times can be interpreted as a variation in the arms length due to the impinging gravitational wave (see fig. 1.2). In the low frequency approximation we can write:

$$L_x(t) = \frac{1}{2}c\tau_x = L\left(1 + \frac{h(t)}{2}\right) \tag{1.20}$$

for the x arm and

$$L_y(t) = \frac{1}{2}c\tau_y = L\left(1 - \frac{h(t)}{2}\right) \tag{1.21}$$

for the y one.

When the two waveforms arrive to the the beam splitter they are thus "out of sync" and a photodiode at the output of the interferometer would measure a phase variation

$$\delta\phi(t) = \frac{4\pi L}{\lambda}h(t)e^{i\pi f\tau_0}\frac{\sin(\pi f\tau_0)}{(\pi f\tau_0)}, \tag{1.22}$$

where λ is the laser wavelength.

From the above description it is clear that an interferometer can be used as a gravitational wave detector. The interferometer response is plotted in fig. 1.3 as a

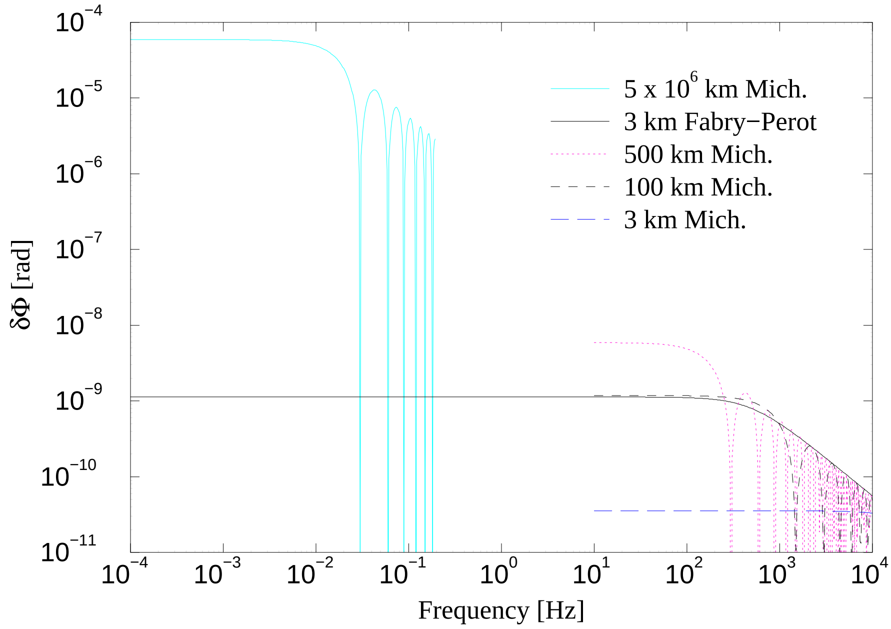

Figure 1.3: *Phase response of an interferometer to gravitational waves of fixed amplitude* 10^{-21}, *for different lengths of the arms. The phase shift increases with increasing arms length, at the cost of a bandwidth reduction. The performance of a 3 km Fabry–Perot (FP) interferometer like VIRGO (see next chapter) is comparable to that of a 100 km Michelson. The response of a* 5×10^6 *long Michelson (like the forthcoming space interferometer LISA[29]) is also shown.*

function of the impinging gravitational wave frequency: the interferometric transducer acts as a low pass filter starts attenuating at frequencies $f \sim c/2L$, that is when the period of the wave is comparable to the travel time τ_0. For low frequency wave the interferometer response is flat:

$$\delta\phi(t) = \frac{4\pi L}{\lambda} h(t). \tag{1.23}$$

The latter equation shows straightforwardly that the longer the arms of the interferometer, the bigger the phase shift due to a gravitational wave.

Chapter 2

Interferometric antennæ

The newly conceived *interferometric antennæ* show a wide band sensitivity. They are indeed designed for detecting gravitational signals with frequencies ranging from a few Hz to some kHz. The difficulties in realizing such an apparatus can be summarized by a single, astonishing number: 10^{-18} meters! It is the order of magnitude of the mirror displacements when a typical impulsive gravitational signal of extragalactic origin, whose amplitude is expected to be $h \sim 10^{-21}$, impinges an interferometer with 3 km long arms, like VIRGO.

In principle, what happens is described in the last section of the previous chapter. The VIRGO interferometer has vertically suspended optical components and the gravitational wave effects are measurable on the horizontal plane. Beside the reduction of the frequency band accessible to the detection, the suspension transmits to the mirrors the ground vibrations, so limiting the interferometer sensitivity. Other sources of noise are bound to the electronics, to the laser source, to the mechanics and thermodynamic characteristics of all the components of the apparatus and, last but not least, to the variation of local gravitational field.

It is well understood how extending the detection band and, at the same time, keeping the noise level reasonably low, means remarkable scientific and technological efforts but represents also a challenging and ambitious goal.

2.1 The suspended interferometer

Let us consider a test mass m suspended to a rigid structure by means of a thin wire of length l, i.e. a simple pendulum. For small oscillations, the well known equation of motion of the mass m is:

$$m\ddot{x} + \frac{mg}{l}x = F_{ext}(t), \tag{2.1}$$

where F_{ext} is an external force applied to the the mass and we are neglecting the dissipation term. In the frequency domain the solution is given by:

$$\hat{x}(\omega) = \frac{\hat{F}_{ext}(\omega)/m}{\omega_0^2 - \omega^2}, \tag{2.2}$$

where $\omega_0 = \sqrt{g/l}$ holds. For frequencies $\omega \gg \omega_0$ this equation becomes:

$$m\omega^2\hat{x}(\omega) + \hat{F}_{ext}(\omega) \simeq 0 \tag{2.3}$$

and, getting back to the time domain, we find:

$$m\ddot{x} \simeq F_{ext}(t) \tag{2.4}$$

that is, the mass responds to the external force as it was free.

In section 1.4 we calculated the effect of a gravitational wave on a Michelson interferometer with freely falling optics. Equation (2.4) shows that a ground based interferometer, whose optical components are suspended to form pendulums, behaves like a freely falling one for frequencies of the impinging gravitational wave above the pendulum resonant frequency.

Above a certain frequency, the phase response of a suspended interferometric receiver is described by the equation (1.22) for a gravitational waves propagating in the vertical (z) direction and with polarization axes parallel to the arms of the interferometer. If the gravitational wave is coming from a generic direction picked out by the two angles θ and φ and with polarization axes rotated at an angle ψ relative to the plane $\varphi = const$, as sketched in fig. 2.1, in the equation (1.22) $h(t)$ has to be replaced by the factor[12]

$$[F_+\left(\theta, \varphi, \psi\right) h_+(t) + F_\times\left(\theta, \varphi, \psi\right) h_\times(t)],$$

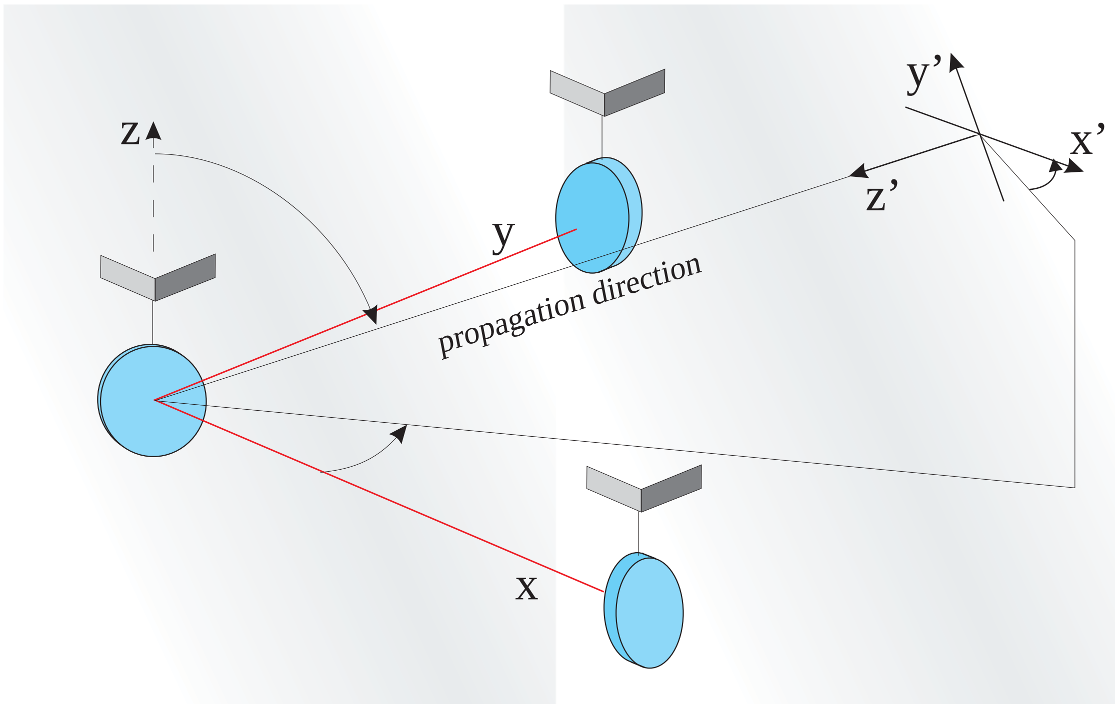

Figure 2.1: *The angles θ, φ and ψ that characterize the propagation and the detection of a gravitational wave.*

where:

$$
\begin{aligned}
F_{+}(\theta,\varphi,\psi) &= \tfrac{1}{2}\left(1+\cos^2\theta\right)\cos 2\varphi\cos 2\psi - \cos\theta\sin 2\varphi\sin 2\psi \\
F_{\times}(\theta,\varphi,\psi) &= \tfrac{1}{2}\left(1+\cos^2\theta\right)\cos 2\varphi\sin 2\psi - \cos\theta\sin 2\varphi\cos 2\psi .
\end{aligned}
\tag{2.5}
$$

From equations (2.5) we can deduce that the interferometer, even if it has a fixed orientation, can detect gravitational waves propagating in whatever direction except the ones along both the bisector of the angle formed by the two arms and its perpendicular ($\theta = \pi/2, \varphi = \pm\pi/4$ rad).

2.2 Noise in an interferometric antenna

Several sources of noise can introduce spurious signals capable to mask the weak effects due to an impinging gravitational wave. Some of them affect the position of the optical components (*displacement noise*), others are intrinsic noises of the read–out system (*phase noise*). Anyhow, they affect the phase shift recorded by the photodiode at output of the interferometer.

In order to compare it to the expected signal $h_S(t)$, one can consider the contribution of the noise to the phase shift as well as it was due to a fictitious gravitational wave of amplitude $h_N(t)$. In the following, we will refer to this as the *equivalent strain noise*. Since noise has a stochastic behaviour, it is better to describe it in terms of its *power spectral density* (or simply *spectrum*):

$$S_N(f) = \lim_{T\to\infty} \frac{1}{T} \left| \int_{-T/2}^{T/2} h_N(t) e^{i2\pi f t} dt \right|^2 . \tag{2.6}$$

In the gravitational wave community, the single–sided (defined only for positive frequencies) *linear spectral density* or *linear spectrum* is used rather than (2.6):

$$\tilde{h}_N(f) \stackrel{\text{def}}{=} \sqrt{2S_N(f)}. \tag{2.7}$$

Once known the linear spectral density of noise, it is possible to evaluate the Signal–to–Noise ratio (SNR) in order to obtain the minimum amplitude that a gravitational wave must have for being detected. The SNR depends not only on the absolute level of noise, but on many parameters such as the observation time, the degree of theoretical knowledge of the gravitational wave emission and the data analysis strategy. Hence, knowing the amplitude of the wave and the noise of the receiver is not enough to decide whether the signal is detectable or not. For instance, for a burst signal of duration τ we can roughly write down the signal to noise ratio as:

$$SNR \simeq \frac{h\sqrt{\tau}}{\left(\overline{\tilde{h}_N(f)}\right)_{\Delta f = \frac{1}{\tau}}}, \tag{2.8}$$

where the linear spectral density of the noise is averaged over the bandwidth $\Delta f = \frac{1}{\tau}$ of the signal. The larger the signal bandwidth, the more degraded the SNR. On the other hand, the signal to noise ratio for a periodic gravitational wave of frequency f_{GW} depends on the observation time T:

$$SNR \simeq \frac{h\sqrt{T}}{\tilde{h}_N(f_{GW})}. \tag{2.9}$$

The antenna sensitivity for periodic signals is proportional to the inverse square root of the observation time, therefore, in spite of their small amplitude, periodic gravitational waves are likely to be detected operating for a suitable integration time.

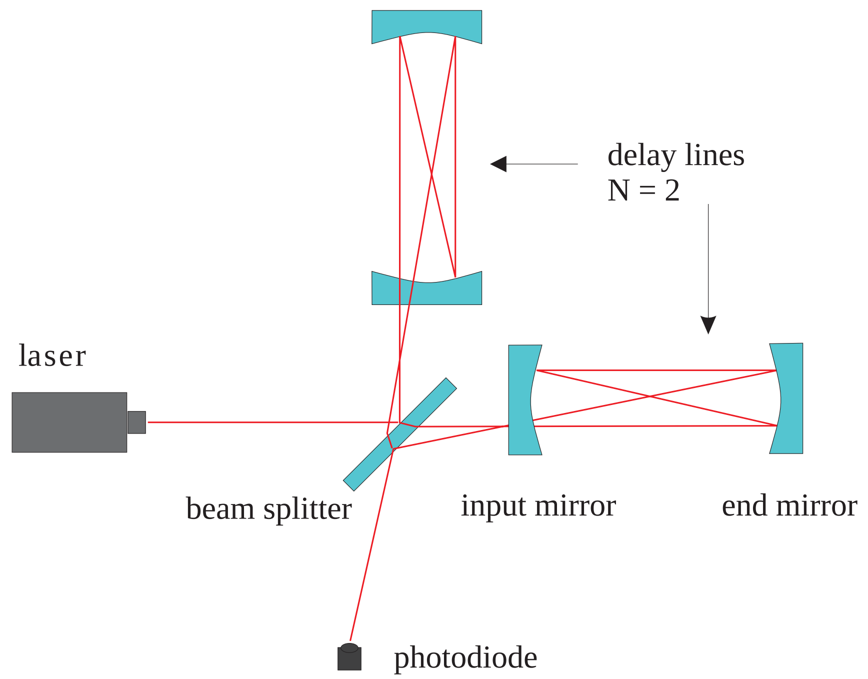

Figure 2.2: *Michelson interferometer with delay lines. Beams are made bounce back and forth in the arms several times before they recombine onto the beam splitter. The phase shift induced by the gravitational wave is so amplified.*

2.3 Delay lines and Fabry–Perot cavities

As we pointed out in section 1.4, the interferometer arm lengths play a fundamental role in increasing the phase response of the antenna (see eq. (1.23)). The need to increase the phase shift due to a gravitational signal is dictated by the existence of noise which affects only the phase of the laser beam without creating a real displacements of the mirror. The detection condition ($S/N \geq 1$) for the expected gravitational signals would require, for a simple Michelson interferometer, an unrealistic arm length (also for budget reasons). A way to improve the phase response is to increase only the optical path length of the beams by bouncing the light back and forth several times along the arms before it returns to the beam splitter. In such a way the phase difference induced in a single round trip is multiplied by the number of cycles the light does in each arm. Current and planned interferometric antennæ are using one of the two schemes described below: *delay lines* and *Fabry–Perot* interferometers.

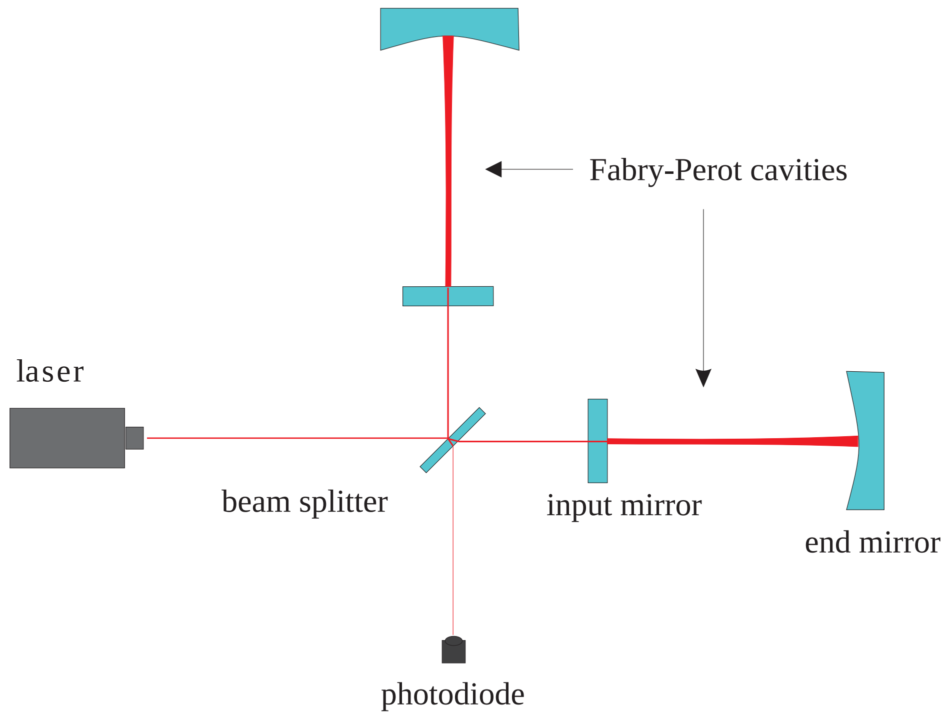

Figure 2.3: *Fabry–Perot cavities are replacing the arms of the interferometer. The phase shift induced by the gravitational wave is amplified by storing the light into the cavities for a time depending on their finesse $\mathcal{F}$.*

2.3.1 Delay lines

In fig. 2.2 the optical layout of a Michelson interferometer with delay lines[14] is sketched. The laser beams are made to bounce back and forth in the arms a large number of times N before they recombine onto the beam splitter. When a gravitational wave of frequency f_{GW} impinges the interferometer, according to eq. (1.22), the bouncing light beam will build up, during its N round trips, a total phase delay

$$\delta\phi_{D.L.} = \frac{4\pi N L h}{\lambda} \frac{\sin\left(\pi f_{GW} \tau_s\right)}{\left(\pi f_{GW} \tau_s\right)}, \tag{2.10}$$

where the *storage time* $\tau_s = 2NL/c$ is the amount of time the light spends into each delay line. For low frequency wave ($f_{GW} \cdot \tau_s \ll 1$) the phase response is N times better than the the response obtained with a single bounce of the light.

2.3.2 Fabry–Perot

In the Fabry–Perot system, as shown in fig. 2.3, each arm is operated as a resonant Fabry–Perot cavity[15]: light from the laser is split at the beam splitter and enters the two cavities through the back of the partially transmitting input mirrors. The two end mirrors have reflectivity close to unit (within a p.p.m.) and the entering light gets resonantly trapped into the cavities.

Slight changes in the length of each cavity drive the cavity slightly off resonance and thereby produce sharp changes in the phase of the exiting light. Consequently, when the light beams *reflected* by each cavity recombine at the beam splitter their relative phase is highly depending on the modulation δL of the length L of the two cavities.

The phase response to an impinging gravitational wave of a Fabry–Perot type interferometric receiver is given by:

$$\delta\phi_{F.P.} \simeq \tau_s \frac{8\pi c}{\lambda} \frac{h}{\sqrt{1 + (4\pi f_{GW} \tau_s)^2}}. \tag{2.11}$$

Here the storage time τ_s is defined through the Fabry–Perot *finesse* $\mathcal{F}$, a parameter measuring the *sharpness* of the resonant cavity:

$$\tau_s = \frac{2L}{c} \frac{\mathcal{F}}{2\pi}. \tag{2.12}$$

When compared to a simple Michelson of the same length, a Fabry–Perot interferometer with cavities of finesse $\mathcal{F}$ shows a phase response $\mathcal{F}/2\pi$ times better, as well as the actual length of the interferometer was increased by the same factor.

As for the case of a Michelson interferometer, with or without delay lines, the phase response of the Fabry–Perot interferometer is quite flat until the frequency of the observed gravitational wave becomes comparable to the inverse time the light spends traveling into each arm: here the response starts decreasing because the photons integrate the space–time perturbation over a whole (ore more than one) period of the gravitational wave (see fig. 1.3).

At this point one might reasonably think that it is possible to indefinitely enhance the phase response of an interferometric receiver, even of small dimension, by folding the optical path into suitable delay lines or Fabry–Perot cavities. But unfortunately, as we will show in the next sections, this would also increase the uncertainty on the

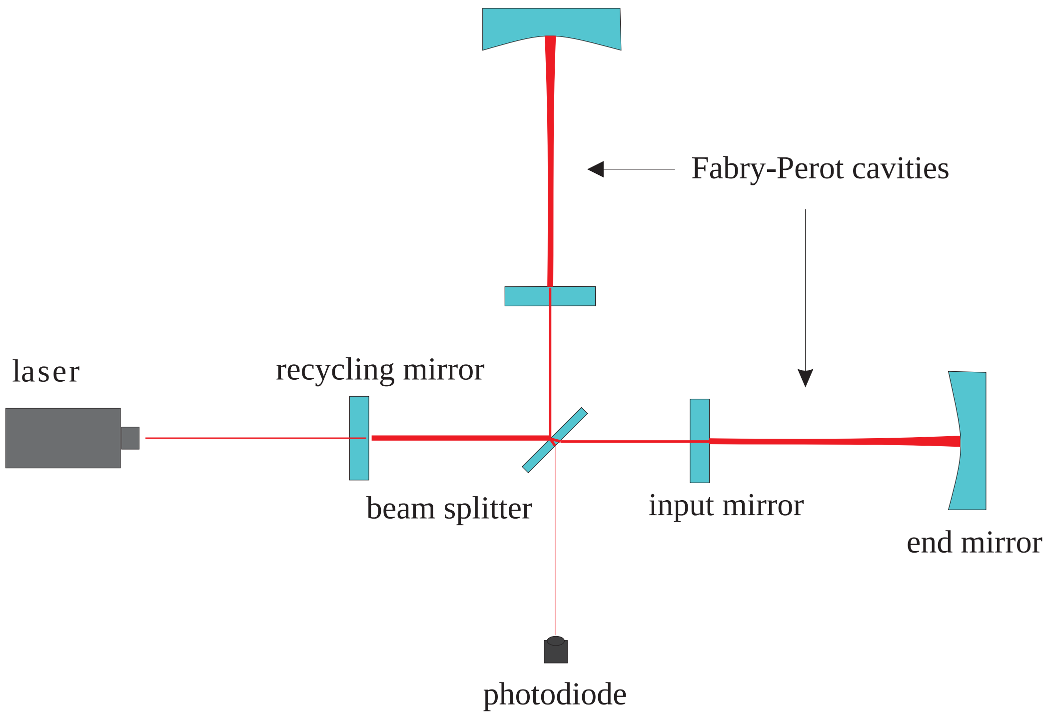

Figure 2.4: *Optical scheme of a Fabry–Perot interferometer with power recycling. The recycling mirror between the laser and the beam splitter reflects the light back to the interferometer which is locked on the dark fringe.*

mirror position. Let us make a step behind to section 1.4 where we found out that the phase shift due to the impinging gravitational wave could be also explained as a strain of the arms of the interferometer: the "displacement response" only depends on the actual arm length hence this one has to be chosen in such a way to overcome the effects due to the noise affecting the mirror position.

2.4 Photon counting noise and quantum limit

An interferometric detector like VIRGO aims to measure length variations below 10^{-18} m, that is about 1/1000 of a proton diameter. This number would be meaningless while thinking about the position of a single atom, whereas it makes sense if we deal with a crystal made of a huge number of atoms whose averaged position is measured by the laser beam wavefront. Nevertheless, a quantum limit to the achievable precision exists, how predicted by the Heisemberg uncertainty relation.

Actually, the ultimate noise which affects the phase shift at the output of the detector is the photon counting noise $\Delta\phi_{pc}$ due to the anticorrelated fluctuations Δn of the number of photons n in the interferometer arms, according to the uncertainty relation $\langle\Delta\phi^2\rangle \cdot \langle\Delta n^2\rangle \geq 1$. For a photon coherent state $\Delta n = \sqrt{n}$ and we can write the phase fluctuations due to photons counting error as:

$$\langle\Delta\phi_{pc}^2\rangle \simeq \frac{1}{n} = \frac{h\nu}{WT}, \tag{2.13}$$

where h is the Planck's constant, ν is the laser frequency, W is the power of the beam entering the interferometer and T is the measurement time. The linear spectral density of this phase fluctuation is straightforward:

$$\Delta\tilde{\phi}_{pc} = \sqrt{\frac{2h\nu}{W}} \tag{2.14}$$

and we can find the linear spectral density of the equivalent strain noise affecting a Fabry–Perot interferometer by inverting equation (2.11):

$$\tilde{h}^{FP}_{shot}(f) = \frac{\lambda}{8\pi L}\frac{2\pi}{\mathcal{F}}\sqrt{\frac{h\nu}{2W}}\sqrt{1+(4\pi f\tau_s)^2}. \tag{2.15}$$

The level of this noise, usually called *shot noise*, can be reduced by increasing the power of light circulating into the interferometer[16, 17]. If the interferometer is locked on the dark fringe, most of the power reflected back to the laser can be recycled by inserting an additional mirror between the laser and the beam splitter which reflects back the light towards the interferometer (see fig. 2.4). The interferometer can be described as a composite mirror which, together with the recycling mirror, forms a *recycling cavity* to be kept in resonance. With this *power recycling technique* the power stored into the arms can be increased by a large factor, thus reducing the shot noise level.

Beside the above mentioned phase noise, the quantum fluctuations of the number of photons are also responsible of fluctuations in the radiation pressure on the mirrors of the interferometer. The displacement noise produced Δx_{pr} is proportional to the square root of the number of photons hitting the mirrors hence, to the power circulating into the interferometer. The accuracy in measuring the mirror position is so limited by the incoherent sum of this pressure radiation noise and the displacement noise producing the phase shift $\Delta\phi_{pc}$. In terms of linear spectral density, the total displacement of a mirror of mass M is:

$$\tilde{\Delta x}_n(f) = \sqrt{\left(\frac{\lambda}{4\pi}\right)^2 \left(\frac{1}{2\mathcal{N}}\right)^2 \frac{2h\nu}{W} + \left(\frac{1}{2Mc}\right)^2 \left(\frac{2\mathcal{N}}{(2\pi f)^2}\right)^2 2h\nu W}, \tag{2.16}$$

where $\mathcal{N}$ indicates how many times the optical path is "folded", i.e. N for the delay lines and $\mathcal{F}/2\pi$ for the Fabry–Perot cavities. Folding makes decrease the first contribution while enhancing the second in the right hand term of equation (2.16). At a given frequency f there is an optimum laser power that minimize the total quantum noise:

$$W_{opt} = \left(\frac{1}{2\mathcal{N}}\right)^2 \frac{Mc^2}{\omega}(2\pi f)^2 \tag{2.17}$$

and the corresponding minimum displacement is close to the standard quantum limit for the accuracy with which the position of a mass M can be measured:

$$\Delta x_{ql}(f) = \sqrt{\frac{\hbar}{M}} \frac{1}{2\pi f}. \tag{2.18}$$

Actually, the interferometric receiver is very similar to the Heisemberg microscope: here the mirrors are playing the role of the particle whose position has to be measured and the laser beam is the analogous of the photon which is used to do the measurement.

The quantum limit for the sensitivity of the interferometric detection of gravitational waves is easily obtained combining equations (1.20) and (2.18). For a given frequency f we have:

$$h_{ql}(f) = \frac{1}{\pi f L}\sqrt{\frac{\hbar}{M}}. \tag{2.19}$$

The function $h_{ql}(f)$ is not the linear spectral density of a noise but it represents the minimum detectable amplitude for a gravitational wave of a given frequency f. Anyhow, it can be used as well as it was a linear spectral density to trace a borderline in the spectral sensitivity plot that characterizes the receiver performances.

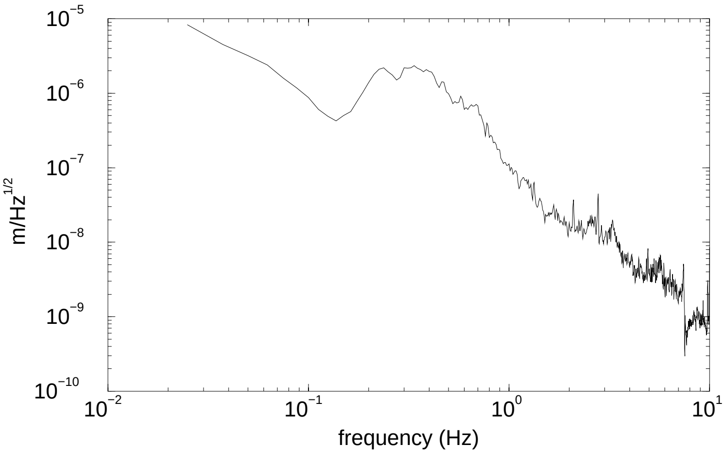

Figure 2.5: *Linear spectrum of the horizontal seismic displacement measured at Pisa INFN laboratories on a Sunday (low human activity, $\xi \sim 0.1$ while in weekdays $\xi \sim 0.3 \div 0.5$). The curve shows a rough $1/f^2$ slope above 1 Hz. The broad peak at 0.14 Hz is found all over the world and is due to the oceans activity.*

2.5 Mirror position disturbances

2.5.1 Seismic noise

A ground based interferometric antenna suffers of the permanent soil vibrations induced by seismic activity, wind, oceans activity and human activity. They are transmitted to the optical components throughout the suspension systems and the resulting noise is the main limitation to the sensitivity of the receiver in the low frequency range. The way to get rid of this noise making the ground based gravitational wave detection possible is the subject of this thesis and will be largely discussed in the following chapters.

There is no universal law describing seismic disturbance. Its intensity can change of orders of magnitude depending on the place where it is measured, but also, in the same place, it can change from a day to another. A general $1/f^2$ behaviour at frequencies above 1 Hz has been found everywhere due to the transmission properties of soil and rocks. The displacement of a generic point of soil is roughly isotropic and, in our laboratory, can be approximately described by an empirical formulation of its linear spectral density:

$$\tilde{x}_{soil}(f) = \xi \frac{10^{-6}}{f^2} \left[\frac{f^2 + f_0^2}{f^2 + f_1^2} \right] \quad \frac{\mathrm{m}}{\sqrt{\mathrm{Hz}}}, \tag{2.20}$$

where $\xi \sim 0.1 \div 1 \text{ m} \cdot \mathrm{Hz}^{\frac{3}{2}}$, $f_0 \sim 0.1$ Hz and $f_1 \sim 0.5$ Hz. The linear spectral density of seismic displacement measured in a horizontal direction on a day with low human activity is shown in fig. 2.5.

In section 2.1 we have seen how suspending the optics of the interferometer makes them freely falling masses above the resonant frequency of the suspension. If we want to take into account the transmission of soil vibrations we have to modify the equation (2.1) adding the position of the suspension point x_0, directly connected to the noisy ground, to the elastic term

$$m\ddot{x} + \frac{mg}{l}(x - x_0) = F_{ext} \tag{2.21}$$

which gives in the frequency domain

$$\hat{x}(\omega) = \frac{\omega_0^2 \hat{x}_0(\omega)}{\omega_0^2 - \omega^2} + \frac{\hat{F}_{ext}(\omega)/m}{\omega_0^2 - \omega^2}. \tag{2.22}$$

The transmission of soil vibrations from the suspension point to the payload is described by the *transfer function* $TF(\omega)$ of the suspension. This is defined as the ratio between the Fourier transform of the payload displacement and that of the displacement of the suspension point when no external force is applied. For the simple pendulum, as well as for a simple oscillator, we have:

$$TF(\omega) = \frac{\hat{x}(\omega)}{\hat{x}_0(\omega)} = \frac{\omega_0^2}{\omega_0^2 - \omega^2}. \tag{2.23}$$

For frequencies below the pendulum resonant frequency ($f \ll f_0$), it is $TF(\omega) \simeq 1$, the suspension is *rigid* and the vibrations are entirely transmitted. Above the resonant frequency ($f \gg f_0$) the suspension is a *soft* connection with the soil and vibrations are attenuated:

$$TF(\omega) \simeq \frac{\omega_0^2}{\omega^2} \ll 1. \tag{2.24}$$

The transfer function in equation (2.23) diverges for $f = f_0$ since we are neglecting the dissipative term. In any realistic oscillator the amount of dissipation determines the quality factor Q and, at the resonant frequency, the excitation is amplified by this factor:

$$|TF(\omega_0)| = Q. \tag{2.25}$$

If N simple oscillators are cascaded, N eigenmodes of eigenfrequencies f_i are present. The transfer function, neglecting again the dissipation, is:

$$TF(\omega) = \prod_{i=1}^{N} \frac{\omega_i^2}{\omega_i^2 - \omega^2}. \tag{2.26}$$

Well above the higher resonant frequency, the transmission of vibrations decreases N times more rapidly than in the simple oscillator:

$$TF(\omega) \simeq \frac{\prod_i \omega_i^2}{\omega^{2N}}. \tag{2.27}$$

Once known the transfer function $TF(f)$ of the suspension system and assuming they are the same for all the optical components, we can write down the linear spectral density of the equivalent strain noise for the interferometric detector:

$$\tilde{h}_{seism}(f) = \frac{2}{L} \left| TF_{susp}(f) \right| \xi \frac{10^{-6}}{f^2} \left[\frac{f^2 + f_0^2}{f^2 + f_1^2} \right], \tag{2.28}$$

where, for consistency with equation (2.20) the arms length L has to be expressed in meters.

2.5.2 Gravity gradient noise

Seismic noise is not a fundamental physical limit: in principle it is possible to reduce the transmission of soil vibrations to the optical components by suspending them to cascade of longer and longer pendula, in order to push toward zero all the resonant frequencies. Unfortunately, there is another way the soil vibrations affect the interferometer optics limiting the efficiency of the seismic isolation: through the local gravitational field. Due to the seismic waves, the mass density distribution around the mirrors fluctuates and the local gravitational field fluctuates as well. These fluctuations directly couple with the mirrors bypassing the vibration isolation system. An estimation of the equivalent strain noise is given by[18]:

$$\tilde{h}_{ggn} = \frac{2}{3\sqrt{\pi}} \frac{G\rho}{L} \frac{x_{soil}(f)}{f^2}, \tag{2.29}$$

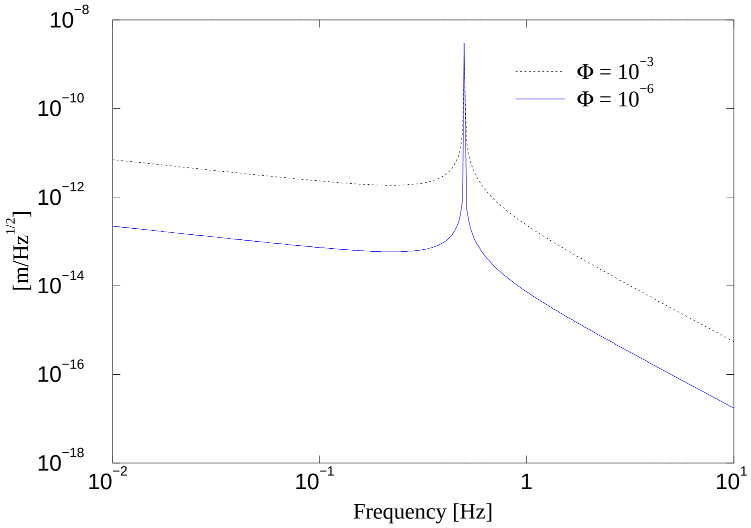

Figure 2.6: *Calculated linear spectral density of the thermal noise for a pendulum ($l = 1$ m, $m = 1$ kg) for two values of the dissipation factor ϕ.*

where G is the gravitational constant, ρ is the average local soil density and $x_{soil}(f)$ is the local seismic spectrum.

The gravity gradient noise, also called *newtonian* noise, sets the limit at low frequency of the sensitivity achievable by a ground based interferometric antenna. There is a frequency (a few Hz) at which this noise dominates over the other non–seismic noises. Below this frequency the seismic attenuation becomes useless and the sensitivity of the interferometer cannot be improved any more. In the next chapter we will clarify this statement when we describe in detail the VIRGO sensitivity curve.

2.5.3 Thermal noise

Thermal noise is associated with internal dissipation phenomena. According to the fluctuation–dissipation theorem[19], dissipation phenomena are connected to a stochastic motion of the system itself. For a linear mechanical system, we can write its equation of motion in the frequency domain in terms of an external force $F_{ext}(\omega)$ necessary to cause the system to move with a sinusoidal velocity of amplitude $v(\omega)$:

$$F_{ext} = Zv, \tag{2.30}$$

where the function $Z(\omega)$ is called the *impedance*. The fluctuation–dissipation theorem states that, at thermodynamic equilibrium, the power spectrum $F^2_{therm}(\omega)$ of the minimal fluctuating force on a system is given by:

$$F^2_{therm}(\omega) = 4k_B T \Re(Z(\omega)), \tag{2.31}$$

where $\Re(Z)$ indicates the real (i.e. dissipative) part of the impedance, k_B is the Boltzmann's constant, and T is the absolute temperature.

If we consider again our simple oscillator, in the hypothesis of dissipation due to the material structure, the system losses can be modeled in the frequency domain by adding an imaginary component to the elastic constant k[20]:

$$-m\omega^2 \hat{x}(\omega) + k\left[1 + i\phi(\omega)\right]\hat{x}(\omega) = \hat{F}_{ext}. \tag{2.32}$$

The function $\phi(\omega)$ represents the phase lag between the mass displacement at a given frequency and the sinusoidal driving force. Experimentally, $\phi(\omega)$ is found to be roughly constant and, for low loss materials, it is $\phi \ll 1$[21].

Using the fluctuation–dissipation theory and a little algebra, the spectrum of the mass displacement is written:

$$S_{X_{th}}(\omega) = \frac{4k_B T\phi\omega_0^2}{m\omega\left[(\omega_0^2 - \omega^2)^2 + \omega_0^4\phi^2\right]}, \tag{2.33}$$

where we remember that $\omega_0/2\pi = \sqrt{k/m}$ is the oscillator resonant frequency. It can be shown that, for a low loss material, the quality factor is $Q = 1/\phi(\omega_0)$.

The dependence on the frequency of the linear spectrum can be summarized as follows:

$$\begin{aligned} \tilde{x}_{th}(\omega) &\simeq \frac{C\sqrt{\phi}}{\omega_0}\cdot\frac{1}{\omega^{1/2}} && \text{for } \omega \ll \omega_0; \\ \tilde{x}_{th}(\omega) &= \frac{C}{\sqrt{\phi\omega_0^3}} && \text{for } \omega = \omega_0; \\ \tilde{x}_{th}(\omega) &\simeq C\sqrt{\phi}\omega_0\cdot\frac{1}{\omega^{5/2}} && \text{for } \omega \gg \omega_0; \end{aligned} \tag{2.34}$$

where we have put $C = \sqrt{4k_B T/m}$.

As we can see, the off resonance parts of the linear spectrum are both proportional to the square root of ϕ: far from resonance, the thermal noise is reduced while using high Q materials (see fig. 2.6) and, even if at resonance the peak is higher, it is also sharper. This agrees with the *equipartition theorem* from which it arises that the mean square fluctuation $< x^2 >$, in other words the integral of the displacement power spectrum, is proportional to $k_B T$, independently on Q. Increasing the Q factor means to confine the amount of thermal noise in a narrower and narrower band around the resonant frequency of the oscillator.

For complex mechanical systems such as the mirror suspension or the lattice of the mirror itself, the thermal noise has to be calculated taking into account all the vibrational modes. Each mode is characterized by its resonant frequency $\omega_n/2\pi$, its quality factor Q_n and its effective mass μ_n, defined as:

$$\mu_n = \frac{E_n}{\omega_n^2 x_n^2}, \tag{2.35}$$

where E_n is the mode energy and x_n is the oscillation amplitude. The analogous of equation (2.32) for a complex system is written:

$$S_{X_{th}}(\omega) = \frac{4k_B T}{\omega} \sum_n \frac{\phi_n \omega_n^2}{\mu_n \left[(\omega_n^2 - \omega^2)^2 + \omega_n^4 \phi_n^2\right]}. \tag{2.36}$$

Far from resonances, the frequency dependence is the same as in equation (2.34).

Thermal noise affecting the interferometer sensitivity arises from the internal dissipation which is present both in the wires supporting the mirrors and in the mirrors themselves. Beside the pendulum mode, the suspension wires also show higher frequencies normal modes, called *violin modes*, which are excited by thermal fluctuations as well. As it will be shown in next chapter, the pendulum mode contribution is the main limit to the antenna sensitivity from a few Hz to a few tens of Hz. For higher frequencies, up to hundreds of Hz, the thermal noise due to the mirror dominates over the other noises. Each mirror is indeed a quartz cylinder with several mechanical drum modes whose thermal excitation disturbs the position or the shape of the reflecting surface.

Thermal noise is highly depending on the mechanical properties of the materials. High Q materials have to be used for reducing the thermal noise limit to the interferometer sensitivity. At the same time, it is important to keep all the resonant frequencies of the suspensions and of the mirrors outside the aimed detection band.

2.5.4 Creep

The stressed mechanical parts of the suspensions may be sources of mirror position disturbances due to *creep* phenomena. A creep event is a sudden release of the stress accumulated in the lattice which can produce a mirror displacement orders of magnitude higher than the ones expected from impinging gravitational waves. Moreover, integrated creep effect causes a weakening in the most stressed parts of the mirror suspension, turning into a remarkable lowering of the vertical position of the mirror.

The in depth investigation performed by the author about the creep noise, as well as the identification of the best creep free materials to reduce it, is the subject of chapter 6 of this thesis.

2.6 Laser Instabilities

2.6.1 Frequency fluctuations

In principle, the arms of an interferometer for gravitational wave detection can be of different lengths. In practice, the two arms have to be nearly equal because of laser frequency fluctuations. The phase response of an interferometer depends on the laser wavelength and therefore, on its frequency $\nu = c/\lambda$. If $\tilde{\Delta\nu}(f)$ is the linear spectral density of the laser frequency fluctuations and if the arms are unequal, there will be a phase shift $\tilde{\delta\phi}$ at the output of the interferometer even if the mirror position remains unchanged:

$$\delta\phi = \frac{2\pi\tilde{\Delta\nu}}{c}\Delta L_{opt}, \tag{2.37}$$

where ΔL_{opt} is the static difference in the optical path length between the two arms. The equivalent strain noise noise is then:

$$\tilde{h}_{ff}(f) = \frac{\tilde{\Delta\nu}(f)}{\nu}\frac{\Delta L_{opt}}{L_{opt}}. \tag{2.38}$$

For an asymmetry factor $\beta = \Delta L_{opt}/L_{opt}$ of about 1% (this is what expected in VIRGO), a frequency stability of about 10^{-5} Hz/$\sqrt{\text{Hz}}$ is required at 100 Hz. An available uncontrolled laser generally presents a stability of 10^2 Hz/$\sqrt{\text{Hz}}$, this means that the laser frequency fluctuations have to be reduced by a factor 10^7.

2.6.2 Power fluctuations

Beside the frequency fluctuations, lasers are also affected by emitted power fluctuations. Actually, the photodiode at the output of the interferometer measures the power P_{out} of the "ordinary" beam returned by the beam splitter, according to

$$P_{out} = \frac{P_{in}}{2}\left[1 + \cos\left(\phi_0 + \delta\phi\right)\right], \tag{2.39}$$

where P_{in} is the laser input power, ϕ_0 is the chosen operating point and $\delta\phi$ is the phase shift induced by the signal we want to detect.

The power response of the interferometer to the mirror displacement is maximum at $\phi_0 = \pi/2$ so, with this choice and taking into account the power fluctuations ΔP, the output power results:

$$P_{out} = \frac{P_{in} + \Delta P}{2}\left(1 - \sin\delta\phi\right) \approx \frac{P_{in}}{2}\left(1 + \frac{\Delta P}{P_{in}} - \delta\phi\right). \tag{2.40}$$

In order not to mask the effect of a true signal, the power stability should exhibit a level extremely difficult to reach: the detection condition would be, e.g. for VIRGO, $\Delta P/P_{in} \ll \delta\phi \approx 10^{-11}$.

To overcome the power fluctuation noise it is better to operate the interferometer on the *dark fringe*, that is at $\phi_0 = \pi$. In this case it is:

$$P_{out} = \frac{P_{in} + \Delta P}{4} \cdot (\delta\phi)^2 \tag{2.41}$$

and detecting a signal only requires $\Delta P \ll P_{in}$. The drawback of this choice is that the power response of the receiver is much worse and, above all, it is not sensitive to the sign of $\delta\phi$. To obtain an adequate response maintaining the dark fringe operation the below described Pound–Drever signal extraction is used.

2.6.3 Heterodyne detection

A common *lock–in* technique to get rid of the $1/f$ noise in interferometric detector is to modulate in phase the laser in order to produce sidebands. Phase modulation can be done by introducing Pockel cells in the two arms of Michelson interferometer. If the two cells are driven in anti–phase with a sinusoidal voltage at frequency $\Omega/2\pi$, the output phase is:

$$P_{out} = \frac{P_{in}}{2}\left[1 + \cos\phi_0 + \delta\phi + 2m\sin\Omega t\right]. \tag{2.42}$$

The parameter m is the *modulation index* and measures the energy of the sidebands. Equation (2.42) can be simplified if the interferometer is operated around the dark fringe ($\phi_0 \simeq \pi$) and the modulation index is small ($m \ll 1$). Neglecting the higher order harmonics, we have:

$$P_{out} \simeq \frac{P_{in}}{2} \left[1 - J_0(2m) + 2\delta\phi J_1(2m) \sin \Omega t\right], \qquad (2.43)$$

where J_0 and J_1 are the Bessel function of order 0 and 1, respectively. The latter equation shows that modulating the light turns into a first order dependence of the output power on the phase shift even if the interferometer is kept on the dark fringe.

Heterodyne detection allows to perform measurements at frequencies where the laser instabilities are smaller and the $1/f$ noise of the electronics is less important.

2.7 Other sources of noise

Here is a list of some other sources of noise which have been considered in designing an interferometer like VIRGO.

2.7.1 Refraction index fluctuations

Fluctuations of the gas pressure generate fluctuations of the refractive index and, consequently, a phase noise. The intensity of the noise is proportional to the gas polarizability and the main residual gas is expected to be hydrogen. In order to keep this phase noise below the shot noise level, the interferometer has to be contained in an ultra high vacuum pipe. The required total pressure is less than 10^{-9} mbar.

2.7.2 Acoustic noise

The vacuum level required to eliminate the above mentioned noise due to refractive index fluctuation is sufficient to isolate the optical components from acoustic noise and from thermal noise associated to viscous damping. The newtonian noise associated to the acoustic waves is not reduced but it is expected to not affect the interferometer sensitivity.

2.7.3 Scattered light

Photons scattered by mirror imperfections and bouncing on the pipe walls get a different phase due to modulating effect of pipe seismic vibrations. If such photons recombine with the laser beam a phase noise will arise. To get rid of this problem, a set of absorbing *baffles* is placed along the pipe[22].

2.7.4 Light in higher modes

The electric field of the laser beam may be decomposed into a sum of different modes and each of them acquires a different phase shift while propagating in the cavities. Only one mode has to be selected for a correct operation. For this purpose an optical cavity, called *mode cleaner*, capable of selecting the TEM_{00} mode only, is usually placed between the laser and the interferometer.

Chapter 3

The VIRGO project

At present five ground based interferometric detectors are near to be operating in the world: two in USA (LIGO)[23], one in Italy (VIRGO)[24, 25], one in Germany (GEO600)[26] and one in Japan (TAMA)[27]. Among them VIRGO is the only one which aims to reach high sensitivity at low frequency too. A sixth interferometer is expected to be built in the forthcoming years in Australia (ACIGA)[28].

The goal of VIRGO is to obtain a sensitivity of $\tilde{h} \approx 10^{-23}\ 1/\sqrt{\mathrm{Hz}}$ above 100 Hz (limited by shot noise) and, above a few Hz, to reduce the seismic noise well below the thermal noise floor limiting the antenna sensitivity in the low frequency range ($\tilde{h} \approx 10^{-21}\ 1/\sqrt{\mathrm{Hz}}$ @ 10 Hz)[30]. The apparatus, a Michelson interferometer with two Fabry–Perot cavities 3 km long, has been built at the site of Cascina, near Pisa.

In this chapter we want to outline the design of the VIRGO antenna and to compare its target sensitivity with the expected amplitude of the gravitational signals coming from the astrophysical sources discussed in chapter 1.

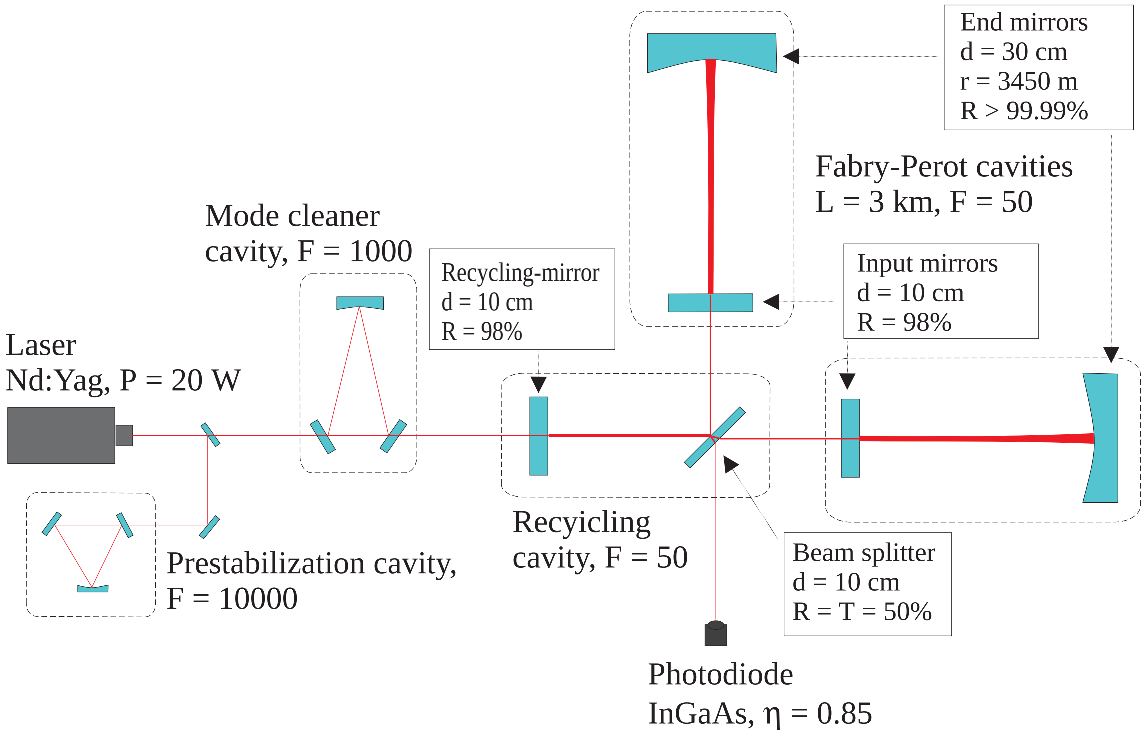

Figure 3.1: *Scheme of the VIRGO interferometer with the 3 km long Fabry–Perot cavities and the recycling cavity.*

3.1 The VIRGO apparatus

The main items of the VIRGO apparatus for gravitational wave detection are: optics, suspensions and vacuum. Each of them has to exhibit very special (often unique of ones' kind) features in order to reach the required specifications.

3.1.1 Optics

The optical layout of the VIRGO interferometer is shown in fig. 3.1.

Laser source : it is a Nd:Yag emitting at $\lambda = 1064$ nm. The laser wavelength is not critical: the reason of this choice is that lasers emitting in the infrared region are more powerful. The output power in the TME_{00} mode is about 20 W. The stability requirements are:

1. power

$$\frac{\tilde{\Delta P}}{P} < \begin{cases} 3 \cdot 10^{-5}/\sqrt{\mathrm{Hz}} & @\ f = 10\ \mathrm{Hz} \\ 3 \cdot 10^{-7}/\sqrt{\mathrm{Hz}} & @\ 100 < f < 1000\ \mathrm{Hz}; \end{cases} \tag{3.1}$$

2. frequency

$$\frac{\tilde{\Delta \nu}}{\nu} \approx \begin{cases} 10^{-4}/\sqrt{\mathrm{Hz}} & @\ f = 10\ \mathrm{Hz} \\ 10^{-6}/\sqrt{\mathrm{Hz}} & @\ 100 < f < 1000\ \mathrm{Hz}. \end{cases} \tag{3.2}$$

The laser, including the stabilization optronics and the phase modulator, is not under vacuum but it is placed on an optical table within a clean room.

Input bench : it is an under vacuum and suspended optical bench. It is equipped with a rigid triangular reference cavity (for the pre–stabilization of the laser frequency), the input and output mirrors of the mode cleaner and the main beam expansion and alignment optronics.

Mode cleaner : it is a triangular cavity 144 m long. Input and output mirrors are mounted on the input bench, the far mirror is suspended and is connected to the input bench by means of a dedicated vacuum pipe.

Power recycling : the recycling mirror (10 cm diameter, 98% reflectivity) is suspended and, with the interferometer, forms a resonant cavity. The foreseen recycling factor, defined as the ratio between the power stored in the cavity and the input power, is about 50: a power of about 1 kW is expected on the beam splitter.

Central interferometer : the suspended beam splitter (10 cm diameter), and the two Fabry–Perot cavities form the real interferometer.

Fabry–Perot cavities : each of them is 3 km long with finesse $\mathcal{F} = 50$. The input mirrors are 10 cm diameter, flat and 98% reflectivity. The output mirrors are 100% reflectivity (within a few p.p.m.) and they are larger (30 cm diameter) than the input ones and curved to take into account the laser beam divergence. Both input and output mirrors are suspended.

Detection system : it is composed of a suspended bench under vacuum and an optical table outside the vacuum system. The bench supports the output mode cleaner and the optics to split and collimate the beam on the photodiodes (quantum efficiency $\eta = 0.85$) for the locking and the signal detection, which are placed on the table.

Mirrors : they are monolithic blocks of quartz and have to exhibit enhanced optical performances besides enhanced mechanical quality factors and high internal resonant frequencies for thermal noise reduction. Special techniques of surface treatment are used to reduce losses in reflectivity.

3.1.2 Suspensions

The mirror suspensions carry out a double work: the first is to make the interferometer a freely falling one (see section 2.1), the second concerns the isolation from the soil vibrations that would be transmitted to the mirrors throughout the suspensions themselves. The Pisa VIRGO group has developed a suspension system, called *superattenuator* capable to inhibit the transmission of soil vibrations to the mirror above a few Hz in all the 6 degrees of freedom. Essentially, the superattenuator is a multi–stage pendulum about 9 m tall. The detailed description of this device is deferred to the next chapter and below.

Six full superattenuators (*tall towers*) are suspending the mirrors of the Fabry–Perot cavities, the beam splitter and the recycling mirror. Since the less seismic isolation requirement, three shorter version (*short towers*) are utilized to suspend the input bench, the far mirror of the mode cleaner and the bench of the detection system.

3.1.3 Vacuum system

The volume under vacuum of the VIRGO apparatus (see fig. 3.2) is divided in two parts: the pipe containing the optics and the towers containing the superattenuators. The pipe is 1.2 m diameter and composed of 15 m long modules connected by bellows and resting on special supports allowing the pipe "breath" induced by the baking or by the daily thermal excursion. As mentioned above, the requirement for the noise due to the fluctuations of the refraction index of being at least a factor 10 below the dominant noises, sets the limit for the total pressure to 10^{-9} mbar. A more strict limit

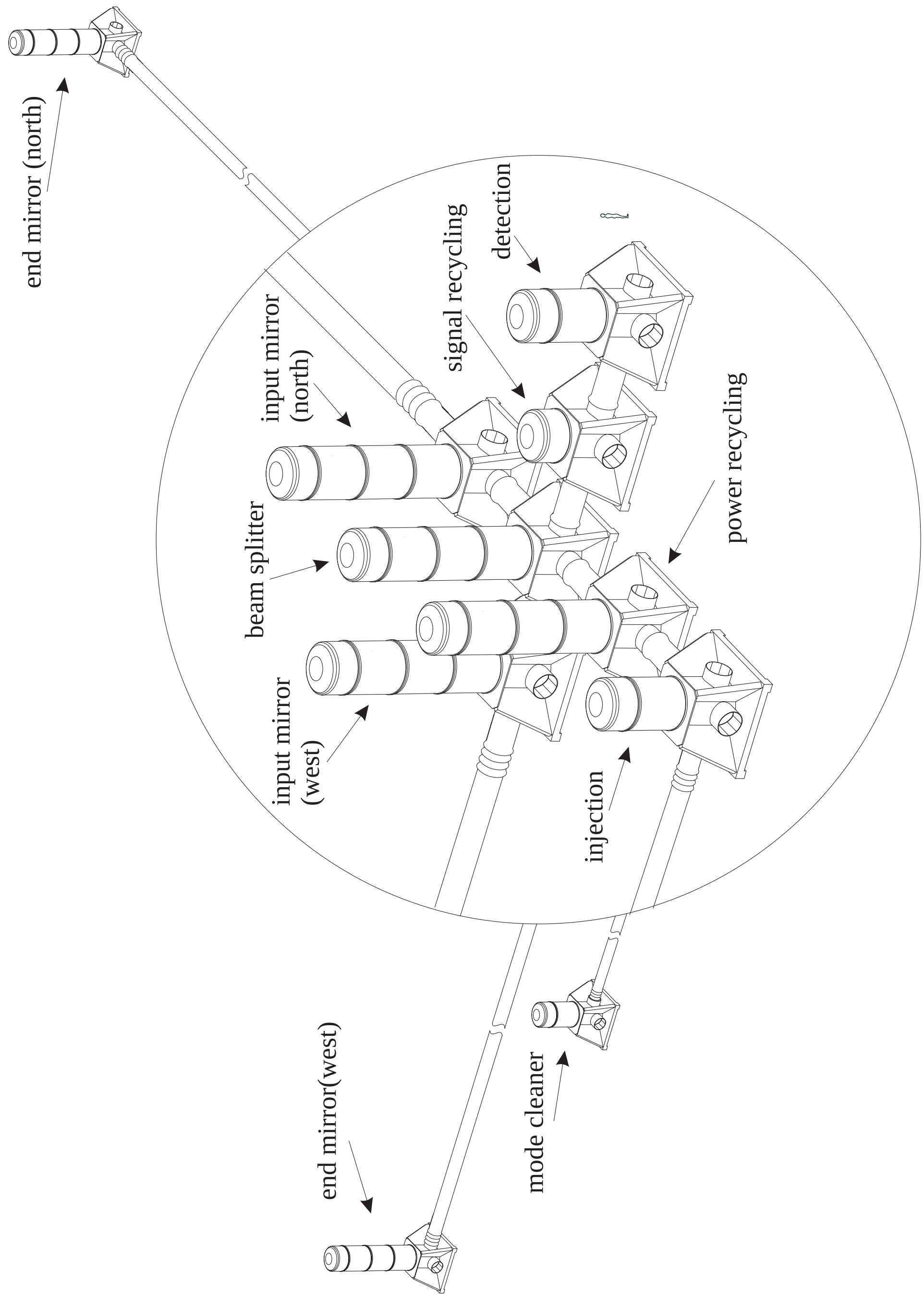

Figure 3.2: *The vacuum setup of the VIRGO interferometer.*

of 10^{-14} mbar is set for the partial pressure of hydrocarbons because these molecules can stick on the surfaces of mirrors and degrade their quality.

The ultra high vacuum required in the pipe cannot be achieved in the towers, because of the large number of devices the superattenuators are provided with. Therefore, the towers are divided in two sections by a separating roof and communicating only through a narrow conductance hole for passing the wire holding the last stage of the suspension. In the upper part a total pressure of 10^{-6} mbar is foreseen.

3.2 Interferometer locking

Locking the interferometer means to actively control the position of the test masses supporting the mirrors in order to keep the interferometer on the dark fringe and both the Fabry–Perot and the recycling cavities in resonance with the laser. These four conditions are fulfilled by extracting the *error signals* from the interferometer, and by driving the actuators for the mirror positioning through feedback *correction signals*[31].

The resonance conditions for the cavities require their lengths to be controlled within $1/10000\lambda \approx 10^{-10}$ m but actually, the root mean square (rms) motion of each mirror should be not larger than 10^{-12} m since the dynamic range limitations of the read–out electronics.

On the other hand, the suspended mirror, because of the suspension resonant modes, exhibits a low frequency swing of the order of tens of μm. This wide motion, entirely confined between 0 and 2 Hz, has to be compensated by means of a suitable control strategy without reinjecting noise into the detection band.

3.3 VIRGO sensitivity

The evaluation of the detector sensitivity is based on the prediction on the intensities of the various noise sources. The total expected noise is converted in the equivalent strain noise $\tilde{h}_N(f)$ defined in section 2.2 and usually called VIRGO sensitivity curve. The predicted sensitivity curve for the VIRGO antenna is shown in fig. 3.3. Depending on the region of frequencies, three different sources of noise are the dominant ones[32].

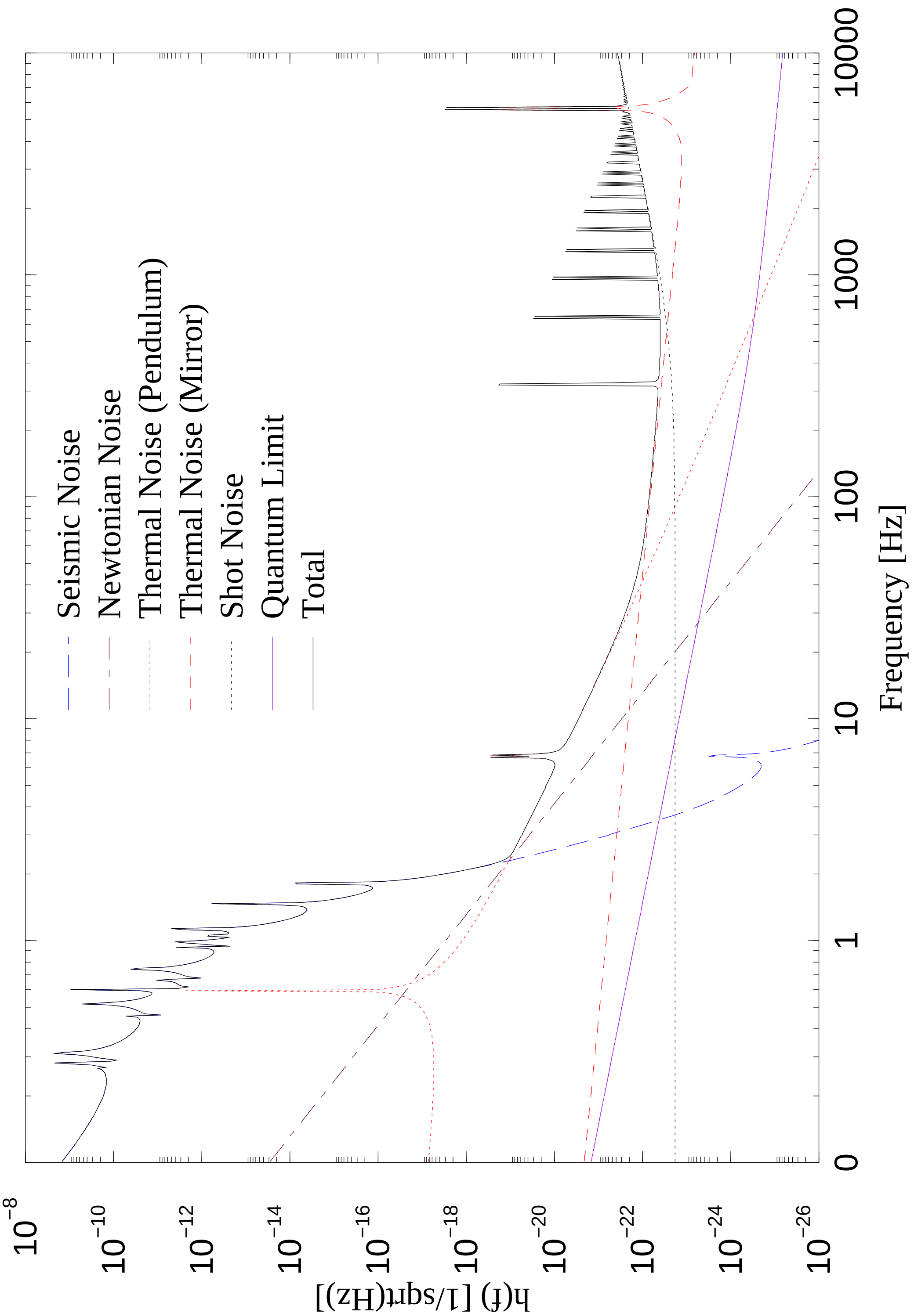

Figure 3.3: *Spectral sensitivity of the VIRGO antenna: the contribution of the main noise sources is shown.*

Seismic noise is expected to be dominant up to about 3 Hz, thanks to the attenuation performance of the superattenuators. This is the low frequency detection threshold of the antenna. A further improvement of the attenuation by lowering the resonant frequencies of the suspension system (see section 2.5) is useless because in that case, as we can see in fig. 3.3, the expected newtonian noise would limit the antenna sensitivity.

Thermal noise dominates from 3 to about 500 Hz; up to about 30 Hz the noise is due to thermal fluctuation of the pendulum formed by the mirror and its suspension wires; above 30 Hz the tail contribution due to the high frequency internal modes of the mirrors is dominant.

Shot noise dominates above 500 Hz. Before the reader worries about the sight of a non–white shot noise, it is worth remembering that we refer to the shot noise (and similarly for the other noises) as the equivalent strain noise $\tilde{h}^{FP}_{shot}(f)$ defined in equation 2.15. The flat phase noise due to the photon counting error is obtained by multiplying our shot noise by the phase response of the Fabry–Perot interferometer.

The sharp peaks, apart from those at about 7 Hz, are due to contribution to thermal noise of the violin modes of the mirror suspension wires; they are in pairs because the two cavity mirrors have different masses. The double peak at 7 Hz is due to thermal noise associated to the main vertical mode of the *marionetta–mirror system*.

With these assumptions about the spectral sensitivity of the antenna, we can review the various astrophysical sources of gravitational waves for evaluating the expected SNR for each of them.

3.3.1 Signals from coalescing binaries

The coalescence of two compact stars is the most promising event to be detected by the first generation of interferometric receivers. The extraction of the signal from the interferometer noisy output will be performed by cross correlating it with the signal expected from the theory (*template*). To achieve the detection it is very important to have accurate theoretical templates and a large effort is being made in this direction.

The expected SNR for a coalescence event has been calculated in the newtonian approximation[33], and it results that about 1 neutron star–neutron star coalescence every 50 years would be observed by VIRGO. Higher SNR is expected as well as the mass of the involved objects increases. More optimistic estimates about the rates of occurrence of coalescence events allow us to be more confident on the detection of the emitted signals.

The SNR for detecting coalescing binaries depends on the minimum frequency at which the detector can start the integration. Starting the integration at 70 Hz would reduce the SNR of about 20% with respect to starting at 4 Hz, hence the importance of extending the detection band toward the low frequency region.

3.3.2 Bursts from stellar collapses

During the last years it has become more evident that the detection of stellar collapses will not be an easy goal for first generation interferometers. Large uncertainties affect the hydrodynamics simulation codes and the evaluated templates. Most of the predicted collapse processes produce gravitational waves detectable only within galactic distance. Even in case of $SNR > 1$ a multiple coincidence detection is required for discriminating between real events and non–gaussian noise. The creation of a network of interferometers and other detectors (such as resonant bars, neutrino detectors, optical telescopes, γ bursts detectors) working in coincidence should allow the unambiguous detection of a burst event as well as, by measuring the delay time between different detection of the same event, the determination of the source direction in the sky.

3.3.3 Periodic signals

Most of the known pulsars are located in the central region of our galaxy and their distance from the Earth ranges from 5 to 20 kpc. As shown in fig. 1.1, most of them emits gravitational waves at frequencies below 10 Hz: this is one of the reasons for the big experimental effort to extend VIRGO sensitivity down to low frequency.

While the spinning frequencies are known with high accuracy, the estimate of the intensity of the emitted gravitational signals is affected by large uncertainties. Only an upper bound can be put on the values of the ellipticity ε (see subsection 1.4.2) to

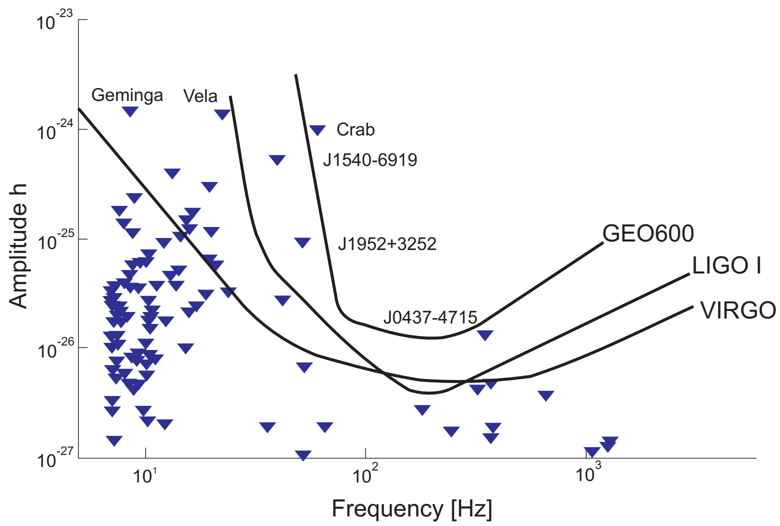

Figure 3.4: *Upper limits of the gravitational wave amplitudes emitted by several galactic pulsars compared to the rms sensitivity of VIRGO, LIGO and GEO600 assuming an observation time of one year.*

compare the amplitude of the signal to the actual detector sensitivity according to equation (2.9). The results are shown in fig. 3.4. The sensitivity of the interferometer can be enhanced in a narrow band around the emission frequency (at the price of reducing the sensitivity outside the band) using a *signal recycling* technique [34, 35].

3.3.4 Stochastic background

The measurements from COBE set a stringent upper limit to the stochastic background intensity at low frequency. Standard inflationary models predict a constant stochastic background spectrum and thus this upper limit could be extended to higher frequencies, in the detection band of the ground based interferometers[38]. This upper limit is orders of magnitude below the sensitivity of present interferometers so, a single antenna would not be enough to detect the stochastic background of relic gravitational waves. The only possibility is to cross correlate the output of two (or more) detectors. They should be far apart in order to not correlate local noise and close enough to maintain correlation for gravitational waves in the VIRGO/LIGO range. A distance of tens of km is suitable to fulfill these conditions[36, 37].

Nevertheless, recent string cosmology models[39] predict a more complex spectrum which should satisfy the COBE limitation at low frequency and, at the same time, they should contain gravitational waves in the VIRGO/LIGO range which might be detectable.

Chapter 4

Extending the detection band to low frequency: the superattenuator

The detection of gravitational waves would be limited, at low frequencies, if the soil vibrations were transmitted throughout the suspensions of the mirrors. They would induce position disturbances ($\sim 10^{-9}$ m/$\sqrt{\text{Hz}}$ @ 10 Hz) larger and larger than the displacements expected from gravitational signals ($\sim 10^{-18}$ m/$\sqrt{\text{Hz}}$ @ 10 Hz). The detection band of the interferometric antenna VIRGO is extended down to few Hertz, thanks to the special system of suspension of the optical components designed to strongly reduce the transmission of soil vibrations: the *superattenuator*. The importance to obtain enhanced sensibility at low frequency too, has been shown in the last section of the previous chapter.

The superattenuator conceived and realized in Pisa is a chain of *mechanical filters*, each of them aiming to suppress the transmission of vibrations to the following stage in all six degrees of freedom. Beside the passive attenuation, this suspension system is suitable for the active control of the position of the optical components. By means of a multi–stage control strategy, the residual motions of the mirrors can be reduced down to the specific requirements ($\delta x_{rms} \sim 10^{-12}$ m) to lock the interferometer without injecting noise into the detection band.

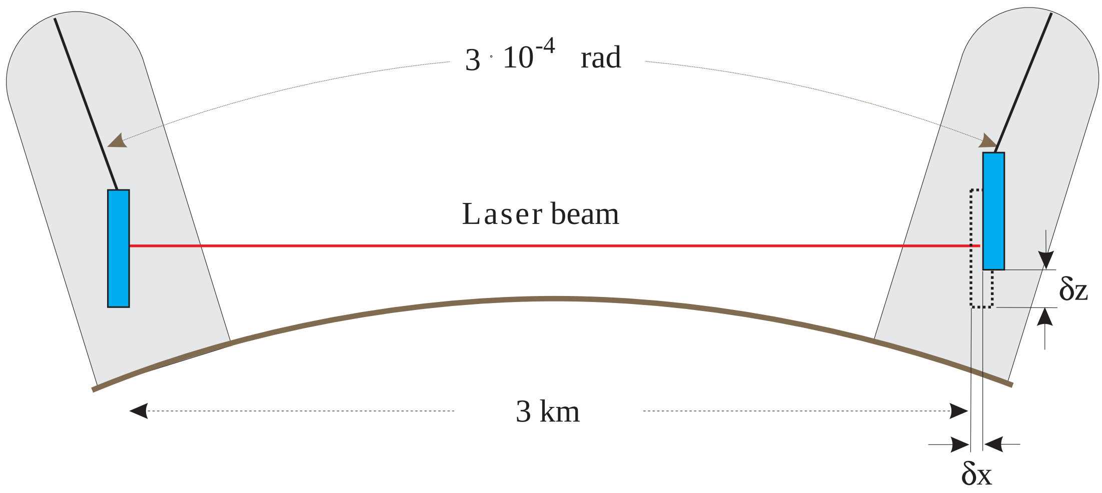

Figure 4.1: *Effect of the Earth curvature on the vertical–horizontal motion coupling: the direction of the gravity over a length of 3 km changes of an angle of $\alpha = 3 \cdot 10^{-4}$ rad. A vertical displacement of the mirror δz turns into a differential displacement $\delta x = \alpha \cdot \delta z$ in the beam direction.*

4.1 The VIRGO superattenuator

4.1.1 Passive attenuation

Although in theory only the components of the vibrations along the laser beam directions affect the interferometer, the suspension system must be effective in all the translation and the angular degrees of freedom. Indeed, in a real mechanical system, there are unavoidable couplings among the different degrees of freedom, at least because of geometrical factors. A minimum coupling factor between the beam direction and the vertical one is due to the Earth curvature, as the suspensions of the input and the end mirrors of a Fabry–Perot 3 km long are not parallel but form an angle of $3 \cdot 10^{-4}$ rad (see fig.4.1). Moreover, motions in directions different from that of the beam can compromise the mirrors alignment.

In order to get an uniform an gradual attenuation in all the degrees of freedom, the superattenuator has been designed as a chain of mechanical filters in cascade:

each of them attenuates the vibrations transmitted from the previous stage to the next one. In this scheme, coupling factors of about 1% are expected: a conservative number which takes into account all the possible mechanical and geometrical causes.

The working principle is that one of the cascade of N oscillators described in section 2.5.1: according to equation (2.27), well above the highest resonant frequency, the vibrations are attenuated by a factor C/f^{2N}, where the constant C is the product of the square of the N resonant frequencies of the system.

Horizontal attenuation. For the movements in the horizontal plane, i.e. the working plane of the interferometer, the superattenuator acts as a pure multi–stage pendulum: each stage holds the next one by means of a steel wire. In order to decrease the frequency detection threshold, it is necessary to reduce the resonant frequencies of the chain and thence to increase the length of the pendula. Practical limitations have led to the choice of a chain of five pendula with a total length of about 7 m. The normal modes of the multi–stage pendulum have resonant frequencies ranging from 0.16 Hz to about 2.5 Hz and the required attenuation should be provided starting from 4 Hz.

Rotational modes. A chain of suspended extended masses acts as a chain of oscillators also in the angular degrees of freedom, providing a strong attenuation of the rotational motions above its resonant frequencies. In order to reduce the frequencies of the rotational modes of the chain around the vertical axis well below the detection band, each filter is a large diameter cylindrical tank, exhibiting a high momentum of inertia. Moreover, the diameters of the suspension wires have been reduced as much as possible (few mm) so to decrease their return torque which opposes to the rotation of the chain and which determines its rotational resonant frequencies. The coupling between linear and rotational modes is minimized by suspending each stage in a fully concentric way so that only very small torques can be exerted on the chain.

The frequencies of the tilt modes of each filter, that are the rotational modes around the two horizontal axes, can be reduced by minimizing the distance between the clamping points of the two steel wires connecting the filter to the neighboring ones. Moreover, the wires are attached as close as possible to the center of mass in order to reduce the arm of the reaction torque.

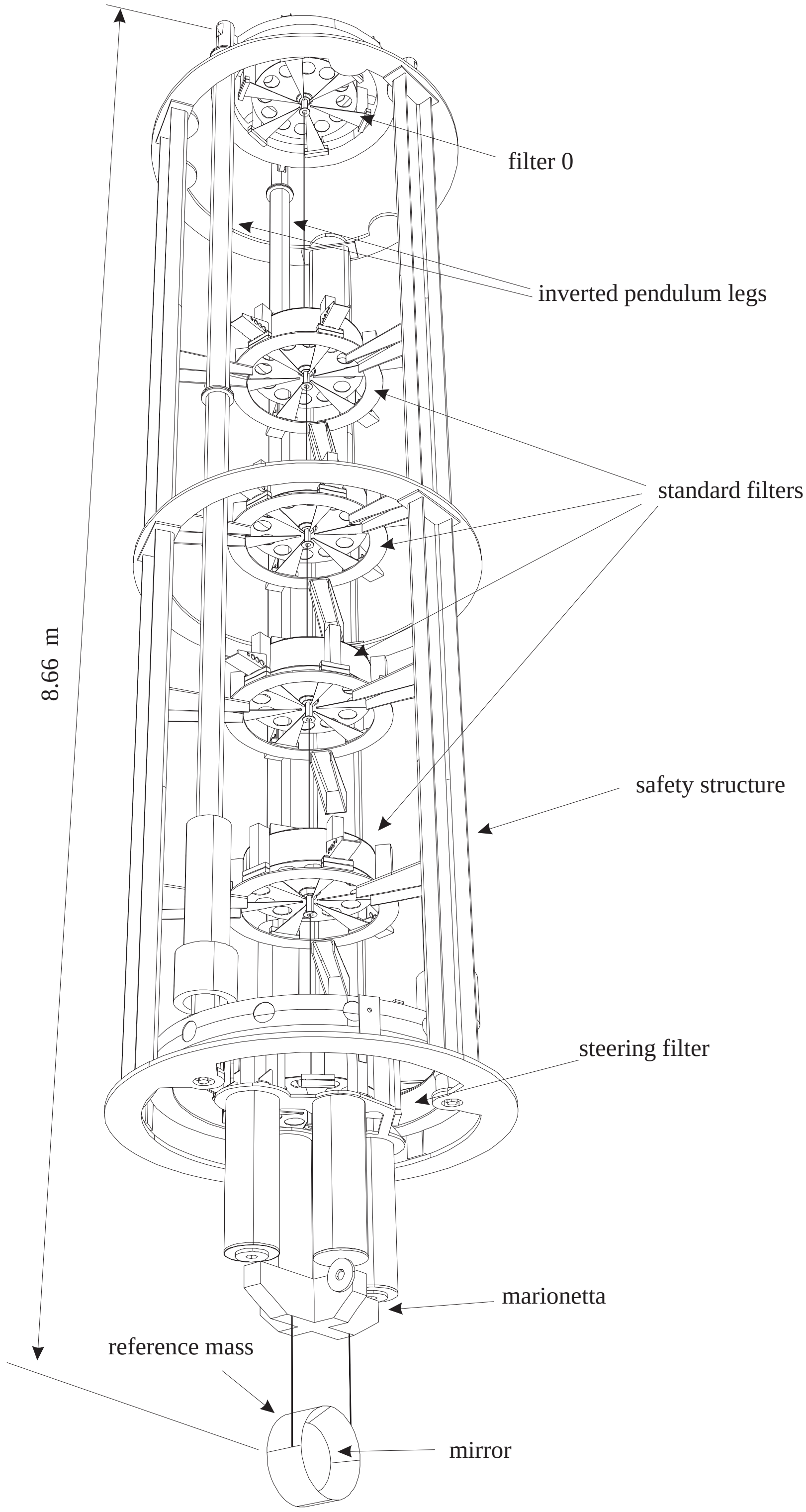

Figure 4.2: *View from below of the VIRGO superattenuator. We can distinguish two of the three legs of the inverted pendulum and, from the top to the bottom, the filter 0, the standard filters 1 to 4, the steering filter, the marionetta and the mirror–reference mass system. The safety frame surrounding the suspension system is also visible.*

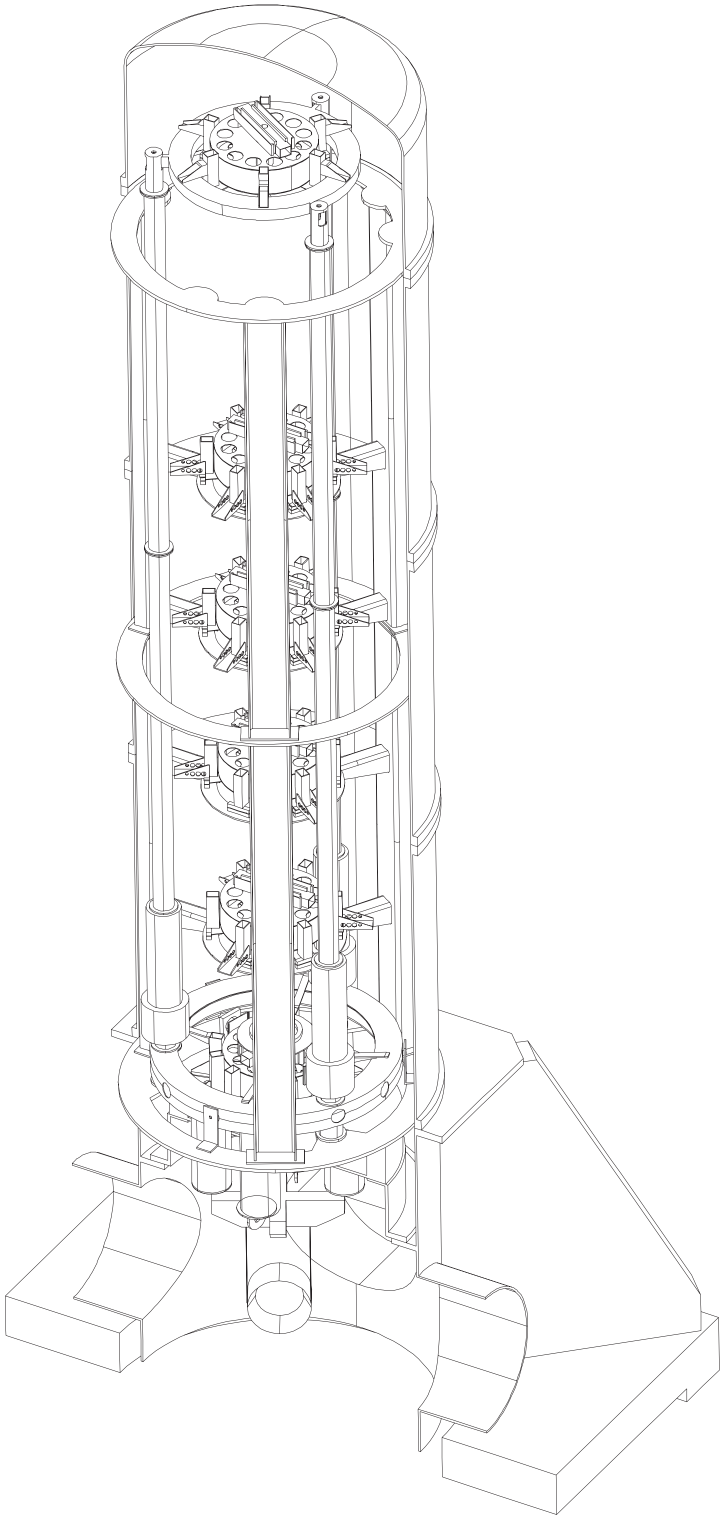

Figure 4.3: *View of the superattenuator inside its vacuum chamber.*

Thanks to these arrangements, the angular oscillations show resonant frequencies lower than 1 Hz.

Vertical attenuation A chain of simple pendula does not attenuate the vertical vibrations of the suspension point. The vertical attenuation is obtained by endowing each filter of a series of cantilever, triangular shaped, steel blades (hereafter called *blades*) acting as springs. They are arranged in a converging set and the next stage of the chain is hanged to their tips. So we have a chain of mechanical oscillators whose resonant frequencies are ranging from 1.4 Hz to 7 Hz. In the next chapter it will be shown how it is possible to reduce all these frequencies below 2.5 Hz as well as for the horizontal directions.

The whole superattenuator chain, shown in fig. 4.2 and fig. 4.3, is made of four *standard filters* plus a modified one, called *steering filter*, which supports the control system for the optical payload: the *marionetta* sustaining the *mirror–reference mass* system. The upper extremity of the chain is connected to a *pre–isolator stage* consisting of a three–legs *inverted pendulum* supporting the *filter 0* . The entire system is surrounded by a safety structure, named *safety frame*.

4.1.2 Active control

The seismic motion of the suspension point is amplified at the resonant frequencies of the superattenuator chain, leading to large resonant oscillations of the mirror. Moreover, at very low frequencies, motions due to both local thermal effects and tidal deformations are completely transmitted by the suspensions. The rms motion of the mirrors, along the beam direction, results to be several orders of magnitude beyond the maximum rms displacement tolerable for the interferometer locking (10^{-12} m, see section 3.2).

In order to compensate for these motions one must control the position of the mirror by sending correction signals to suitable actuators. This control cannot be performed by acting directly on the mirrors because of the finite dynamic range of the digital electronic system. In particular, the maximum force one can apply in proximity of the mirror is limited by the DAC card used to convert the digital correction signal to the analog one which is sent to the actuators for the mirror positioning. Compensation forces corresponding to displacement of the mirror along the beam larger than one micron, even if in quasi DC, would induce a large electronic noise floor into the detection band. This noise floor affects the driving currents of the actuators causing mechanical vibrations of the components to which the force is applied. If large forces were exerted too close to the mirror, these vibrations would not be filtered enough and they would be almost entirely transmitted to the mirror, so limiting the antenna sensitivity.

Such considerations have imposed to adopt a control strategy in which the compensation forces are exerted in three *control points* along the chain:

1) from the safety frame to the pre–isolator stage;
2) from the steering filter to the marionetta;
3) from the reference mass to the mirror.

The active control of the mirror position is performed by acting on these three points in different bands of frequency and different dynamic ranges. The very low frequency motions (from DC to 100 mHz) are compensated at the pre–isolator level. Here, large forces can be exerted since the high frequency noise injected is filtered by the superattenuator chain.

At higher frequency, where the chain exhibits its resonant modes, it is hopeless to try to control the motion of the mirror by means of the top stage actuators. Indeed, roughly speaking, a too large delay would be introduced by the resonances of the system between the actuation force and the motion of the mirror. This implies that, above 100 mHz, the compensation has to be applied, in any case, downstream the chain, close to the mirror.

Because of the above mentioned dynamic constrain, we must be sure that the mirror residual motion, above 100 mHz, does not exceed the amplitude of one micron. To fulfill this requirement, an active damping of the resonant modes of the chain is performed at the pre–isolator level (see section 4.3). The control above 100 mHz is then divided into two bands: up to 1 Hz, the mirror position is controlled by means of the steering filter–maroinetta system and, above 1 Hz, the correction forces are exerted directly on the mirror from the reference mass.

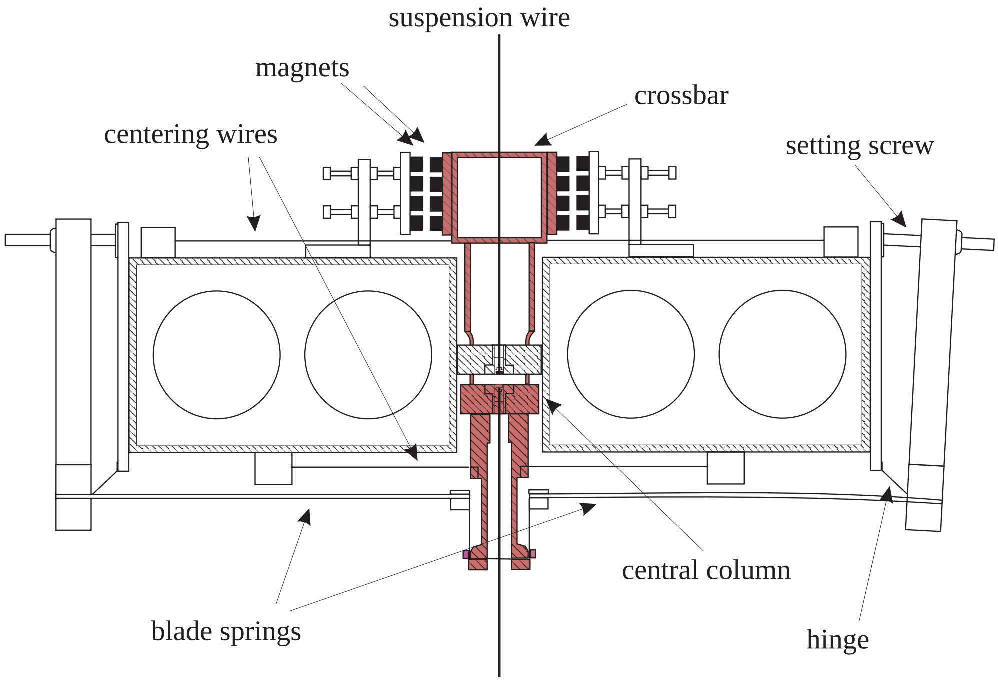

Figure 4.4: *Section of a standard filter. The part in red can move with respect to the body of the filter.*

4.2 Standard filters

The section of a standard filter is shown in fig. 4.4. The main body of the filter is a rigid steel cylinder 100 kg weigh, 70 cm diameter and 18.5 cm height. This one forms the fixed part of the mechanical filter and is suspended to the previous stage by means of a steel wire 1.3 m long and whose diameter ranges from 1.85 to 4 mm, according to the load. As shown in fig. 4.2, the distance between filter 0 and filter 1 is larger than 1.3 m so to allow the insertion of an additional filter, if necessary.

The basis of the triangular blade spring for the vertical attenuation are clamped to the outer circumference of the bottom of the cylinder. The tips of the blades are connected to a *movable central column* which is constrained, by means of two systems of four centering wires, to move only in the vertical direction into the central pot of the main cylinder.

The central column supports a *crossbar* which extends over the top of the filter body and to which the inner matrices of the *magnetic antispring* are fixed (see next chapter). To the central column it is clamped the wire suspending the next stage.

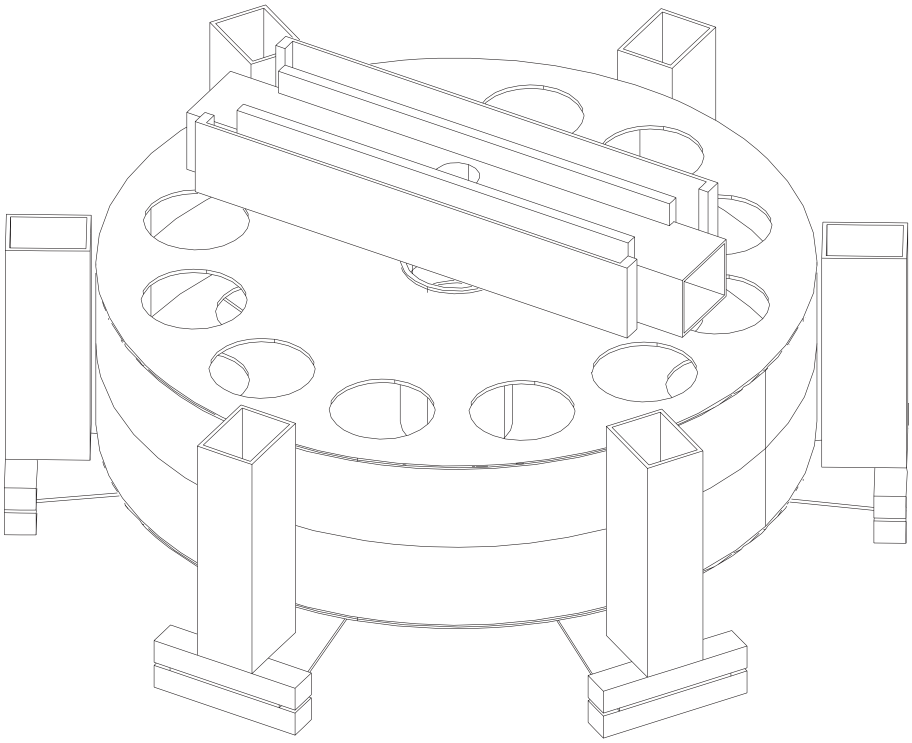

Figure 4.5: *Top view of a standard filter.*

The tips of the blades, the central column, the crossbar and the suspension wire form the moving part of a vertical oscillator loaded with the weight of the stages below. The main vertical mode, useful for the vertical attenuation, is at 1.4 Hz without the antispring. Since this is a complex system, other resonant modes are present. These modes limit the attenuation performances so they have to be damped by means of special absorption devices described in the following of this thesis.

The blade springs are pre–bent in order to assume a straight horizontal configuration once loaded (see fig. 4.7). Each blade is designed to have a nominal load ranging from 40 to 90 kg and the triangular shape guarantees a uniform distribution of the stress in order to minimize the maximum internal stress. The number of blades for each filter ranges from a maximum of 12 to a minimum of 4 according to the position of the filter along the chain and therefore, to the load they have to hold. The choice of the best material for the realization of the blades (and, in general, of all the stressed components of the superattenuator) is also a topic of this thesis.

The position of the movable part of the filter with respect to the main body can

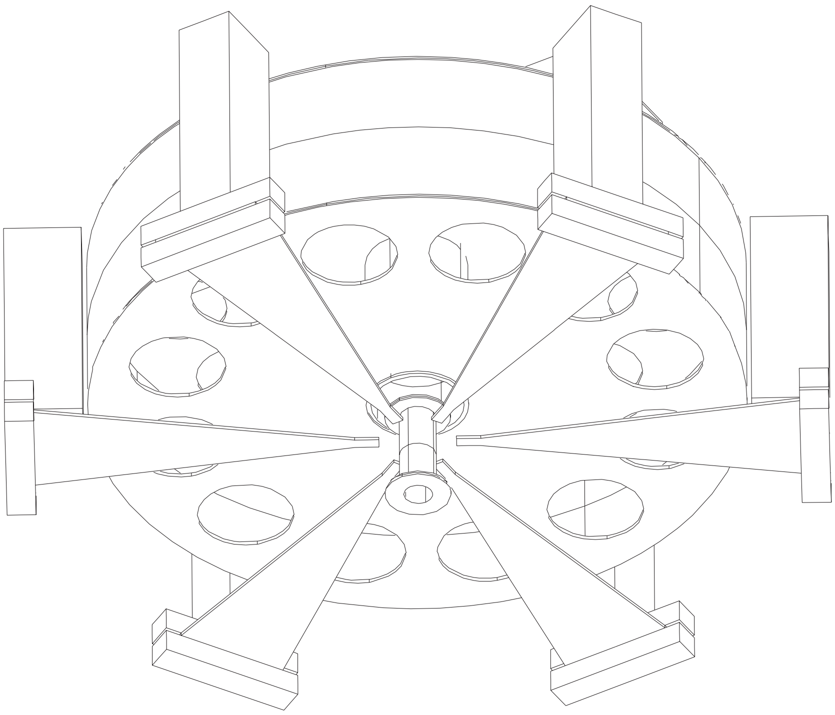

Figure 4.6: *Bottom view of a standard filter.*

be adjusted by changing the slope of some blades (*movable blades*) through suitable setting screws. A further fine remote adjustment is obtained by using the so called *fishing rod*. This device consists of a soft blade spring connected to the crossbar through a thin wire (here is the affinity with the fishing tool) and working in parallel to the other blades: a stepping motor can change the slope of the fishing rod and the remote positioning of the movable part of the filter can be achieved with the accuracy of few μm within a range of some mm. A Linear Variable Differential Transformer (LVDT) is used to measure the position of the crossbar with respect to the filter body.

4.3 Pre–isolator stage

The chain of mechanical filters is suspended to an ultra–low frequency pre–isolator stage. Beside providing a large reduction of the intensity of the seismic noise exciting the chain normal modes, the very softness of an ultra–low frequency stage makes it the ideal platform to apply the active damping of the resonant modes of the chain.

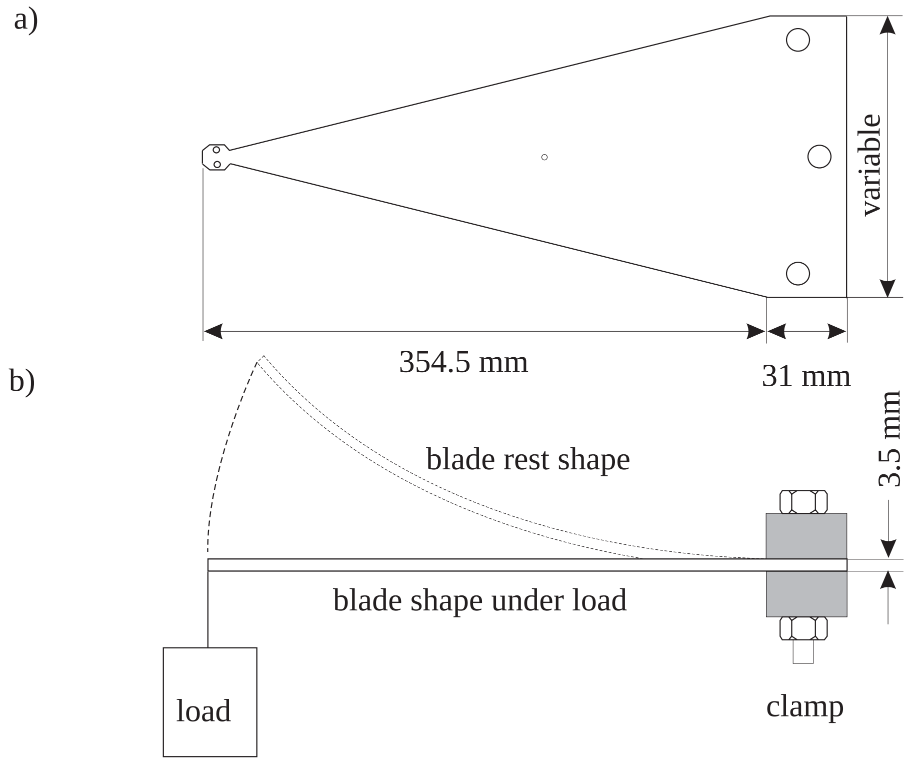

Figure 4.7: *Triangular shaped blade spring of VIRGO mechanical filters; a) upper view; b) side view: the suitable pre–bending assures a straight shape once the blade is loaded so it acts as a vertical spring.*

Moreover, it makes it possible to move the entire chain over the long period range using gentle coil–magnet actuators with low power consumption.

The pre–isolator stage is itself an x, y, z and θ_z (i.e. the rotation around the vertical axis) oscillator with a much lower resonant frequency (about 30 mHz) for the horizontal translation modes. In the horizontal directions the attenuation is performed by means of an *inverted pendulum*[40] composed by three rigid columns (legs), 6 m tall, each connected to the ground through a flexible joint and supporting a top table. A modified mechanical filter, called *filter 0*, placed on the top table exerts the vertical attenuation.

In order to adjust the horizontal offset of the chain, motorized springs act on the legs of the inverted pendulum from the safety frame. An endless screw is driven by a stepping motor to adjust the vertical position of the chain from the crossbar of the filter 0. Three LVDT sensors measure the position of the top stage with respect to

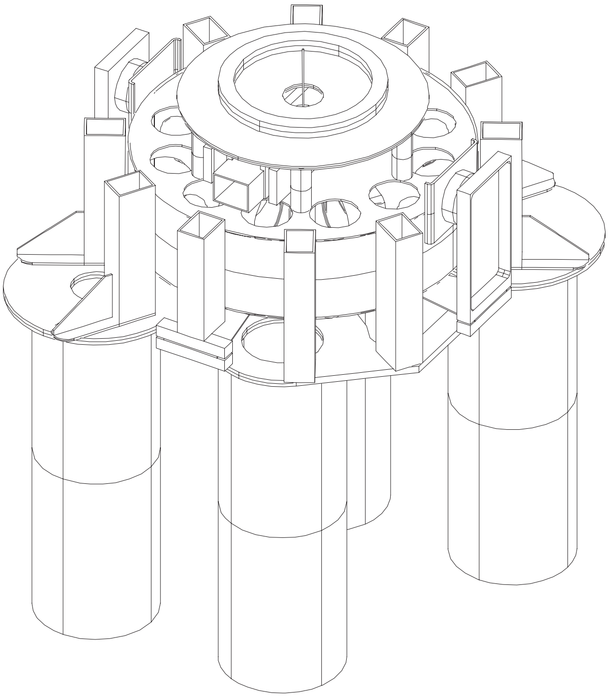

Figure 4.8: *View of the steering filter with its four legs for the control of the marionetta.*

the safety frame while the vertical position is read by means of a CCD camera looking at the mirror.

The active damping is performed by means of three horizontal and two vertical coil–magnet pairs placed between the top table and the safety frame and between the body of the filter 0 and its crossbar, respectively. Since the LVDT signals refer to a noisy structure, the sensors to drive the actuators are home made accelerometers (inertial damping).

4.4 Steering filter

The last filter of the chain is commonly called *filter 7* (see fig. 4.8) since the former superattenuator was designed to have 7 filters. It is basically a standard filter but it is equipped with devices to fulfill additional features. Four columns about 1 m long extend from the bottom of the filter, each supporing a driving coil facing a corresponding small magnet fixed to each arm of the marionetta. By driving the coils with proper currents, forces and torques can be applied to the marionetta to control

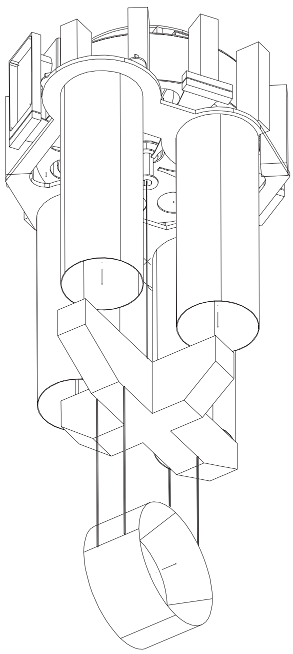

Figure 4.9: *The marionetta and the mirror–reference mass system suspended to the steering filter.*

the position of the mirror within the band of 0.1-1 Hz.

The angular positioning of the filter in the horizontal plane is achievable by means of motorized setting screws and ceramic balls bearings which allow both the rotation of the filter with respect to its suspension wire and the rotation of the marionetta with respect to the filter itself.

4.5 Optical payload

The marionetta hanging from the steering filter is the last stage of this complex suspension system for the optical components of the interferometer. It is essentially a cross shaped structure supporting the mirror and the reference mass through two couples of looping steel wires (see fig. 4.9). The aim of the marionetta is to allow to finely control the position and the alignment of the mirror for the interferometer locking.

Final adjustments of the position of the mirror along the beam direction above 1 Hz are applied directly to the mirror from the reference mass which surrounds it.

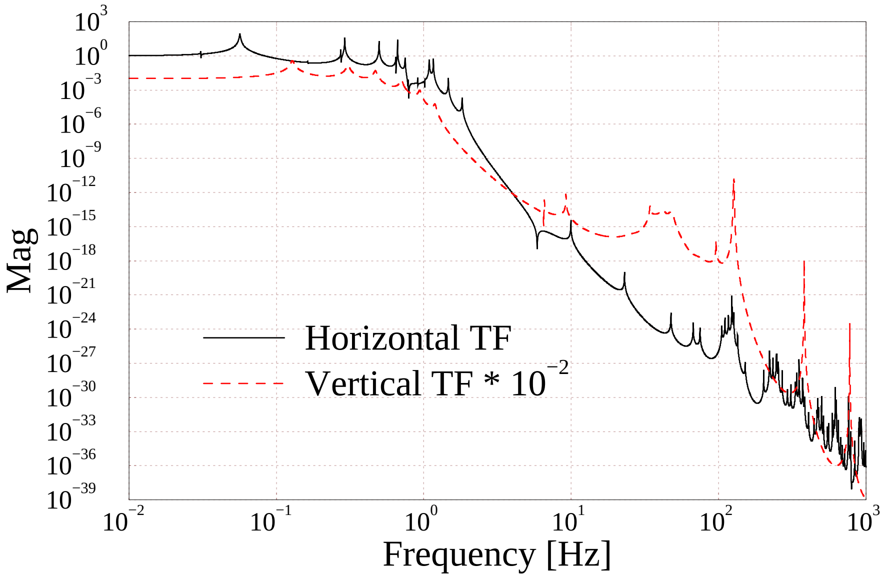

Figure 4.10: *Simulated superattenuator transfer function along the beam direction. A vertical–horizontal coupling factor* $\alpha_{\mathrm{mech}} = 0.01$ *has been assumed.*

The reference mass is suspended by the superattenuator and therefore, it is seismic noise free as well as the mirror. The position control is exerted by means of four coils mounted on the reference mass facing four magnets placed on the mirror. The reference mass is made of dielectric material in order to avoid Foucault current dissipation that would increase the thermal noise affecting the mirror.

4.6 Superattenuator expected performances

In fig. 4.10 the calculated transfer function of the superattenuator along the beam direction is shown. The expected performance of the suspension chain is the result of a six degrees of freedom simulation code, SIESTA[41], in which a vertical–horizontal coupling factor of 0.01 has been assumed, while the coupling between the beam direction and the other ones has been considered negligible. Above 10 Hz the attenuation performance is degraded by the internal resonant modes which will be treated in chapter 6: a *plateau* is found rather than a f^{-2N} behaviour.

The superattenuator is expected to completely fulfill its specifications. The plateau is in a range where the residual seismic noise is largely dominated by thermal noise, as

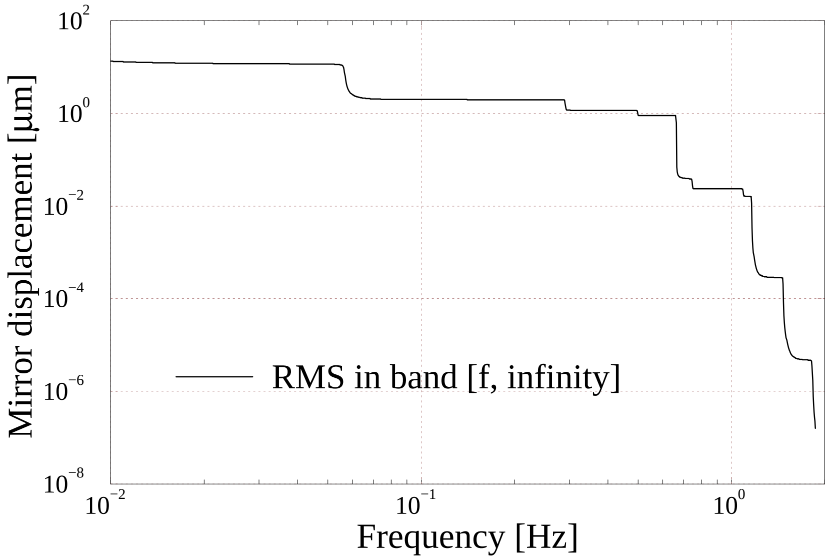

Figure 4.11: *Integrated rms motion of the mirror as expected from the calculated superattenuator transfer function of fig. 4.10.*

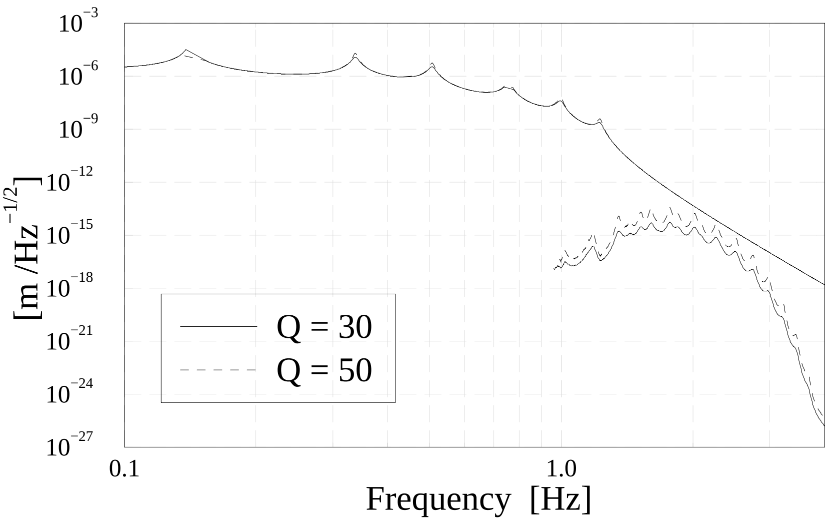

Figure 4.12: *Effect of the antisprings nonlinearities on the superattenuator vertical performance for two different values of the Q of the vertical resonances.*

shown in fig. 3.3. Moreover, the internal vibrations responsible of the peaks between 40 and 100 Hz will be efficiently damped by passive absorption devices developed by the author and described in chapter 6. The seismic noise starts dominating over other noises at $f < f_{\min} = 3$ Hz. We consider this as the *low frequency threshold* of the VIRGO detection band.

As discussed at the beginning of this chapter, the seismic noise is attenuated by a huge factor above 10 Hz, but it is amplified at the resonant frequencies. This causes large resonant motions of the mirror. Fig. 4.11 shows the expected rms motion of the mirror without the active damping of the superattenuator normal modes. Such a seismic excited motion would be too large whit respect to the allowable dynamic range (less than 1 μ above 100 mHz) of the payload control, hence the necessity of the active damping.

Non linear effects have been considered in the simulation[42]: fig. 4.12 shows that the effect of up–conversion associated to the quartic term of the antisprings potential is dominated by the linear behavior of the system.

Chapter 5

Vertical attenuation: the magnetic antispring

The mechanical and geometric characteristics of the filters are bound by practical limitation. Consequently, the attenuation performances are limited as well, since they are determined by the resonant frequencies of the system. The pendulum frequency of the filter is bound to the length of the suspension wire and this one is limited by the available vertical space in the vacuum chamber: the achievable frequency is of about 0.5 Hz. The whole chain has all the horizontal normal modes below 3 Hz exerting the required attenuation starting from about 4 Hz.

On the other hand, the vertical attenuation of the chain shows a higher threshold frequency, at about 7 Hz. Indeed, the vertical resonant frequency of a filter is of about 1.5 Hz, well above the horizontal one. This would limit the low frequency sensitivity of the interferometer because of the coupling between the two degrees of freedom.

The reduction of the vertical resonant frequencies of the chain is made feasible by mounting on each filter a set of permanent magnets (*magnetic antispring*) which allows the lowering of the vertical resonant frequency of each filter to less than 0.5 Hz[43]. It comes out that the threshold frequency of attenuation is lowered from 7 Hz to about 4 Hz.

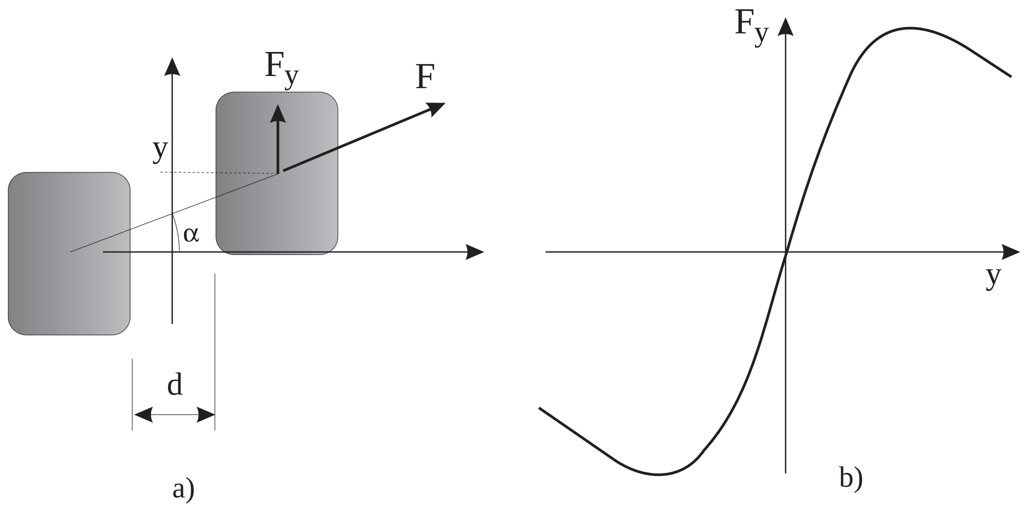

Figure 5.1: *a) Working principle of the magnetic antispring: the two facing magnets are constrained to move along the vertical direction (y axis). b) Qualitative behaviour of the force between the magnets as a function of the vertical offset y.*

5.1 The magnetic antispring

The working principle of the magnetic antispring is based on the repulsive force reciprocally exerted by two magnets having horizontally opposite magnetic moment and constrained to move only along the vertical direction. In fig. 5.1 a) it is sketched what happens: the magnet A exerts on the magnet B in the position y, a repulsive force whose vertical (y direction) component can be written:

$$F_y(y) = F(y) \sin \alpha, \tag{5.1}$$

where $F(y)$ is the module of the force and we have indicated only the dependence on the y coordinate. The horizontal separation d between the magnet is fixed and α is the angle the force direction forms with the horizontal axis. The behaviour of F_y versus the y coordinate is qualitatively shown in fig. 5.1 b): within an interval depending on the magnets separation the repulsive force increases with the absolute value of y, then it decreases until it vanishes. It is only in twice this interval that the system exhibits the antispring feature. For small displacements δy around a point y of the above mentioned interval, the (5.1) can be linearized:

$$F_y(y + \Delta y) = F_y(y) + \frac{\partial F_y(y)}{\partial y} \Delta y, \tag{5.2}$$

where the derivative in the right hand term is positive and it is equivalent to a "negative stiffness" whose absolute value will be indicated with $k_{as}(y)$.

Actually, the antispring system consists of two pairs of matrices of permanent magnets in repulsive configuration which act in order to reduce the stiffness of the vertical oscillator near its equilibrium point. As shown in fig. 4.4, two matrices are mounted on the top of the filter body in such a way to face the other two which are fixed to the crossbar and therefore are solidal with the moving part of the filter. Using two pairs of matrices allows to get a strong vertical anti–stiffness without applying resulting lateral forces to the crossbar.

Each matrix of the antispring is made of two or four lines of ferroxdure magnets, $6 \times 2 \times 1.5$ cm^3, producing a nominal magnetic field of 0.36 Tesla in the direction parallel to the 1.5 cm dimension. We decided to put each line of magnets in the matrix with the sense of the magnetic field opposite both to that of the neighboring line in the same matrix and to that of the line facing on the matrix in front of it. This configuration allows to minimize the total magnetic moment dipole of the system, reducing the coupling with external magnetic field.

The number of the magnets in each line, as well as the number of the lines, depends on the required anti–stiffness which depends on the stiffness of the blades and therefore, on the load to be supported by the filter the antispring are mounted on[30]. The fine regulation of the anti–stiffness, during the assembling phase, is obtained by means of setting screws which allow to vary the distance between the matrices mounted on the filter body and the ones on the crossbar.

The antispring acts in parallel to the blade springs. Let us indicate with y the vertical displacement of the movable part with respect to the filter body, choosing as origin of the axis the position where the antispring matrices are perfectly aligned ($y = 0$ in equation (5.2)). The resulting vertical force applied to the central column will be:

$$F_R(y) = -Mg + F_y(y) - k_s \cdot (y - l_0), \tag{5.3}$$

where Mg is the load of the filter, K_s the stiffness of the blade springs and l_0 represents the rest length of the blade springs. If y_0 is the equilibrium point, for small displacements Δy around it, the equation of motion of the mass M results, according to (5.2):

$$M\ddot{\delta y} = -\left[k_s - k_{as}(y_0)\right]\delta y, \tag{5.4}$$

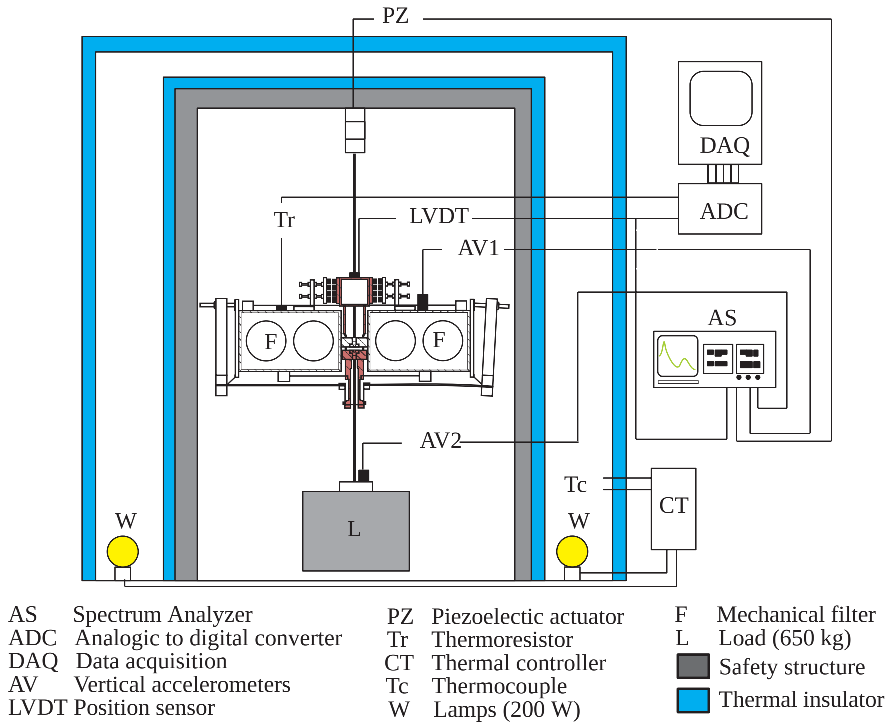

Figure 5.2: *Experimental set up for the measurement on the mechanical filter prototype.*

which admits oscillating solution with frequency $f_0 = (1/2\pi)\sqrt{(k_s - k_{as})/M}$ when the condition $k_s > k_{as}$ holds. The validity of this approximation depends on how much rapidly k_{as} varies with the offset y between the magnets.

At $y = 0$ k_{as} has the maximum value and the minimum variation with the offset. The behaviour of the anti–stiffness depends on the horizontal separation between the magnets: the lower the separation the narrower the range in which k_{as} slowly varies with the offset. For too low values of this separation, the stability condition $k_s > k_{as}$ can be no longer satisfied in an interval of y included between regions where it still holds, giving rise to a *mechanical bistability*. To improve the behaviour at low frequency we can increase the number of the magnets. In this way we obtain the same frequency with a larger horizontal separation since the repulsive force has been increased.

On the other hand, it is sufficient to take the vertical resonant frequency of each filter just below the respective pendulum resonant frequency (0.5 Hz) so that all the vertical modes of the chain will have resonant frequencies below that of the horizontal

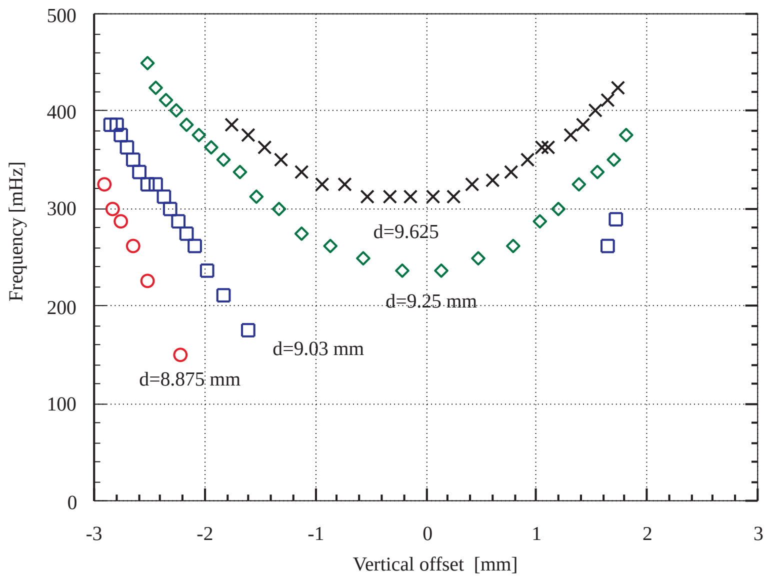

Figure 5.3: *Vertical resonant frequency of the mechanical filter versus the equilibrium point position for different values of the magnets separation d. The two lowest values, have no equilibrium points near zero (bistability condition).*

ones and the sensitivity of the interferometer will be limited, below 4 Hz, by the horizontal seismic noise.

According to the results of the survey described below, the number of the magnets to mount on each filter has been chosen so that k_{as} has a pretty linear behaviour within a range of at least 2 mm around the zero offset.

5.2 Filter prototype

For the full characterization of the mechanical filter, a detailed survey has been carried out by the author on a filter prototype equipped with 12 blades[44]. The experimental setup is sketched in fig. 5.2. The filter with its load of about 650 kg is enclosed in a double box of thermal insulator to ensure an enviroment thermal stability within a tenth of degree. A piezoelectric actuator can excite the system in the vertical direction allowing the measurement of the transfer function in that direction. The signal of two accelerometers placed on the filter body and on the load, respectively, are collected and processed by a HP spectrum analyzer. The position of the moving part of the filter is also measured by means of an LVDT sensor whose signal is sent both to the

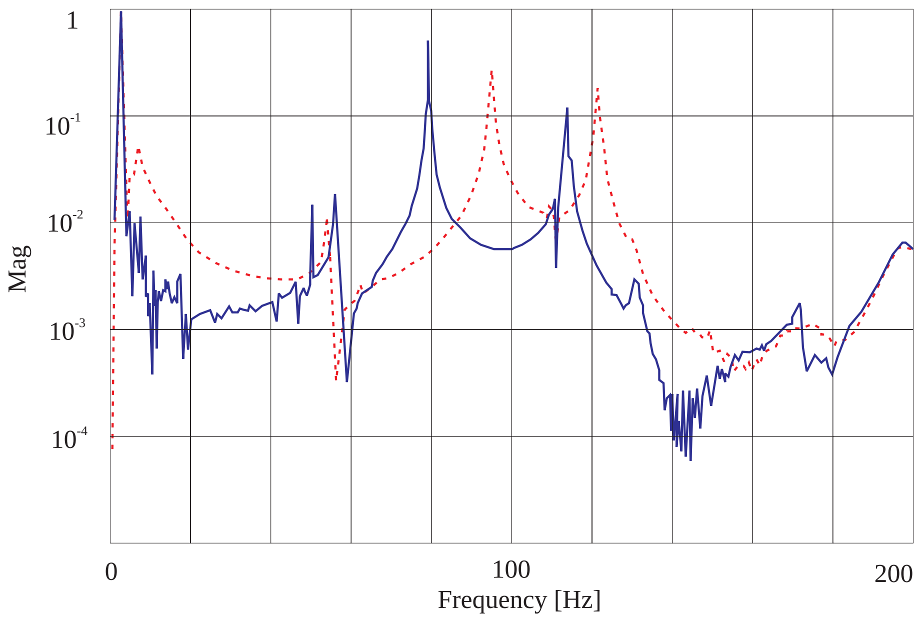

Figure 5.4: *Module of the vertical transfer function of the filter with the antispring (solid line). Below 20 Hz the attenuation is better of about a factor 10 than the case without the antispring (dashed line).*

spectrum analyzer and to an ADC converter connected to a computer.

In order to study the behaviour of the magnetic antispring described in the previous section, a series of measurements of the main vertical resonant frequency has been done for different values of the separation between the matrices of magnets and for different operating temperatures.

5.2.1 Dependence on setting point

The results of the measurements about the dependence of the main resonant frequency on the vertical offset between the magnets are shown in fig. 5.3. The measurements have been repeated for four different values of the separation between the matrices at a temperature of 30 °C. The curves show as the antispring can be easily set to reach the aimed goal: to take the main vertical resonant frequency below the limit of 0.5 Hz.

Fig. 5.4 shows the effect of the antispring on the vertical transfer function of the filter (solid line). The distance between the matrices is set to have a resonant

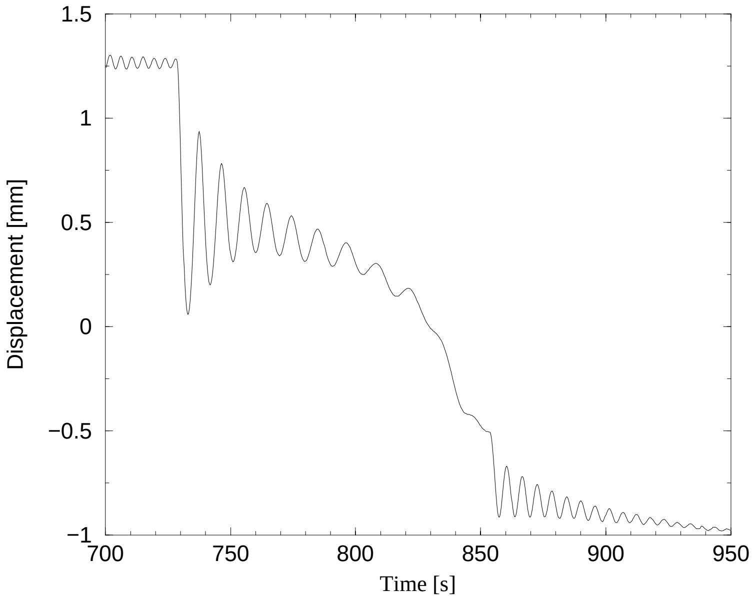

Figure 5.5: *Mechanical bistability in a measurement at 26.3 °C. The system oscillates around an equilibrium point which is slowly lowered by thermal drift. Once the bistability zone at about -0.1 mm is reached, the system jumps to the other equilibrium point at about -0.5 mm. At t = 855 s we newly excite the system.*

frequency of about 0.4 Hz when the magnets are perfectly aligned. By the comparison with the vertical transfer function of the bare filter (dashed line) is evident the enhancement of the attenuation at low frequencies. Starting from about 20 Hz the attenuation performance of the filter becomes worse, either with or without the anti-spring, because of the inner resonant modes of the filter. In the next chapter we will deal with this subject.

From the resonant frequency behaviour one can deduce the dependence of the anti–stiffness on the relative position of the magnets. When they are perfectly aligned ($y_0 = 0$), k_{as} is maximum and the frequency assumes its minimum value (*minimum vertical frequency*). When the horizontal separation decreases, the curves will become narrower and the anti–stiffness will vary more rapidly with the magnet offset; moreover, its maximum value increases.

For the lower curves in fig. 5.3, the magnets separation is too small and there are no stable equilibrium position near to zero: here the system experiences a mechanical bistability. What happens is shown in fig. 5.5 which reports the recording of the

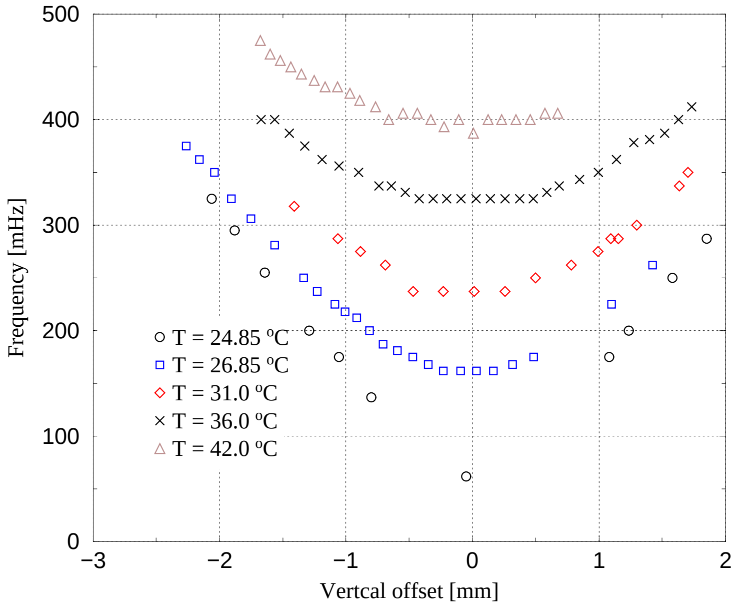

Figure 5.6: *Vertical resonant frequency of the mechanical filter versus the equilibrium point position at different temperatures for the 7×3 magnets antispring. The separation of the matrices is 9.25 mm.*

crossbar displacement in the neighborhood of the zone of instability. The equilibrium point slowly goes down because of thermal drift (see next section), then the system jumps to the another equilibrium point in a symmetric position with respect to the "zero" of the magnets (different from the zero of the scale).

5.2.2 Dependence on temperature

The permanent magnetic field of the antispring is very sensitive to the temperature variation: the magnitude of the field will decreases (increases) when the temperature increases (decreases). Two series of measurements at different temperatures have been done: the first one on an antispring with matrices of 7×3 magnets and 9.25 mm horizontal separation (see fig. 5.6), the second one on an antispring with 5×3 magnets matrices separated by 4.5 mm (see fig. 5.7).

The values of the measured minimum vertical frequencies are plotted versus the temperature in fig. 5.8, and we can deduce that the frequency varies almost linearly

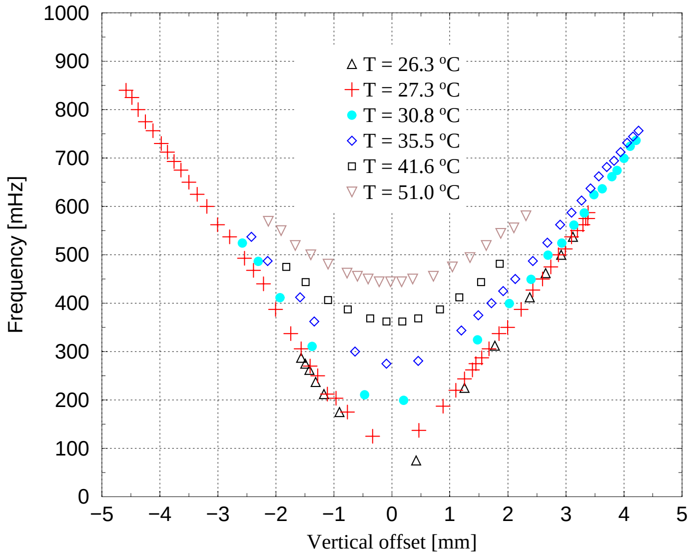

Figure 5.7: *Vertical resonant frequency of the mechanical filter versus the equilibrium point position at different temperatures for the 5×3 magnets antispring. The matrices separation is 4.5 mm.*

within the interval of interest. The relation

$$\frac{\Delta f_{\min}}{\delta T} = \frac{15\text{mHz}}{{}^{\circ}\text{C}} \pm \frac{2\text{mHz}}{{}^{\circ}\text{C}} \tag{5.5}$$

is in good agreement with the dependence on temperature of the anti–stiffness expected to be of about 0.4%/°C[45].

Actually, the thermal variation of the frequency is the sum of the variations of both the magnets strength and the blades stiffness. Nevertheless, the measurement of the latter has given the value of $\frac{\Delta K}{K \Delta T} = \frac{2.1 \cdot 10^{-4}}{{}^{\circ}\text{C}}$ (see chapter 7), negligible with respect to the former.

Moreover, the temperature variation indirectly affects the frequency through the thermal drift of the equilibrium point. As shown in the next section, the temperature variation induces the variation of the equilibrium position as a consequence of the change of the total stiffness. Therefore, the variation of the frequency contains also a contribution due to the k_{as} dependence on y.

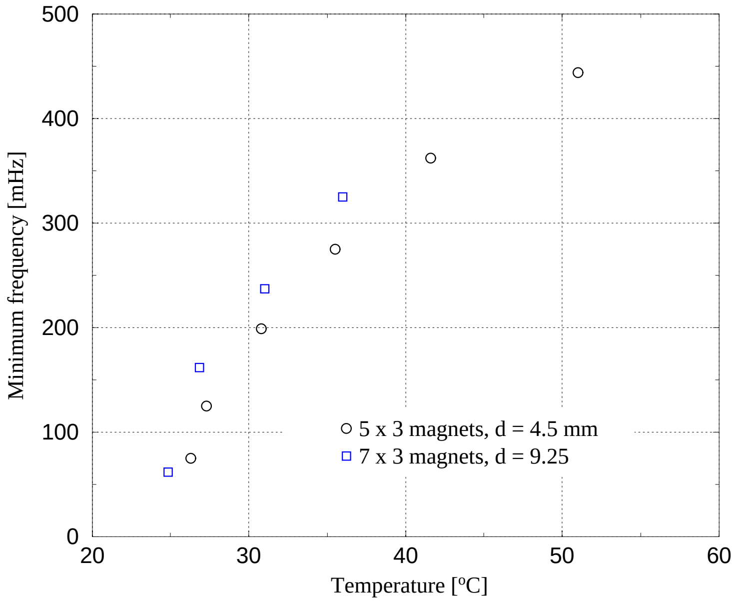

Figure 5.8: *Minimum vertical frequency versus temperature.*

5.2.3 Quality factor

The characteristic decay time τ of the vertical oscillation has been evaluated from the acquired data about the displacement of the moving part of the filter with respect to the fixed one[49]. In fig. 5.9 the values of the decay time τ_i are plotted versus their correspondent frequencies $f_{0,i}$. The data refers to the two series of measurements done to determine the temperature dependence.

Both the two group of measured τ show a linear dependence on the frequency f_0 which means that the quality factor of the oscillator $Q = \pi f_0 \tau$ behaves like the square of the resonant frequency. This experimental evidence disagrees with the viscous damping mechanism where the decay time is independent on resonant frequency. In fact our data agree with the description of the damping due to internal friction of the material[20]. The mathematical formulation of this phenomenon is obtained by adding an imaginary component to the stiffness k_s of the blades spring:

$$k_{tot} = k_s(1 + i\phi) - k_{as} = (k_s - k_{as})(1 + i\phi') \tag{5.6}$$

with

$$\phi' = \frac{k_s \phi}{k_s - k_{as}} = \phi \frac{f_s^2}{f_0^2}, \tag{5.7}$$

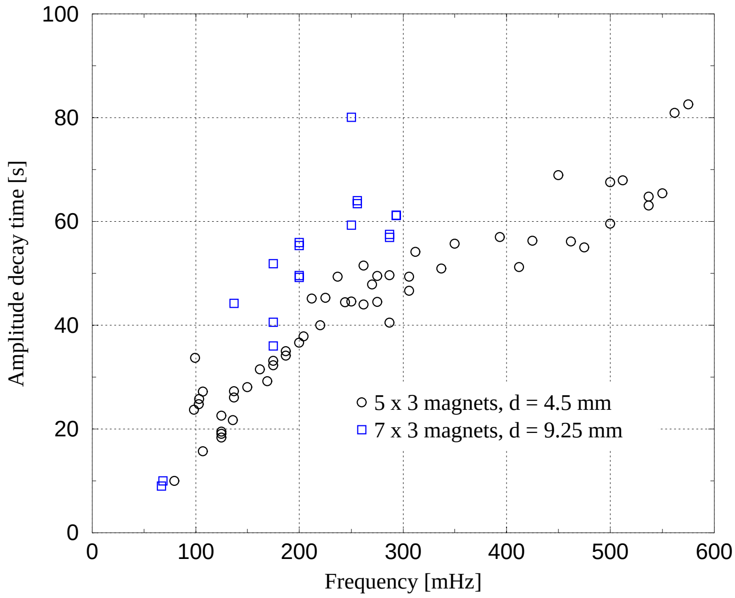

Figure 5.9: *Decay time of the oscillations versus resonant frequency for two different configurations of the magnetic antispring.*

where f_s is the vertical resonant frequency of the filter without the antispring. From the latter equation we can deduce the dependence on resonant frequency of the quality factor which is also defined as the inverse of the phase lag ϕ. By inverting the (5.7) we obtain:

$$Q(f_0) = \frac{f_0^2}{\phi f_s^2}. \tag{5.8}$$

Therefore, the origin of the damping has to be ascribed to internal phenomena of dissipation: internal friction of the blades, hysteresis of magnets and hysteresis of the mechanical supports of the magnets matrices.

The measured values of the quality factor are rather low. Nevertheless, having low values of Q is not a disvantage, at least on the upper stages of the superattenuator: low quality factors suppress the transmission of the soil vibration at the resonant frequencies of the chain. On the last stage, where the thermal noise can affect directly the mirror, high Q materials have to be preferred. By the way, other requirements, such as the low creep rate (see next chapter), have led our choice towards high Q materials for the realization of the blades and of the magnets supports.

5.3 Thermal stabilization

On the basis of the experimental data collected, relevant information about the stability of the superattenuator have been obtained; in particular it has been picked out the necessity of thermal stabilization within 0.1 °C[46, 47] inside the vacuum chambers containing the suspension systems so that the fluctuation of the vertical position of the mirrors do not overload the alignment system. Moreover, the thermal stabilization allows to eliminate the complex system of hydraulic adjustment of the filter designed for the previous version of the superattenuator[48].

Here we estimate the vertical displacement of the suspended mirror due to changes in the stiffness of the blade springs and magnetic antispring driven by temperature variations.

As the total vertical stiffness of a mechanical filter changes, a new equilibrium position is reached by its load. The equilibrium condition is:

$$K_s\,(y - l_0) - K_{as}y + Mg = 0, \tag{5.9}$$

where K_s and K_{as} are the blades and the antispring contribution to the total stiffness K_{tot}, respectively, y is the vertical displacement from the perfectly–faced–magnets position, l_0 is the rest length of the blade springs treated as linear springs and Mg is the filter load. The solution of (5.9) is easily obtained:

$$y_0 = \frac{K_s l_0 - Mg}{K_s - K_{as}}, \tag{5.10}$$

and can be differentiated in order to obtain the thermal drift of the equilibrium position:

$$\delta y_0 = \frac{\delta K_s\,(Mg - l_0 K_{as})}{(K_s - K_{as})^2} + \frac{\delta K_{as}\,(K_s l_0 - Mg)}{(K_s - K_{as})^2} \tag{5.11}$$

or, from the (5.10):

$$\delta y_0 = \frac{(l_0 - y_0)\,\delta K_s}{K_{tot}} + \frac{y_0 \delta K_{as}}{K_{tot}}. \tag{5.12}$$

In the real situation of the VIRGO mechanical filters we have $y_0 \ll l_0$ and we can approximate $l_0 - y_0$ with l_0 and $K_s \cdot l_0$ with Mg. So we can rewrite the (5.12) as:

$$\delta y_0 \simeq \frac{g}{(2\pi f_0)^2}\left(\frac{\delta K_s}{K_s} + \frac{y_0}{l_0}\frac{\delta K_{as}}{K_{as}}\right), \tag{5.13}$$

where the relation $K_{tot} = M(2\pi f_0)^2$ has been used. By putting into the (5.13) numerical values:

$l_0 \simeq 0.15$ m; $y_0 \leq 0.001$ m

$f_0 \simeq 0.4$ Hz

$\frac{1}{K_s}\frac{\delta K_s}{\delta T} \approx 2 \times 10^{-4}/°\mathrm{C}$

$\frac{1}{K_{as}}\frac{\delta K_{as}}{\delta T} \approx 4 \times 10^{-3}/°\mathrm{C}$

(the latter two coming from direct measurements), we can estimate the amount of vertical displacement δy_s due to the blades contribution:

$$\frac{\delta y_s}{\delta T} \simeq \frac{9.8}{(2 \times \pi \times 0.4)^2} \times 2.1 \times 10^{-4} \simeq 300\ \mu\mathrm{m}/°\mathrm{C} \tag{5.14}$$

and δy_{as} due to the magnets:

$$\frac{\delta y_{as}}{\delta T} \simeq \frac{0.001}{0.15} \times \frac{9.8}{(2 \times \pi \times 0.4)^2} \times 4 \times 10^{-3} \simeq 30\ \mu\mathrm{m}/°\mathrm{C}. \tag{5.15}$$

The total vertical displacement of the mirror due to the above described temperature variation is obtained by summing the contribution of all the six filters of the suspension chain. A big amount of vertical displacement cannot be compensated by the position adjusting systems whose range is of a few mm. Moreover, all the motor driven devices must be switched off during the data taking and this will further reduce the capabilities of position correction.

By the way, there is a stronger stability requirement on the resonant frequencies of the suspensions chain. Large thermal fluctuations of the frequencies cannot be tolerated by the feedback system for the locking and for the active damping. With a thermal stabilization within 0.1 °C, the residual thermal changes of the vertical frequencies remains inside the natural width of the peaks, making much simpler the locking and the active damping operations.

5.4 Assembling procedure

All the filters for the six VIRGO superattenuators plus the three short towers composed only by the filter 0 and the steering filter (a total number of 42 filters), are assembled and tested by the people of the suspensions group, whose the author is member. The filter assembling consists of well defined operations whose aim is to guarantee the best working configuration and to reduce to the minimum further adjustments once the filter is mounted in its final position along the chain. The setting of the antispring system is the most important of these operations.

The filter is suspended to a rigid structure and charged with its nominal load, then the load is made oscillate and the frequency is measured through a commercial accelerometer whose signal is sent to a spectrum analyzer. In order to evaluate the minimum resonant frequency, the magnets offset is changed by adding small calibrated weights ($\approx$ 100 g) to the filter load and the frequency is measured for each offset position. The contribution to the frequency variation due to the small changes of the load ($\Delta f/f \sim \sqrt{\Delta m/m}$), is negligible with respect to the variation due to the change of the antispring offset which, according to (5.10), results linearly dependent on the added load. In this way we obtain a curve of the resonant frequency versus the magnets offset, like the ones described in the previous section.

The filter is tuned to the desired vertical resonant frequency by setting the separation between the antispring matrices. It is impossible to get an accurate tuning of the filter because of this trial–and–error method but, on the other hand, it is not necessary. The requirement is to keep the vertical resonant frequency below the horizontal one (about 0.5 Hz) and far enough from zero in order to avoid instabilities. The conservative range between 300 and 400 Hz has to be considered acceptable. The temperature dependence of the resonant frequency is also taken into account by using the (5.5) to evaluate the frequency shift the filter will experience when it is put in its final operating location.

Chapter 6

Mechanical limits: internal modes

The internal modes of some elements of the VIRGO mechanical filters limit their performances. Around the frequencies of such modes the attenuation of the filters becomes worse so that the isolation from seismic noise is compromised. In order to damp these unwanted vibrations the filter structure has been designed to be rigid as much as possible; where it has not been possible to do it, i.e. blade springs and suspension wires, special dynamic absorption devices, hereafter called *dampers*, has been designed.

The dampers are mounted on the vibrating elements in order to attenuate the resonance. In this way we are able to keep the vertical transfer function of the filter below the required value in all the frequency region affected by the internal vibration we have dealt with (30-130 Hz).

Above 10 Hz, the vertical attenuation of a filter deviates from the $1/f^2$ behaviour since the non negligible mass of the blades. Even if we damp the internal modes, a sort of *plateau* remains between 30 and 100 Hz. Nevertheless, to keep the seismic noise well below the thermal one which dominates this frequency region, this worse attenuation is acceptable if we consider the trend of the seismic noise (see equation (2.20)). For instance, at 10 Hz the linear spectral density of the thermal excited displacement of the mirror is about 10^{-17} m/$\sqrt{\text{Hz}}$ while for the soil vibrations we have about 10^{-9} m/$\sqrt{\text{Hz}}$. The last value has to be multiplied by the vertical–horizontal coupling factor (about 1%), this means that a vertical attenuation of 10^7 by the entire suspension (less than 20 for each filter), will be sufficient to reach our goal. Things get better for higher frequency.

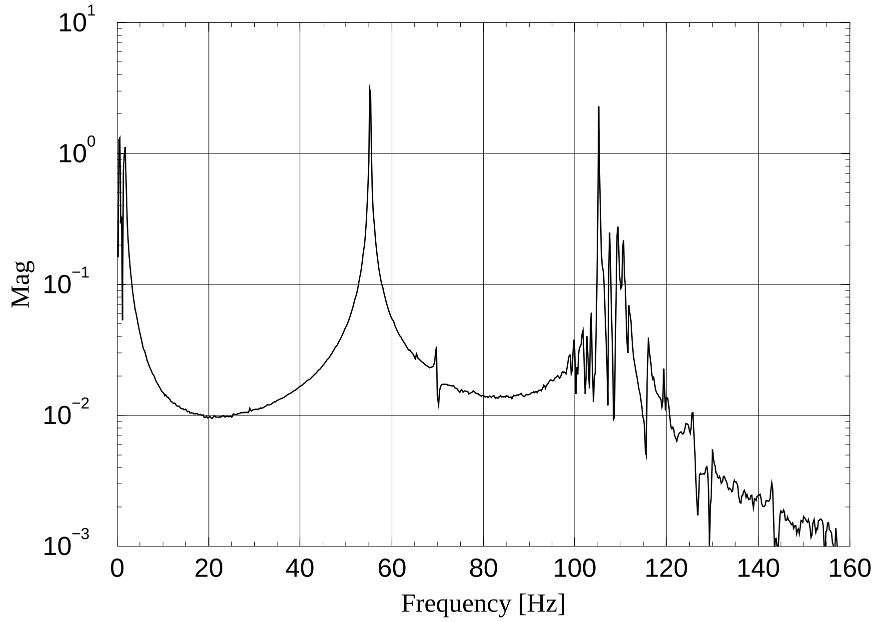

Figure 6.1: *Vertical transfer function module of the filter 1 measured on the prototype chain. The peak at 55 Hz is due to the crossbar mode; the first flexural modes of the blade springs is responsible of the structure aruond 105 Hz.*

6.1 Internal vibrations

In fig. 6.1 the vertical transfer function (VTF) of a filter is shown. The measurement is taken on the filter 1 operating in the prototype superattenuator built in INFN–Pisa laboratory, by placing two commercial accelerometers on the top vessels of the filter 1 and of the lying below filter (filter 2), respectively. The signals are sent to a spectrum analyzer which automatically calculates the transfer function. The system is excited by driving with white noise the two vertical coils for the active damping placed on the top stage of the superattenuator.

What we can see in the VTF is that, beside the main resonant frequency, other two relevant peaks are present. The first one at 55 Hz is due to the next stage suspension wire which acts as a spring between the movable part of the filter (central column + crossbar) and the body of the lower filter (see fig. 6.2 a)). The second one at about 105 Hz is due to the first flexural mode of the blade springs (see fig. 6.2 b)). Hereafter, we will refer to these modes as the *crossbar mode* and the *blade mode*, respectively. The value of the VTF at the frequency of these two peaks is above the unit. This

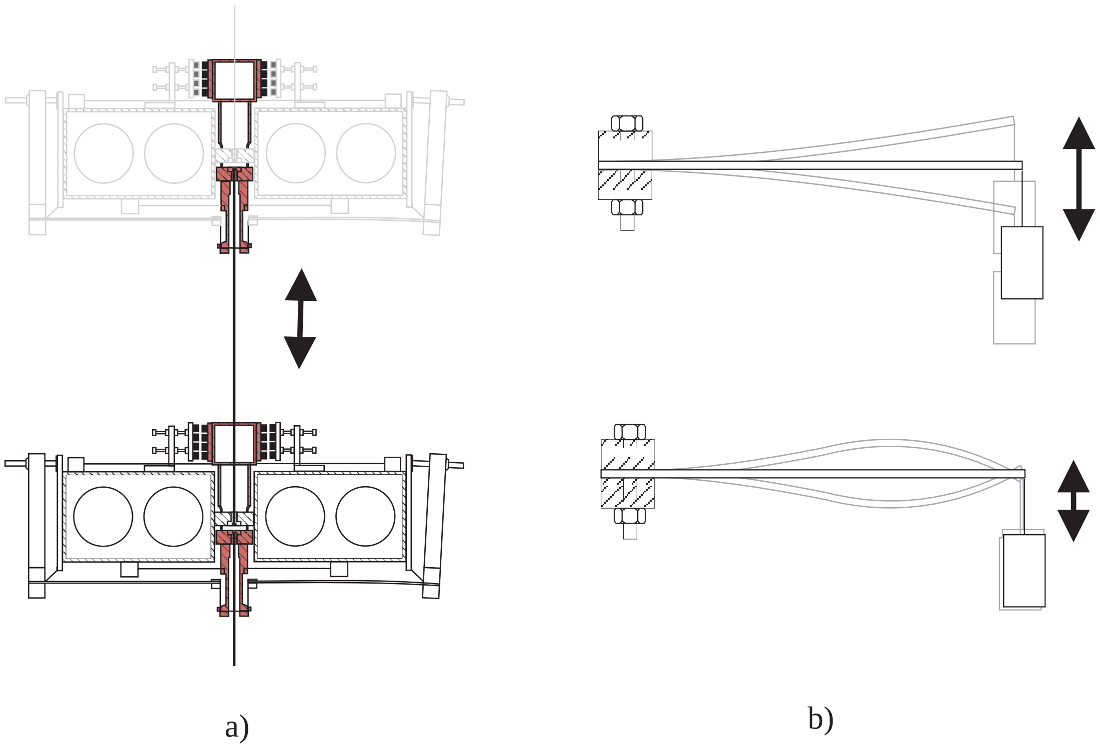

Figure 6.2: *a) The suspension wire acts as a spring between the movable part of the upper filter and the body of the lower one. b) The main mode of the spring blade (upper part) and the first flexural one (lower part).*

means that the filter does not attenuate seismic vibrations at such frequencies. As a consequence, these resonances are channels throughout vibrations are quite entirely transmitted from a stage to the next one.

Another evidence which arises from the measurement shown of fig. 6.1 is the deviation from the $1/f^2$ behaviour of the VTF. Apart from the above mentioned resonances, the vertical attenuation of the filter is damaged by the fact that the blade springs have a not negligible mass and momentum of inertia. This cause a $1/f$ trend which cannot be improved even by damping the internal resonant modes. By the way, we are showing in this chapter that, once damped the the internal modes, the vertical attenuation is enough to keep the seismic noise below the other noises which are expected to limit the sensitivity of the interferometer.

Our dampers are essentially low–Q oscillators coupled with the element whose vibration has to be attenuated. Since a low–Q oscillator dissipates most of energy at

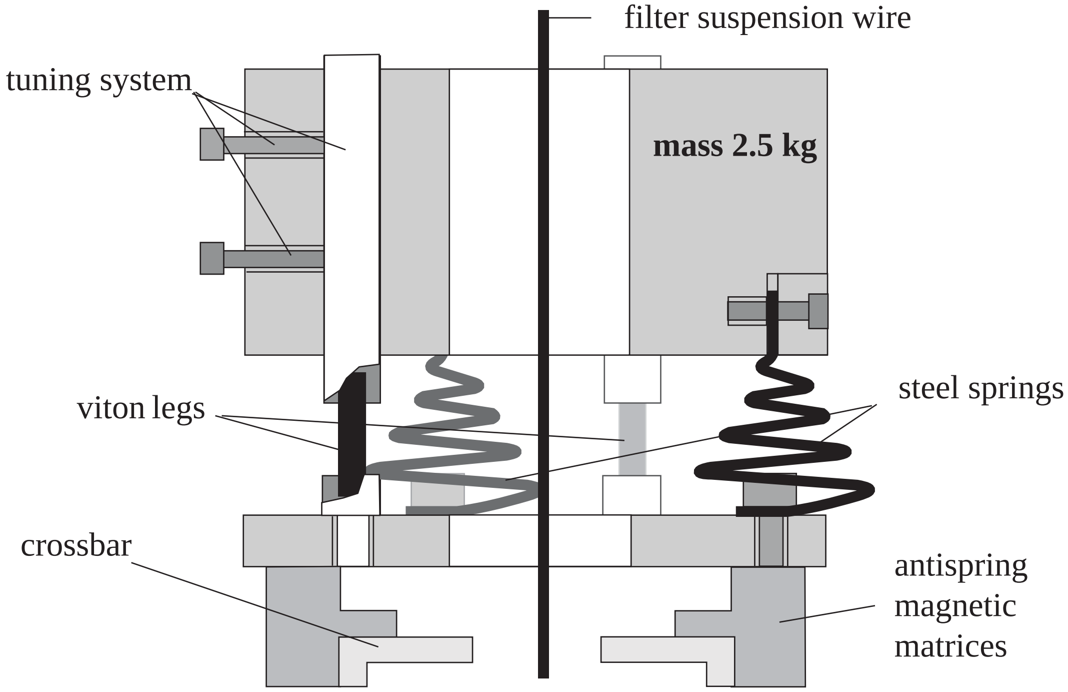

Figure 6.3: *Schematic view of the damper for the crossbar mode.*

its resonant frequency, we have decided to build dampers with adjustable resonant frequency. In this way one can tune the damper at the frequency of the mode which has to be attenuated.

The final version of the damper used to attenuate the crossbar mode is sketched in fig. 6.3. It consists of a mass of 2.5 kg resting on three viton legs which are the dissipating elements of the device. The length of the viton can be varied to adjust the resonant frequency. To avoid stress on the viton legs, three soft steel springs sustain the mass load. This damper is coupled with the vibration mode by fixing it onto the crossbar of the filter. The final version of the crossbar dampers have been designed by the author who has also attended to their realization and to their assembling on all the VIRGO filters.

For the blade mode we use a 50 g weight connected to the center of each blade by means of a viton rod, about 10 cm long (see fig. 6.4 a)). The length of the viton is chosen to match the resonant frequency of the damper to the frequency of the first flexural mode of the blade. In a previous model the viton rod worked in flexural mode and the oscillating mass was lighter than the actual one (see fig. 6.4 b)). We have

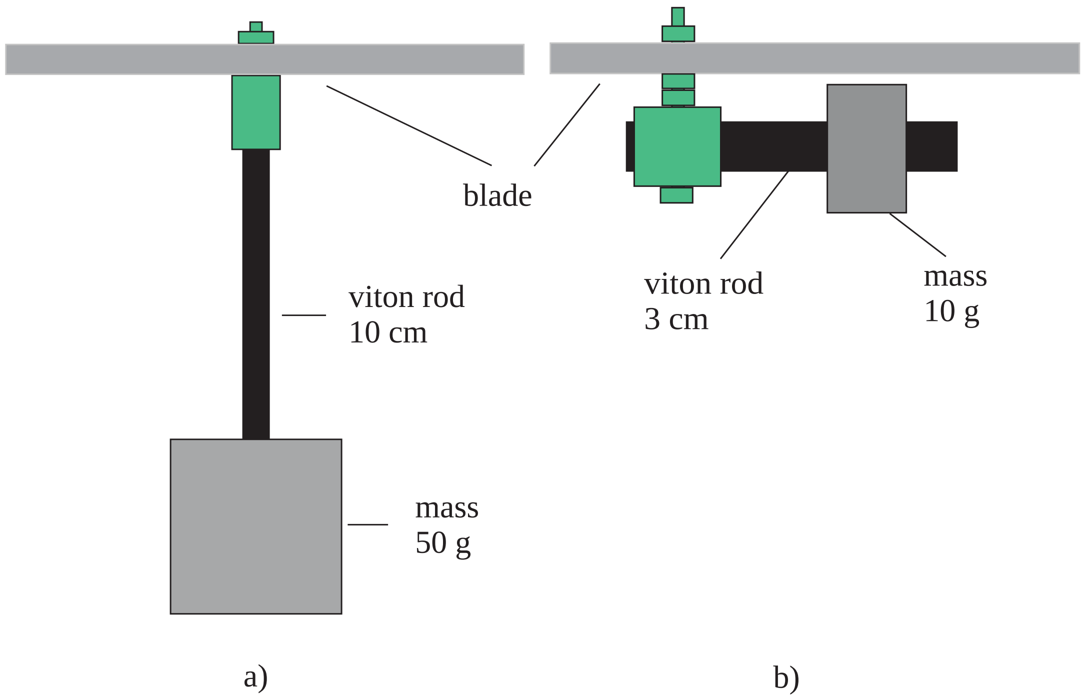

Figure 6.4: *Damper for the blades mode. a) The new version with the viton working in extension mode; b) in the old one the viton worked in flexural mode.*

found that this new design is more efficient than the older one.

6.2 Damper characterization

The first generation of dampers has been tested by the author on a single blade spring and on the prototype mechanical filter already seen in the previous chapter[44, 50]. These tests have confirmed the efficacy in attenuation and the feasibility of damper tuning.

Blade dampers. A detailed characterization of the behaviour of the blade dampers was obtained by studying their effects on the VTF of a single blade taken apart from its filter. Then, the dampers have been mounted on the blades of the prototype filter in order to damp the resonance due to their first flexural mode. In the VTF shown in fig. 6.5 we can distinguish two effects of the blade

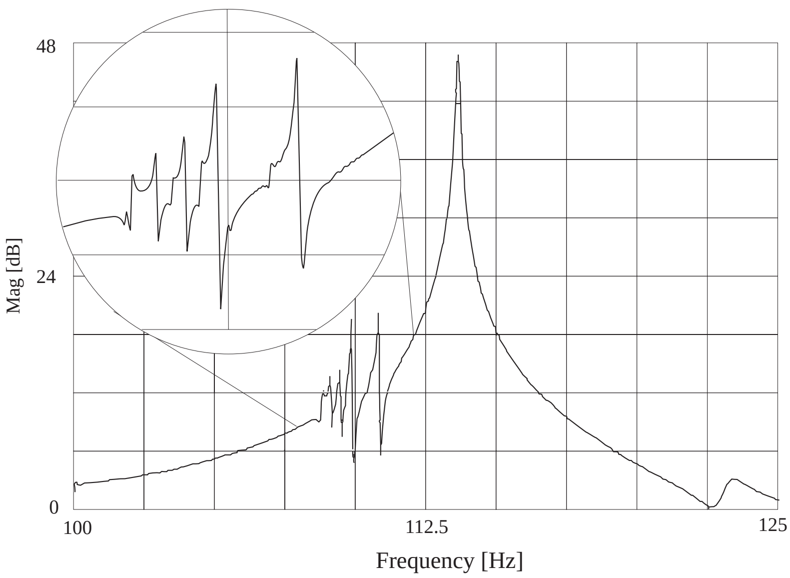

Figure 6.5: *Flexural modes of the 12 blades as they appear in the transfer function measured between the body and the crossbar of the filter prototype. In the circle, the structure attributed to the vibration of the blades as single elements is picked out.*

vibrations: the first is a series of peaks and notches attributed to the blades oscillating as single elements; the second is a sharper peak, at a frequency a little bit higher, identified as a coherent oscillation of all the blades. Since the latter resonance limits the attenuation of the filter more than the single blade contributions, all the dampers are tuned to oscillate at the frequency of that collective mode, i.e. all the dampers have the same arm length. We, of course, cannot directly measure the resonant frequency of the dampers, so we have to change the length of the viton until we get the best attenuation. Once the best tuning is found, the single blade modes result damped as well. A tolerance in the tuning operation of about 1 mm on the length of the oscillating viton rod has also been found.

Crossbar damper. An analogous survey on the crossbar damper has demonstrate the feasibility of damping of the crossbar mode. A 1 mm tolerance has also been estimated in determining the best length of the viton legs.

Dependence on temperature. The mechanical characteristic of viscous–elastic materials are very sensitive to temperature variations. In the previous chapter we

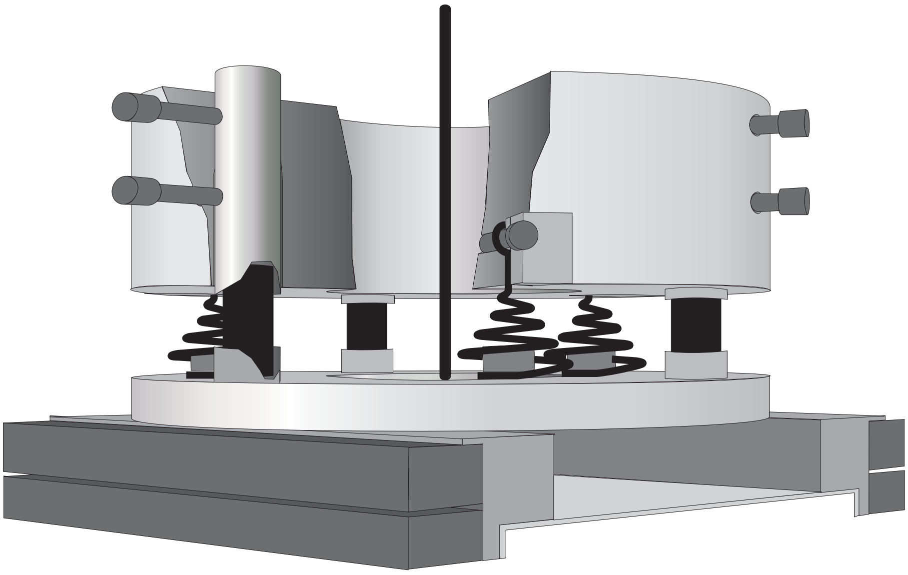

Figure 6.6: *Perspective view of the crossbar damper.*

have seen that the superattenuators have to work at a stabilized temperature but, at the time this survey was done, the working temperature had not been well defined yet. If the working temperature had been too high (or too low) to carry out the assembling operations we would have had to be able to foresee the change in the dampers performances due to the different temperatures. The measurements at different temperatures of the efficacy of the dampers allow us to determine an empirical relationship for the correction to apply to the active length of the viton rods in case the temperature of the assembling operation is different from the working temperature of the superattenuators. In the range of temperatures between 22 and 35 °C, we have found:

$$\frac{\Delta L}{\Delta T} \cong -0.1 \frac{\mathrm{mm}}{^{\circ}\mathrm{C}} \tag{6.1}$$

for the blade dampers and

$$\frac{\Delta L}{\Delta T} \cong -0.05 \frac{\mathrm{mm}}{^{\circ}\mathrm{C}} \tag{6.2}$$

for the crossbar damper.

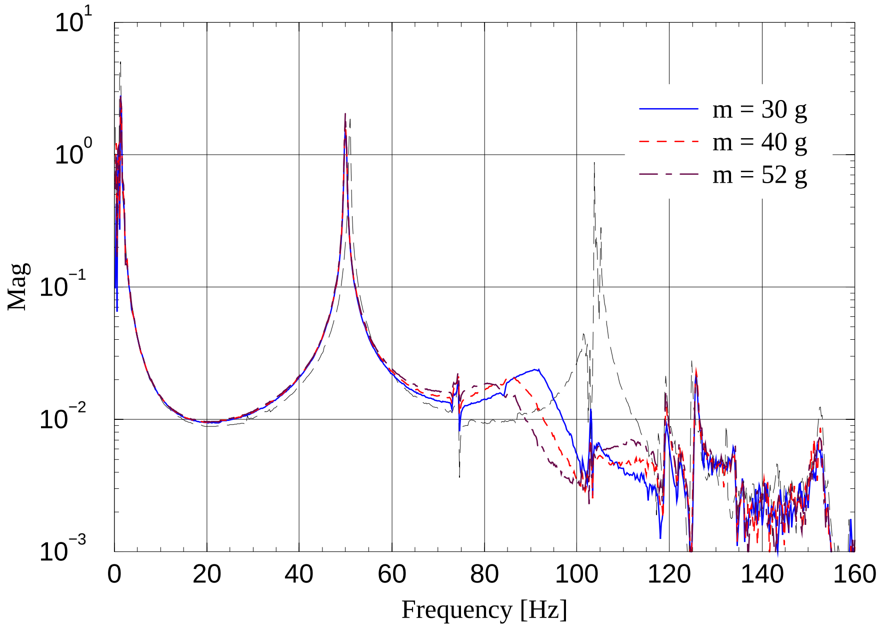

Figure 6.7: *Vertical transfer function modules of the filter 3 for three different values of the oscillating mass of the blade dampers. The VTF of the filter without dampers is also shown (long dashed line).*

6.3 Superattenuator prototype

Before starting to install the superattenuators of the VIRGO interferometer, a complete superattenuator prototype has been assembled in the laboratory of INFN–Pisa. The prototype differs from the final superattenuator only for its height because of the lower distance between the filter 1 and the top stage due to practical limitations.

A new series of measurements has been done to test the efficacy of the dampers on the filters mounted along the prototype chain. The most important parameters studied are the length of viton and the weight of the oscillating masses. The final version of dampers has been chosen after studying different alternatives (in particular for the blade dampers).

The fig. 6.7 shows how the VTF of a filter changes when the oscillating mass of the blade dampers increases from 40 g to 52 g: the height of the residual peak decrease but its frequency moves towards lower values, where the tail of the crossbar mode rises the VTF. We have found that 50 g is a good compromise. Moreover, the blade modes of each filter are all quite close to the same frequency so we can mount

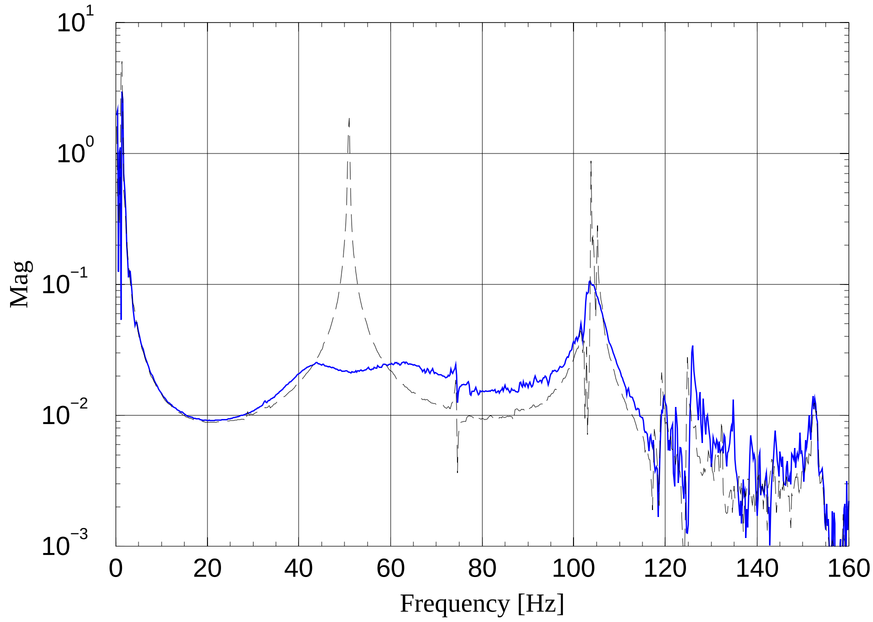

Figure 6.8: *VTF module of the filter 3 with the crossbar damper (solid line) compared with the undamped one (dashed line). The blades are also damped but using the old devices.*

the blade dampers all with the same resonant frequency, that is with the same viton length.

In the VTF shown in fig. 6.8 we can see the effect of the crossbar damper; the dotted line is the filter VTF without dampers; here we have damped also the blades but with the old dampers which are less efficient. Using the new blade dampers, as we can see in fig. 6.9, the peaks of the blades completely disappear. At the time the measurement was done this filter was the last mounted on the chain and was charged with a 400 kg dummy load. In this condition, the VTF differs for about a factor 2 from that we would have measured if it had been loaded with the lower stages of the superattenuator chain.

The frequency of the crossbar mode differs from a filter to another because of the different masses involved and of the different suspension wire diameters. Therefore, each damper has to be tuned at the specific frequency of the filter it will be mounted on. A calibration curve of the device can be obtained by fitting the measured frequencies f versus lengths of the viton legs L with the relationship we get from the

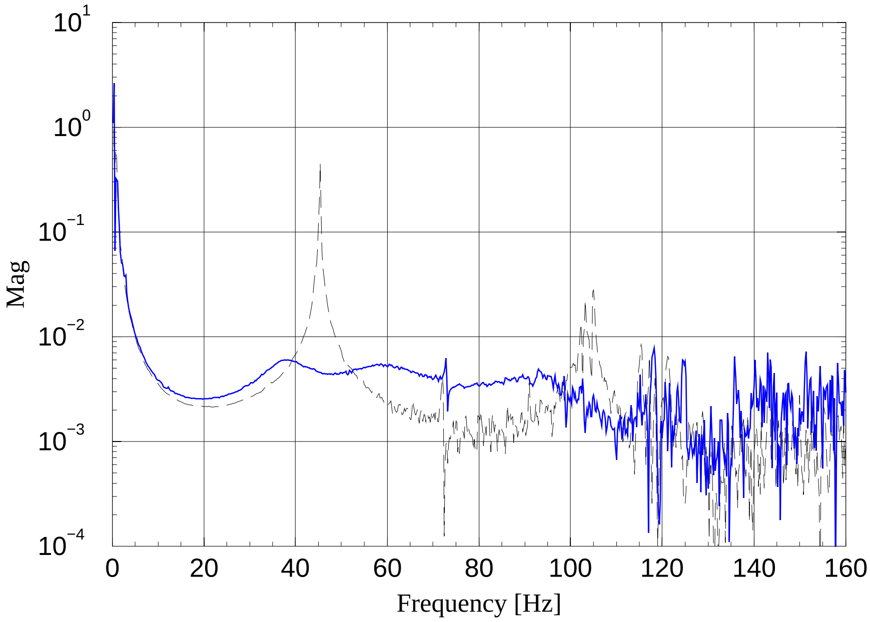

Figure 6.9: *VTF module of filter 4 full damped (solid line) compared with the undamped one (dashed line).*

elastic elongation law of materials:

$$f = \frac{1}{2\pi}\sqrt{3 \cdot \frac{ES}{LM}}, \tag{6.3}$$

where E is the Young modulus of the material, S is the section of the viton legs and M is the mass of the damper (see fig. 6.10).

6.4 Superattenuator transfer function

In section 2.5 we defined the transfer function of an unidimensional oscillator. For a linear mechanical system with six degrees of freedom, the transfer function is defined as the linear operator connecting the Fourier transform of the input point displacement to the Fourier transform of the output point displacement in all the six degrees of freedom. Above a few Hz, the attenuation of our superattenuator is so strong that it is not possible to perform a direct measurement of the 36 frequency–dependent elements of the matrix: no commercial accelerometer is sensitive enough to detect the small mirror residual displacement.

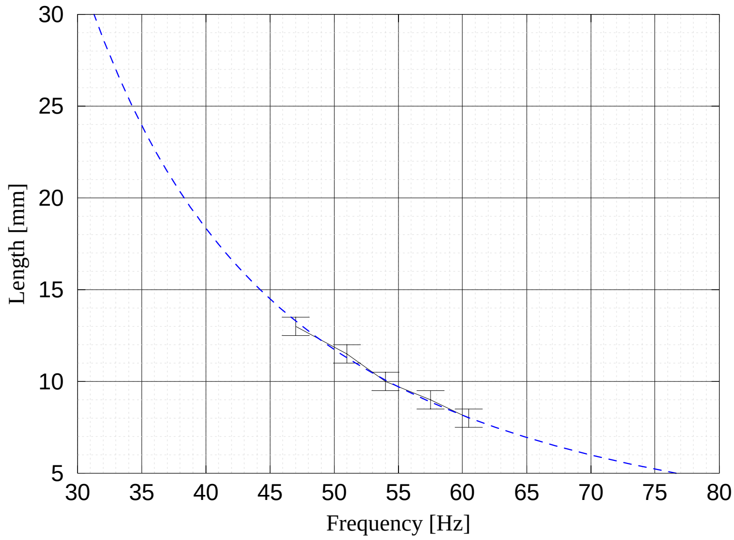

Figure 6.10: *Calibration curve of the crossbar damper with a 2.78 kg oscillating mass (the mass of the accelerometer is also included).*

An alternative strategy to measure the total transfer function can be adopted if we think that our system interacts with the external environment only through the input point. For such a system it is possible to write:

$$X_{in} = T_{in} \cdot F_{in} \qquad \text{and} \qquad X_{out} = T_{out} \cdot F_{in}, \tag{6.4}$$

where the operators T_{in} and T_{out} do not depend on the force F_{in} applied to the input point, since the system is linear. In particular, if X_i and X_{i+1} are the input and the output point of the i–th stage of the chain, respectively, we will have:

$$X_{i+1} = T_{i+1}T_i^{-1} \cdot X_i. \tag{6.5}$$

The transfer function in the right hand term of the latter equation does not depend on the elements and on the external forces which are upstream of the input point X_i. It can be directly evaluated by exciting the stage of the chain and by measuring the displacements of the input and output points with commercial accelerometers which are sensitive enough to detect the output signal after one stage of attenuation.

Now we can rewrite the (6.5) for the input and the output points of the entire chain of n stages inserting $n-1$ identity operators, so obtaining:

$$X_{out} = T_{out}T_n^{-1} \cdot T_nT_{n-1}^{-1} \cdot ... \cdot T_1T_{in}^{-1} \cdot X_{in}. \tag{6.6}$$

Therefore, the total transfer function of the entire superattenuator chain can be obtained by multiplying the single stage transfer functions of equation (6.5) directly measured on each stage.

In principle a total number of 12 accelerometers connected to a spectrum analyzer with the same number of channels would be necessary to evaluate each matrix element of the transfer function. In addition a very delicate analysis should be performed to distinguish each matrix element from the others because of instrumental couplings in the accelerometers. However, in the vertical direction each filter, as well as the entire superattenuator, has a weak coupling with the other degrees of freedom. This means that the 6×6 matrix is quasi–diagonal along the vertical direction. Two accelerometers, one on each filter, monitoring the vertical displacement, are sufficient to determine the diagonal element of the transfer function of a single stage. Moreover, the diagonal term of the total VTF is well represented with the product of the single diagonal terms. The error induced by small couplings has been estimated to be a few percent.

The VTF of the prototype chain has been evaluated by multiplying the VTFs of each single stage measured on the chain[51]. In the total VTF shown in fig. 6.11 we can see how the crossbar mode peaks are suppressed by dampers except that of filter 0, at about 35 Hz, and that of filter 7, at about 50 Hz (indeed these two filters do not have the crossbar damper). All the blades are also well damped.

The transfer function measurements has been performed along the horizontal axis too. Since our system exhibits a rough cylindrical symmetry, the total transfer function measured along a fixed horizontal axis is very similar to the one measured along any other horizontal axis. In this case the main trouble is due to the coupling of translations along the horizontal axis with the rotations around the horizontal axis (tilt) perpendicular to the first one. This can be explained by the presence of the suspension wire. A tilt of the upper filter induces a bend in the lower filter suspension wire which makes the lower filter translate. The presence of this coupling implies the transfer function matrix is not diagonal along the horizontal axes. Therefore, it is not possible to evaluate the entire superattenuator horizontal transfer function by simply multiplying the diagonal terms of each single stage matrix. This method only gives a rough estimation of the total horizontal transfer function, though its order of magnitude is correct.

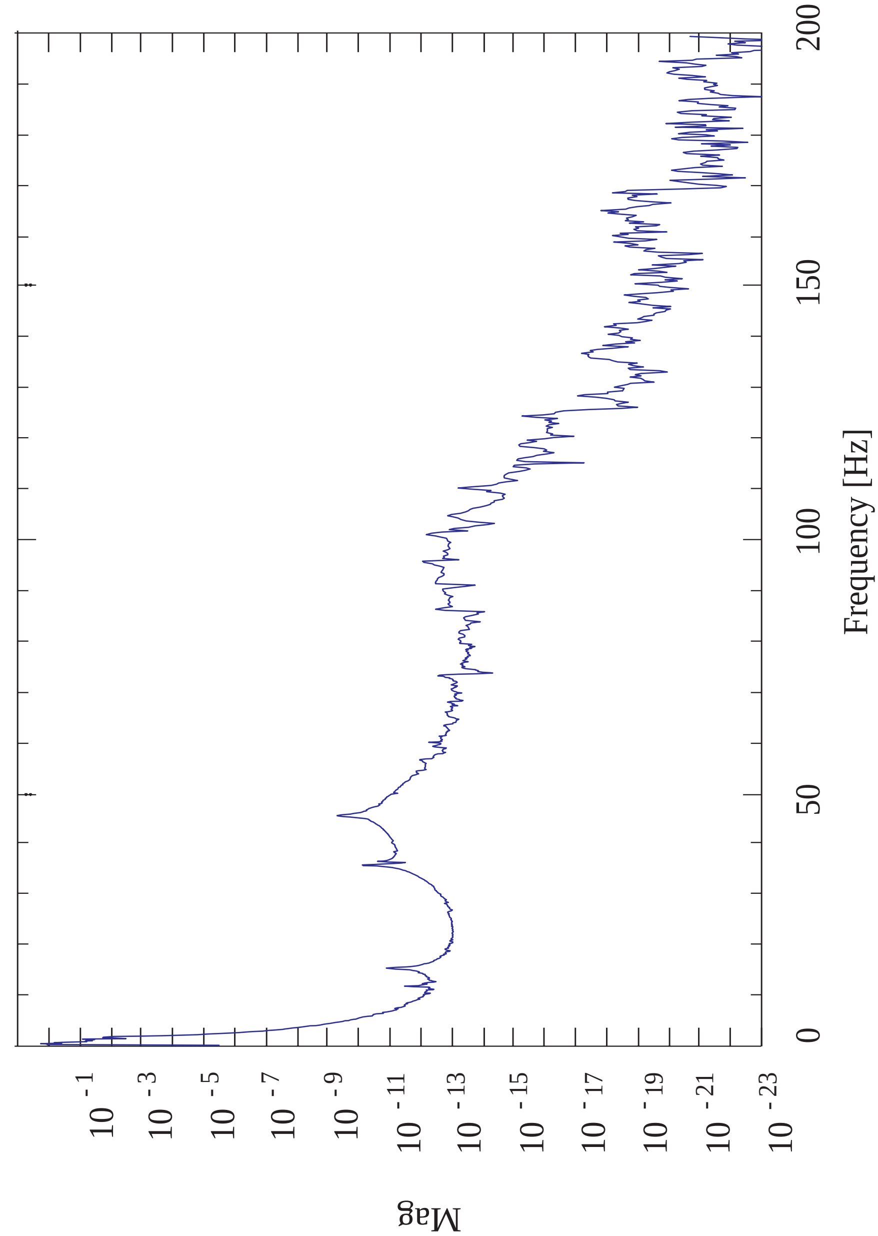

Figure 6.11: *Vertical transfer function module of the superattenuator chain. The function is obtained by multiplying the VTFs of each filter measured on the chain.*

On the other hand, the comparison between the module of the horizontal transfer function between two filters and the module of the vertical one shows that, above 10 Hz (resonant peaks excluded), the attenuation of each stage in the horizontal direction is at least ten times better than the vertical attenuation. So, we can conclude that the total horizontal transfer function is order of magnitude smaller than the vertical one. In other words, the main seismic noise contribution in the VIRGO detection band comes from the residual seismic vertical component coupled to the beam direction.

The measurement of the total vertical transfer function has demonstrate that the superattenuator chain is able to isolate the optical components of the VIRGO interferometer from seismic noise starting from a few Hz. Indeed, we have estimated an attenuation factor ranging between 10^9 and 10^{13}, in the frequency band from 4 to 200 Hz, for the seismic noise vertical component which represents the most important contribution to the noise. With this attenuation the residual seismic noise, in the above mentioned range of frequency, is negligible with respect to other noises limiting the antenna sensitivity.

Chapter 7

Steel blade springs for the VIRGO superattenuators

Static and dynamic stress affects the microscopic structure of the materials and can change their macroscopic features. The mechanical filters are made up of different elements which will be subject to stress, mainly static, for long time. Blades, wires, hinges and clamps might suffer such deformations to induce a sag of the load of the filter and, as a consequence, of the suspended mirror.

The phenomenon we refer to is known as *micro–creep* or simply *creep*. It is mainly due to single microscopic yielding events at the crystalline structure level.

The creep is the source of two problems. The first is that a sag of a few microns per day would require monthly reset of the filters working point and would saturate the dynamic of any vertical positioning system of the chain in a few years. The second is the noise induced by each single creep event.

A survey on a filter prototype had picked out the entity of these problems towards the material for the realization of the blade springs and further researches were done on special alloys which would have a lower creep. The solution has been indicated in the *Maraging* steel and all the most stressed components of the superattenuator are made of this material. The blades have undergone the special treatments we are describing in this chapter.

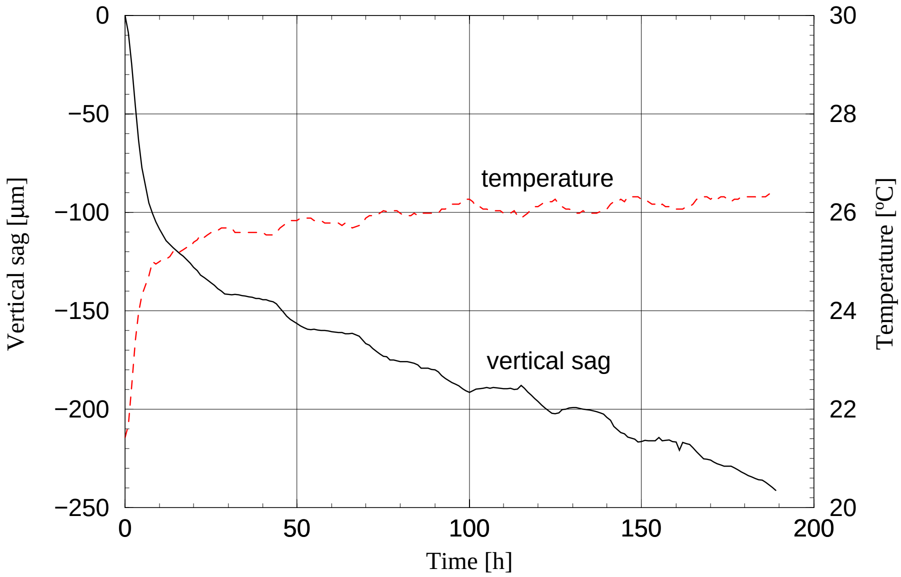

Figure 7.1: *Vertical displacement of the load of the filter and temperature versus time. It can be observed the vertical sag due to creep when the temperature is almost constant around 26 °C.*

7.1 Evidence of creep

By means of the experimental set–up described in section 5.2 the author carried out a survey on the vertical lowering of the movable part of the filter prototype[55]. The bare filter, without the antispring system, was loaded and the position of its crossbar with respect to the filter body was observed through an LVDT sensor. We made a series of measurement at different stabilized temperatures, each of them few weeks long, in order to evaluate the speed of the filter sag as a function of the operating temperature.

The fig. 7.1 shows the vertical displacement of the crossbar versus time in the measurement taken at 26 °C. The recording of data started when the temperature was at about 21 °C so we can see also the warming up phase of the system. The values of the temperature are shown as well. It is possible to distinguish two different trends. During the warming up the effects of the temperature variation prevail. As the temperature increases the blades become softer and they need a larger flexion to hold the weight of the applied load. These flexions are substantially elastic and reversible. When the temperature is stabilized around 26 °C, unless a maximum daily

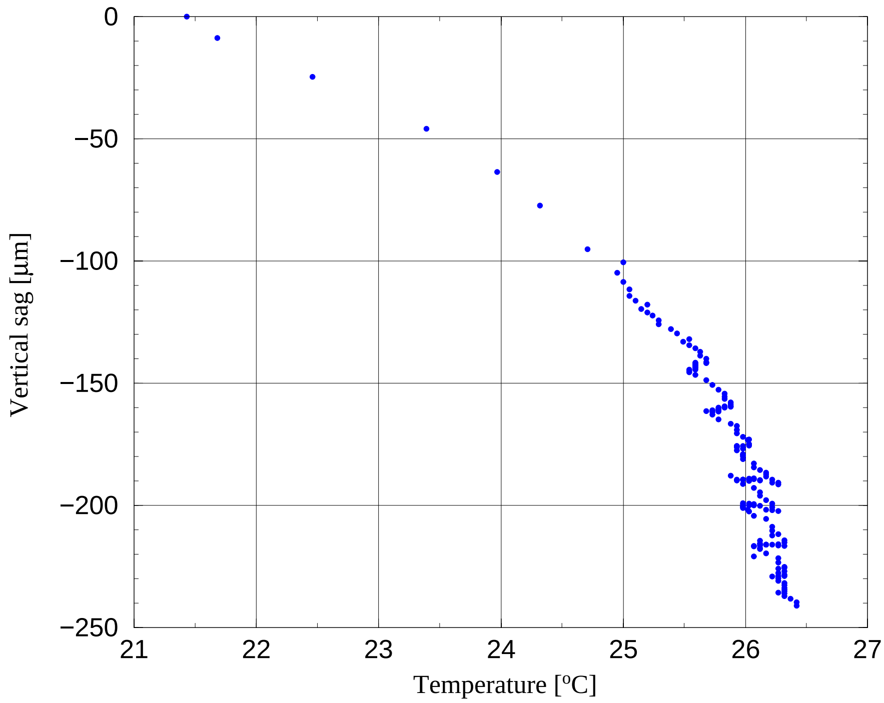

Figure 7.2: *Vertical displacement of the load of the filter versus temperature. In the region around 26 °C we can distinguish the daily excursion of the temperature and the progressive sag due to creep. The time flows from left to right.*

excursion of about 0.4 °C and a slow increment of its average value, the slope of the displacement curve does not agree with the temperature increment any more. This is the creep.

The effect is still more evident if we consider the lowering of the crossbar as a function of temperature (see fig. 7.2). From the linear trend concerning the warming up phase we have been able to deduce the change of the crossbar position due to the temperature variation. A value of -30 μm/°C has been found. If this value is attributed to the only variation of the stiffness of the blade springs k_s, for this one we obtain:

$$\frac{1}{\Delta T}\frac{\Delta k_s}{k_s} \approx \frac{1}{\Delta T}\frac{\Delta y_0}{y_0} = \frac{2.1 \times 10^{-4}}{^\circ\mathrm{C}}, \tag{7.1}$$

where y_0 is the rest position of the tip of the blade (see fig. 4.7).

The curves shown in fig. 7.3 refer to the sag of the crossbar with respect to the filter body measured at various temperatures after these had stabilized. The speed

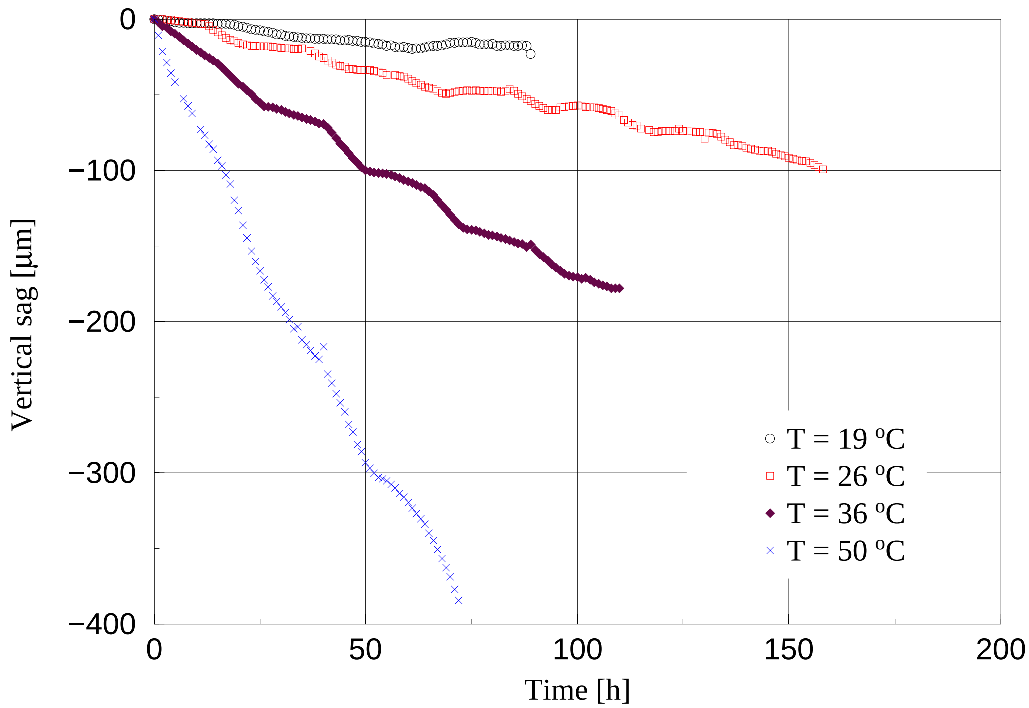

Figure 7.3: *Vertical sag of the filter load versus time at different temperatures. The speed of sag increases as temperature increases.*

of sag increases with the temperature. We have guessed a time dependence of the position $y(t)$ like:

$$y(t) = \lambda T(t) + Kt, \tag{7.2}$$

where $T(t)$ is the temperature as a function of the time and K is the speed of sag due to the creep. By assuming, for the coefficient of thermal elongation λ, the value of $-30\ \mu\text{m}/°\text{C}$ previously determined and by subtracting from the measured data y_i the contribution $\lambda \cdot T_i$, we have isolated the component due to the creep and have estimated a value of K. For each measurement we have assumed that K was quite constant in the small spread of temperature observed. The estimated values of the speed of sag are plotted versus the temperature of the respective measurement in fig. 7.4, in which it is evident an exponential behaviour (see next section).

The sag observed in the above described measurements has to be entirely ascribed to the creep of the blades, being these the most stressed components of the mechanical filter. To confirm this claim, a further test aiming to rule out the creep of the filter

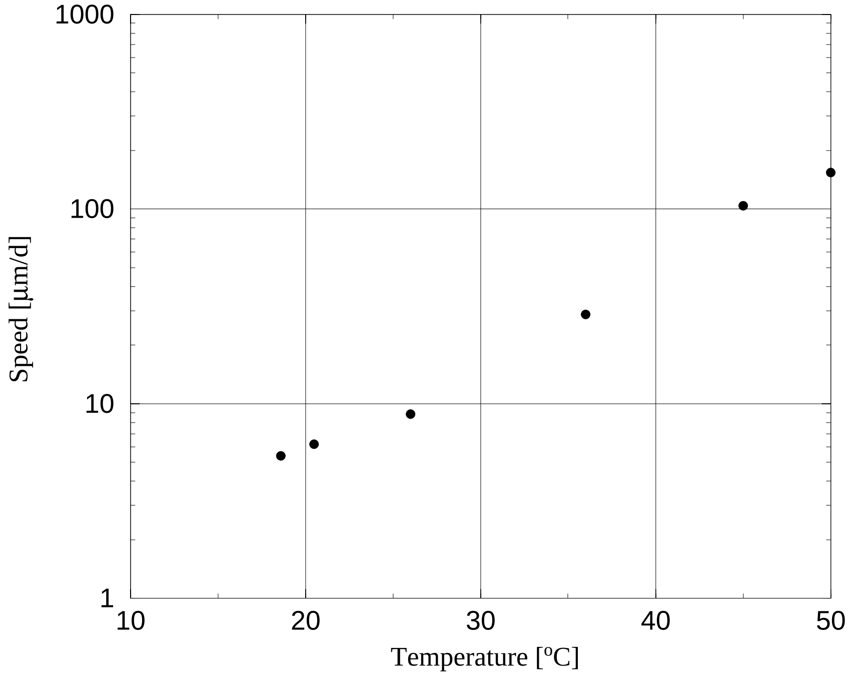

Figure 7.4: *Mean speed of sag of the movable part of the filter versus temperature. The exponential trend is evident.*

body and of the blade hinges was made. We clamped eight very strong and rigid blades, 4 cm thick, to a filter which was then loaded with a 1.2 ton mass (about twice the nominal load of the filter). The system was placed in a temperature controlled chamber, at about 35 °C, and the sag of the load was measured by means of a mechanical comparator placed between the crossbar and the filter body. Despite the double acting load, no lowering of the blades tips, larger than the instrument sensitivity (about 1 micron), was found in two weeks of observation. The wires were also tested in similar condition with null results over two weeks.

The results of the measurements of the blade sag were rather alarming. The measured creep effect of 10–20 micron per day around the most likely VIRGO operating temperature (at that time not yet defined) was much higher than the expected one and a strong dependence on temperature was evident. No reduction of creep had been observed on the time scale of weeks. In few days the filter sag would lead the antispring matrices out of the right working range and a reset procedure would be necessary. This level of creep, absolutely unexpected, could not be tolerated by our apparatus because it would saturate the dynamics of any feedback system of the vertical positioning in a few month.

Moreover, as shown in the section below, creep is responsible of a sort of mechanical shot noise which affects the suspended mirrors. The level of creep resulting from our measurements would induce mirror displacements, in the beam direction, order of magnitude larger than the expected displacement due to gravitational waves. The maximum tolerable creep is set by the requirement to keep the noise induced well below the thermal noise limit.

7.2 The creep phenomenon

The sag of the blades tips is the macroscopic evidence, easy to be measured, of microscopic processes which happen at the level of the crystalline structure of the material the blades are made of. To understand what happens it is necessary to glance into the microscopic structure of metals. Here we will report a simplified description of the topic, deferring the reader to specialized publications for a better treatment[52, 53, 54].

7.2.1 Creep origin

As soon as the stress is applied to a polycrystalline solid, a quasi–equilibrium state is reached where each grain is deformed along the local stress direction. Inside each grain the stress is initially distributed rather uniformly throughout its volume. As time goes on, thermal fluctuations shake free or generate *dislocations*: lines of defects of the crystalline structure. This dislocations glide through the grain pushed by the stress field pressure until they reach the surface of the grain or a pinning point and there they accumulate. In this way they actually transport a part of the stress originally distributed in all the grain volume, towards its boundary. If the built up stress is enough to exceed the yield limit a grain slippage will occur and the energy is released and distributed between the other grains. The energy released in a single grain slippage is estimated to be of the order of hundreds of picoJoule, taking into account the dimension of the grains and the applied stress.

The speed of sag of the applied load is proportional to the average elongation due to the single creep events and to the frequency at which they occur. The frequency depends on the number of dislocations which can reach the grain surface and therefore, it depends on temperature. The amount of dislocations inside a grain depends on chemistry and physical processes the material has been undergone to. A fraction of these dislocations proportional to an exponential of the applied stress has activation energy comparable to the thermal energy $K_B T$ (i.e. the Boltzmann constant times the absolute temperature) and it can move inducing creep in the long run. Although very small (10^{-21} J at room temperature), thermal fluctuations are able to drive such an event in which energy enormously higher are involved.

The frequency f at which the dislocation are used up is given by:

$$f = f_0 \cdot e^{-\frac{E}{K_B T}}, \tag{7.3}$$

where both the activation energy of the elementary creep process E (of the order of eV) and the constant f_0 depend on the detailed crystalline structure and on the applied stress. E is not a fixed value because in the crystals there is an infinity of slightly different kinds of dislocations, each with its own activation energy. The observable E is rather the mean value of a distribution of activation energies.

Above a certain stress threshold the thermal energy fluctuations can shake free only a limited number of available dislocations. In this regime, as time goes on, the dislocations are progressively used up until they are exhausted. If the equation (7.3) is applied to different kinds of dislocations, it is obvious that the ones with lower activation energies will be used up faster. In absence of dislocation regeneration, E grows with time because of the longer lifetime of the dislocations with higher activation energies. As a consequence, the creep shows a logarithmic trend with time while the speed of sag decreases as the inverse of time. Moreover it is possible to eliminate all the dislocations which can be activate by aging the loaded sample at a higher temperature. This regime is named α–creep.

Above the threshold level, the distributed stress is capable to continuously generate new dislocations. In this case the creep will induce a sag with constant speed and we can speak of steady–state creep or β–creep. The tested blades were made of AISI 1070 steel and we have found them to be in the β–creep regime.

7.2.2 Creep noise

The main warning coming from the unexpected amount of creep concerns the noise caused by the grain slippages. Each of them generates a quasi instantaneous pulse which propagates throughout the materials at the speed of sound. A simple theoretical model of a mirror suspension wire has been proposed to evaluate the noise induced by the creep events[59]. The linear spectral density $\tilde{y}(\Omega)$ of the vertical displacement of the mirror due to grain slippages results to be:

$$\tilde{y}(\Omega) = \frac{\omega_0^2}{\sqrt{\left(\Omega^2 - \omega_0^2\right)^2 + \gamma^2\Omega^2}} \frac{q_s\sqrt{\lambda}}{\Omega}, \tag{7.4}$$

where ω_0 is the vertical resonant frequency of the wire, γ is its dissipation factor, q_s and λ are the amplitude of a single slippage and the frequency they occur, respectively. We can evaluate λ from experimental results on the speed of sag K like that ones described in the previous section, being this two quantities bound by the simple relation $K = q_s \cdot \lambda$. The amplitude q_s is deducible from the above stated theory and it results to be of the order of picometers.

From the experimental data it arose that the level of creep noise would be extremely high at the operating temperature foreseen for VIRGO (around room temperature). The measured values of about 10 microns per day corresponds to hundreds of "clicks" per second. The vibrations induced on the mirrors in the beam direction were orders of magnitude higher than the displacement expected from the impinging gravitational waves (typically 10^{-18} m) . Such vibrations could not be entirely attenuated since they were generated all along the superattenuator chain. Some rough conservative evaluations provided a strong limit to the maximum creep rate tolerable in the last stage of the suspension: about 10^{-2} step/s which corresponds to a speed of sag of about 1 nm per day. Particular attention had to be paid to the suspension wires of the mirrors whose creep directly affects the mirrors themselves. A survey on the creep in the mirror suspension wires has been carried out in the laboratories of the INFN–Perugia[59].

7.3 The Maraging solution

The high β–creep level we measured in the survey described in section 7.1 has to be attributed to the pretty uniformity of the iron grains contained in high carbon steel alloys like the AISI 1070 of the tested blades as well as the AISI 1085 of the suspension wires. The dislocations (and the stress they carry), driven by the stress field, migrate throughout the grains and accumulate either into defects or into the small carbon crystals at the boundary of the grains. As the dislocations can be collected from the entire volume of the grain to relatively small pinning points, the yield stress will be eventually reached even for low applied loads.

To reach the desirable α–creep regime, the AISI 1070 would be loaded with less than 15–20% of the commonly accepted elastic limit. However, the VIRGO requirements of low frequency oscillations involve high stress applied to the blade springs. Indeed, it can be easily shown that the resonant frequency of the blades depends on the inverse square root of the applied stress.

After evaluating different alternatives, we found a solution to the creep problem in a completely different kind of steels: the precipitation hardened steel alloys. In particular our choice was an alloy of the Maraging steel family: the Marval 18 C–250[1][56, 57].

In Maraging steels only about two thirds of the alloy is iron, the balance is made of nickel, chromium, cobalt, molybdenum and titanium in finely weighted percentage. The alloy presents iron grains of the same dimensions of normal steel (5–10 μm) but they are populated by many millions of nanometer sized metal crystal which have "precipitated" into the grains during the hardening process. In such a structure, dislocations are not allowed to travel throughout the grain since they are stopped by the nanocrystals. Therefore, the stress remains frozen within the grain volume and the slippage threshold on its surface cannot be reached anymore.

We studied the behavior of the Maraging steel blades through a series of measurements aiming to determine the amount of creep by monitoring the sag of the load under different applied stresses, at different operating temperatures and after different thermal treatments of the samples: the results were more than comfortable[57]: no evidence of steady–state creep was found under a large range of test conditions.

[1]Marval 18 is a trademark of Aubert & Duval SA, 41, Rue de Viliers, Neuille–sur–Seine, F–92202, France

A similar survey was performed on the filter suspension wires[58].

Being the maximum tolerable creep rate beyond our measurement capabilities, we could only indirectly estimate it. Indeed, the measurements at different temperatures demonstrated that the creep rate, indistinguishable from zero at a certain temperature, could be deduced from the measurement at a higher temperature by scaling the latter by a factor depending only on the difference of temperature. Since a factor of reduction of three orders of magnitude was evaluated to be induced by a reduction of temperature from 80 °C to 30 °C, a creep rate of less than one micron per day at 80 °C would correspond to less than one nanometer per day at VIRGO operating temperature (a value acceptable for VIRGO) . All the tested blades and wires made of Maraging steel were observed to reach this level of creep within the duration of the measurements (about two weeks).

From this survey, we found that the available dislocation consumption was accelerated, so lowering the creep rate, by increasing the operating temperature . In fact, after baking the loaded blades, the creep rate at room temperature was practically indistinguishable from zero in our experimental set–up.

Moreover, a technique to suddenly reduce the number of available dislocations, as effective as the baking, is to “train” the blades at more than their nominal load. A series of measurements aimed to monitor the *acoustic emission* activity while the blades are loaded, has confirmed the above statement[60].

Acoustic emission is a typical event detectable in metals during deformation. In the case of loaded metallic samples, dislocation motion is one of the main sources of detectable (ultrasonic) acoustic signals. The several set of events collected gets evidence of a memory effect that influence the motion of dislocations in the Maraging steel, known as Kaiser effect (see [60] and references therein). When a sample is firstly loaded, then unloaded and finally reloaded in the same direction, the rate of acoustic emission events is considerably reduced during the second loading cycle. A reduction of the ultrasonic processes, corresponding to a reduction of the available dislocations, is hence obtained by applying a few stress cycles to the steel blades improving, at the same time, its stability on the microscopic scale.

7.4 Heat treatments and tests

In order to satisfy the mechanical specification of the VIRGO detector, a complete characterization of Maraging steel has been done to optimize the mechanical properties of the special elements we were going to build[61, 62]. Both the composition of Marval 18 C–250 and its microstructure concur to reduce the microplasticity and microcreep phenomena. The microstructure is strengthened by the aging treatment which causes the precipitation of intermetallic particles, reducing the motion of dislocations. Therefore, a strong increment of strength of the material is reachable with an adequate thermal treatment, as well as an improvement of its hardness and yield point. We have determined that the best heat treatments to optimize the mechanical properties of the Maraging steel is the following:

Material solution annealing. The elements made of Maraging steel are heated at 1113 °K (840 °C) for 1 h. At this temperature the material undergoes a complete transition to the austenitic phase and the hardening elements (molybdenium, nickel, cobalt and titanium) are in solution with other elements. During the cooling phase in air, a massive martensitic formation with a high concentration of lathe is generated. The dimensions of the lathes and the density of the dislocations will determine the hardness of the material.

Aging process. The pieces are heated at 708 °K (435 °C) for 100 h. The aging treatment causes the precipitation of an inter–metallic formation of thin particles which bring about a reduction in motion of the dislocations. The maximum ultimate tensile strength is attained with a suitable combination of aging time and furnace temperature. It has been found that, with this combination, the dimension of the precipitates were more effective in locking the dislocations and reducing the microplasticity phenomena.

For the best control of the final results, we decided to perform the aging process of all the elements in Maraging steel for the VIRGO superattenuator construction by ourselves. A suitable oven has been placed in the laboratory of INFN–Pisa for this purpose and it has been equipped with a programmable temperature controller. A small pipe connected to a set of gas–cylinders allows us to flux Argon into the oven in order to get a poor oxygen atmosphere during the heat treatments.

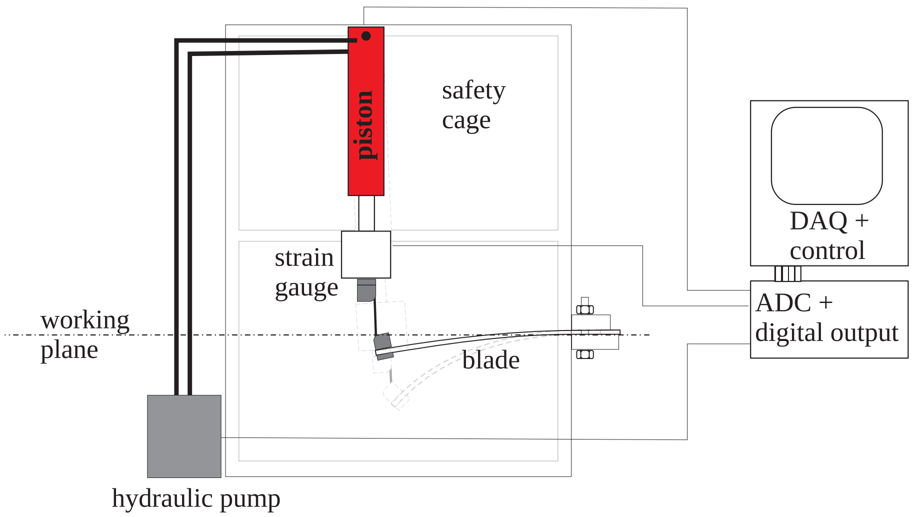

Figure 7.5: *The apparatus to test the VIRGO blade springs.*

The about 400 blade springs have undergone the following described special procedure, identified and performed by the author. Since the blades are bent to the required curvature radius, according to their nominal load (see section 4.1.2), before the hardening of the steel (otherwise it would be impossible to bend them) we first perform a solution annealing (1 h @ 840 °C) to eliminate residual stresses due to bending operations. After they are made cool down to room temperature, in air, they are sent again to the bending in order to bring in correction to the curvature radius, in case the heat treatment has caused small deformations. Then the blades undergo the aging process (100 h @ 435 °C) at the end of which, they are quickly cooled in water and ice.

7.4.1 Fatigue test

Once the heat treatment has been concluded, we submit each blade to a *fatigue test*, a typical technique to take the materials to their optimal performances. Moreover, as discussed in the previous section, fatigue test allows to eliminate the available dislocations so to reduce the creep noise effects. The fatigue test we have decided to adopt, consists of 10 cycles of load–unload the blade. A special testing machine has been built to load the blades by means of a hydraulic piston (see fig. 7.5).

The base of the blade is clamped to the lateral beam of a rigid frame and its tip is connected to the piston through a steel wire. The base of the piston is fixed to the top of the frame so that it works perpendicularly to the blade when the latter one assumes its working flat configuration. The load is applied upwards. In each cycle the piston pulls the tip of the blade from -45 mm to +45 mm with respect to the working position of the blade, then it returns back. Each round trip takes about 40 seconds. In this way we apply to the blade a load which slowly increases up to about 30% more than the nominal one. We have estimated that this level of the applied stress is sufficient to eliminate all the dislocations available at the nominal load (see previous section) and, at the same time, it is far enough from the yield point.

During the tests, the position of the tip of the blade is read by a built–in position sensor measuring the elongation of the piston. A strain–gauge cell placed between the head of the piston and the tip of the blade measures the applied load. Both sensor and piston operation are digitally controlled by a customized LABVIEW data acquisition program running on a PC. A National Instruments ADC board and a home made readout device are the interface between the PC and the testing machine. The above described apparatus is part of a larger set up realized to test other components of the VIRGO superattenuator[63]. Moreover, the blades testing machine has been used for the acoustic emission measurements described in the previous section.

7.4.2 Characterization

Since first measurements we have found that the blades hardly ever assume a perfectly flat shape when they are loaded to their nominal load. The reason of this is probably in their processing: the blades birth flat, then they are bent nearly by hand and slight deviations from a uniform curvature are likely to exist. These defects turn out into a deviation from the flat shape the blade would assume if it had a uniform curvature. As a consequence, when the nominal load is applied to the blade, its tip will get a position, with respect to the filter body, different from the expected one. It is important to notice that the position of the tip of the blades reflects the vertical offset of the magnetic antispring. This mismatch can be compensated by acting on the movable blades of the filter (see section 4.2).

From the collected data we can evaluate the actual working load supported by each blade and its stiffness around the working point. According to the design of the mechanical filter, we consider the working point of a blade the point where its tip

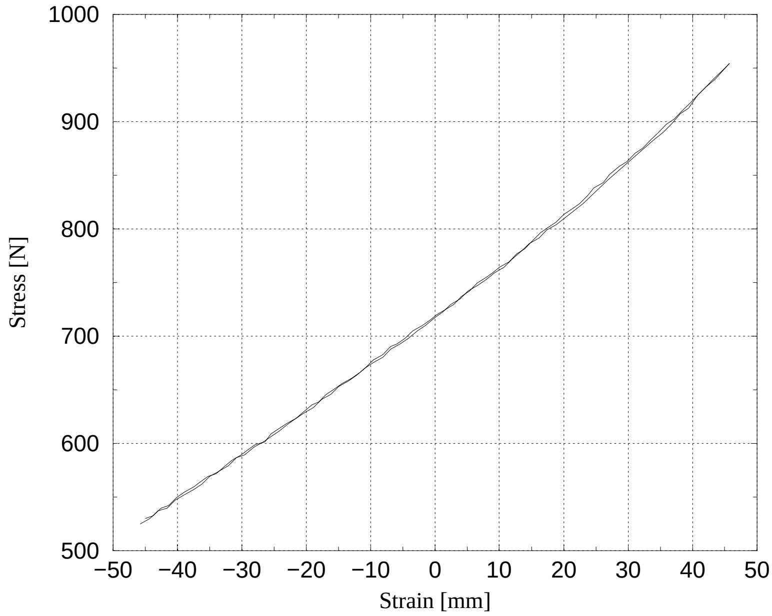

Figure 7.6: *Stress–strain curve of a blade spring as measured with the testing machine. The blade behaves as a vertical spring in a range of about 30 mm around the working point.*

lies on the plane defined by the support the blade is clamped to, i.e. the zero of our measurements. In fig. 7.6 the measured stress–strain curve of a blade is shown: the data refer to the last cycle of the fatigue test.

By means of a linear fit on the data in an interval of ± 10 mm around the zero strain, we estimate the value of both the actual load and the stiffness of the blade. The values are then recorded in a database (MS Access) and utilized in the assembling phase of the filters.

Chapter 8

VIRGO short towers

The installation of the VIRGO suspension systems started with the three short towers holding the far mirror of the mode cleaner cavity, the injection bench and the detection bench, respectively (see chapter 3). Since less seismic isolation is required, the short towers are composed only by the pre–attenuation top stage with a reduced inverted pendulum (2 m tall instead of 6 m) and by the steering filter suspending the last stage.

More than seismic attenuation, the short towers are aiming to provide an effective positioning system of the suspended items without introducing noise into the detection band of the interferometer. Although they are different from the full version, we can learn a lot by their installing and setting operations.

In this chapter we present a survey performed by the author on the dynamics of the first installed short tower: the one suspending the bench on which the far mirror of the mode cleaner cavity is mounted. For shortness, we will refer to this as the Mode Cleaner tower. The mechanical characteristics of the chain are measured on the apparatus in its working condition, apart from vacuum and thermal stabilization.

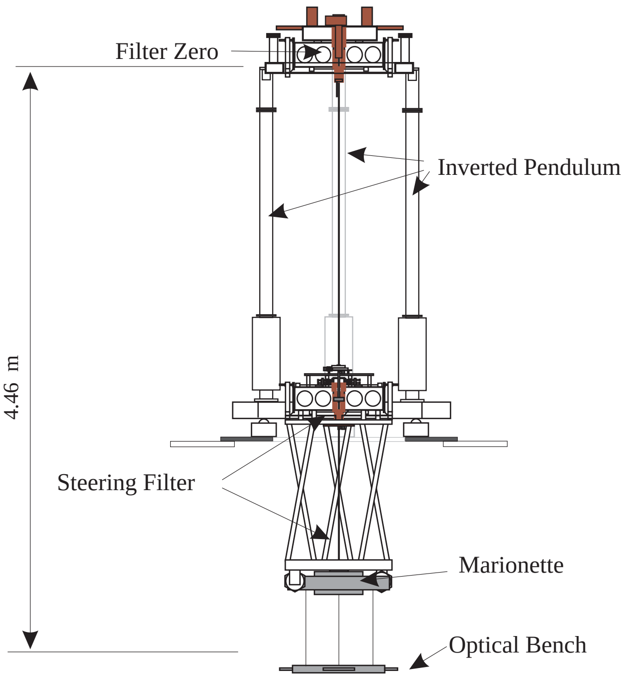

Figure 8.1: *The Mode Cleaner suspension system.*

8.1 Mode Cleaner

The Mode Cleaner is a triangular cavity 144 m long. Input and output mirrors are mounted on the input (or injection) bench, the far mirror is mounted on a suspended bench inside a vacuum chamber which is connected to the input bench by means of a dedicated vacuum pipe of reduced diameter. The finesse of the cavity is 1000 and its aim is to select the mode TEM_{00} from the laser beam before it is injected in the interferometer.

As shown in fig. 8.1, the Mode Cleaner suspension system is a short superattenuator consisting of only two mechanical filters: the filter 0 and the steering filter. A steel suspension wire links together the two mechanical filters and the marionetta to the steering filter. The marionetta is different from the one mounted on the tall tower since it has a circular shape. Also the steering filter is modified with respect to the one for the tall superattenuator: a structure extending from the bottom of the filter replaces the legs in supporting the driving coils which are eight instead of four. The coils, facing small magnets fixed to the outer circumference of the marionetta, are used to control the position and the angular alignment of the optical bench. The

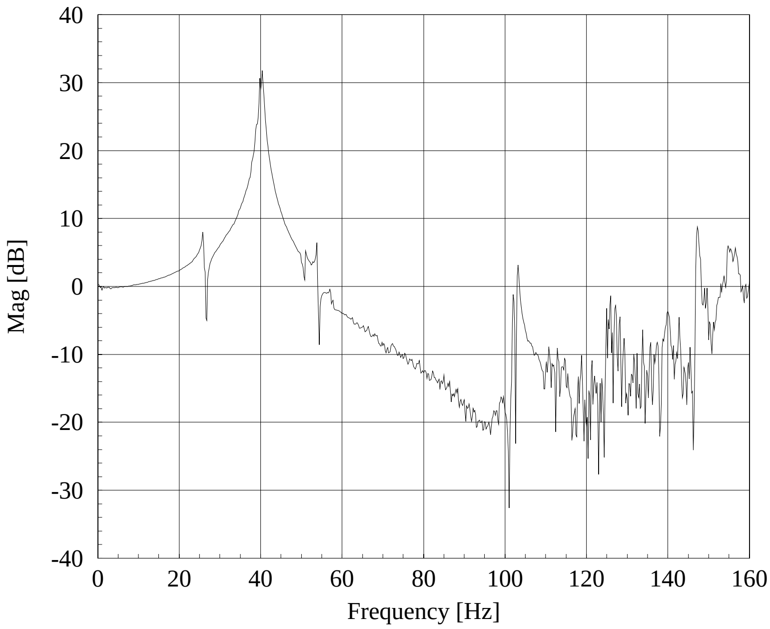

Figure 8.2: *Vertical transfer function marionetta → optical bench.*

optical bench which hosts the mirror is suspended to the marionetta by means of three steel wires. The filter 0 is supported by an inverted pendulum whose three legs are 2 m long. The survey on the mechanical characteristics of the chain has been performed by the author on the apparatus in its working condition, apart from vacuum and thermal stabilization.

By using commercial accelerometers (PCB – mod. 393B12) and a Spectrum Analyzer (Ono–sokki) we have been able to determine the normal modes of the chain and to check its attenuation performances. Four accelerometers have been positioned on the vessels of both the filter 0 and the steering filter, on the marionetta and on the optical bench, respectively. Vibrations have been injected by means of soft hammer blows and/or by driving the coil–magnet positioning device on the top stage of the chain.

8.2 Vertical dynamics

We have started with the measurement of the vertical transfer function (VTF) between 0 and 160 Hz of the last stage of the chain shown in fig. 8.2. Here we find

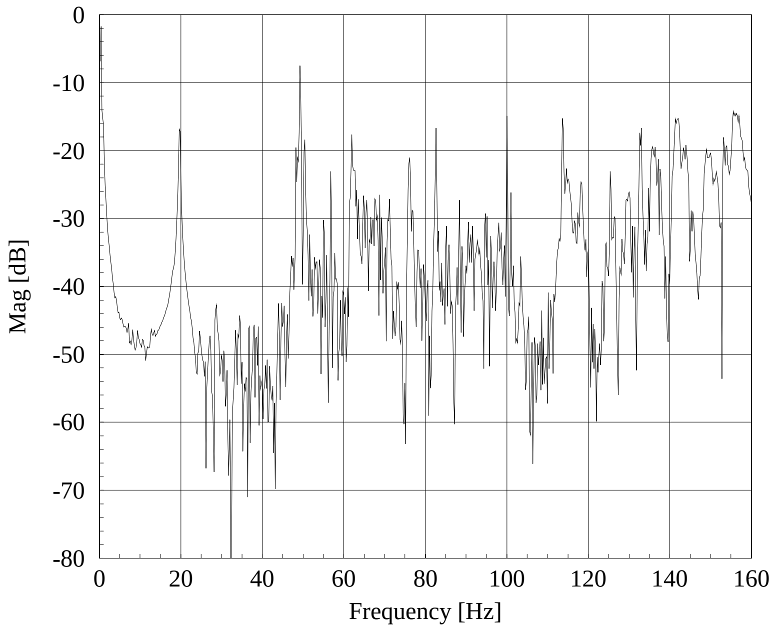

Figure 8.3: *Vertical transfer function steering filter → marionetta.*

a structured peak at 40 ± 0.2 Hz due to recoil of the optical bench against its three suspension wires acting as vertical springs. High order vibrational modes are present above 100 Hz. This means that, in the vertical direction, the system marionetta–optical bench behaves like a rigid object below 10 Hz. The VTF of the above stage, measured between the steering filter and the marionetta, (see fig. 8.3) shows the typical $\left(\frac{f_0}{f}\right)^2$ trend with $f_0 \simeq 400$ mHz due to the main vertical resonance of the blade springs+magnetic antispring of the steering filter; at 19.8 ± 0.2 Hz there is the crossbar mode of the steering filter (see chapter 5). Unfortunately, this VTF becomes less clean as the frequency increases because of loss of coherence between the signals of the two accelerometers, but we can still distinguish the zero–pole at about 40 Hz due to the resonance of the lower stage and the peak at 50 Hz of the same resonance, now coupled with the vertical modes of the steering filter. Multiplying the modules of these two VTFs we obtain the module of the VTF steering filter–optical bench shown in fig. 8.4 and compared with a direct measurement of the same one: the agreement is good, at least until the measurements are meaningful.

The problem of transferring vibration throughout one attenuation stage is crucial

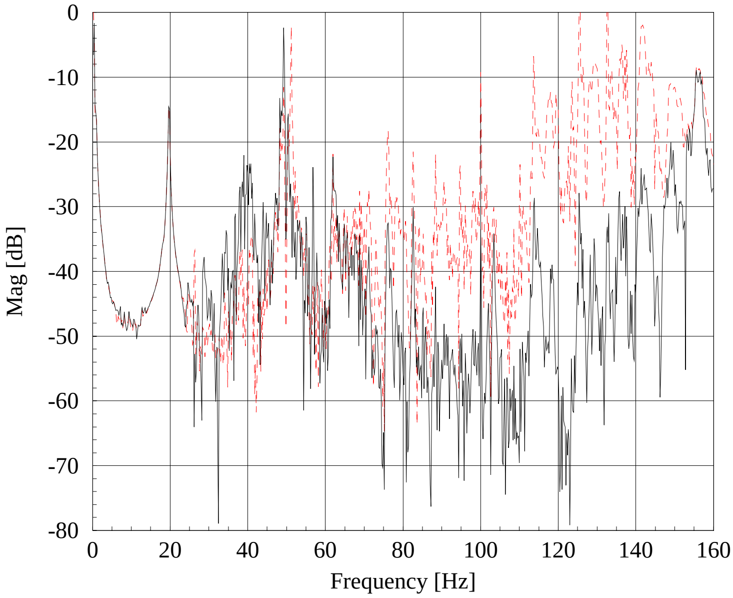

Figure 8.4: *Vertical transfer function steering filter → optical bench obtained by multiplying the modules of the single stage VTFs (solid line) compared with the measured one (dashed line).*

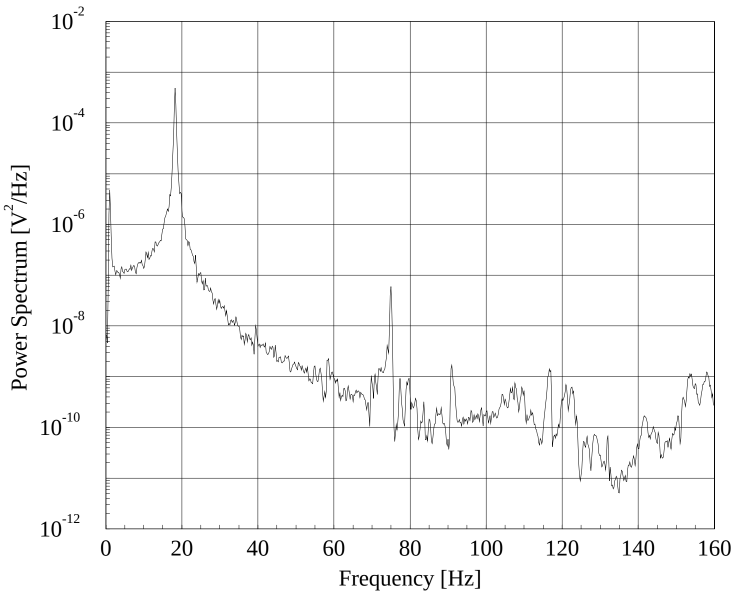

Figure 8.5: *Power spectrum of the accelerometer (in vertical direction) placed on the steering filter.*

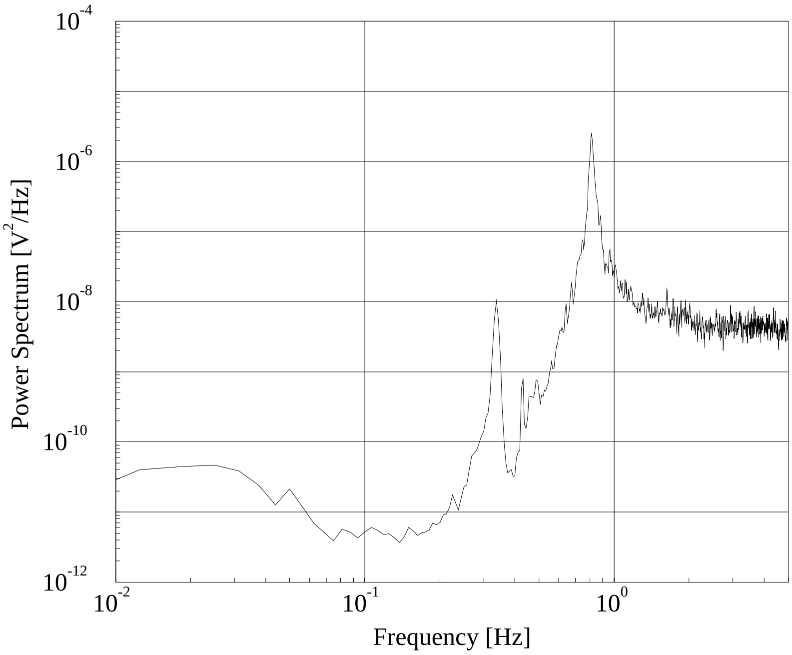

Figure 8.6: *Low frequency power spectrum of the accelerometer (in vertical direction) placed on the steering filter.*

in measuring the VTF between the filter 0 and the steering filter: we cannot sufficiently excite the upper filter to have on the lower one a good signal to calculate the transfer function. Anyway, by measuring the power spectra we can get information about the features of filter 0–steering filter stage. The power spectral density of the signal of the accelerometer placed on the vessel of the steering filter has been obtained by driving the vertical actuators of filter 0 with white noise. Through the coil–magnet system used as actuators we have injected vibrations on the crossbar of filter 0 so exciting the vertical modes of the chain. From the spectrum shown in fig. 8.5, we find that filter 0 has its crossbar mode at 18.2 ± 0.2 Hz.

At low frequencies, we find the two main vertical modes of the chain at 337 ± 6 and 812 ± 6 mHz, as it is evident in the power spectrum shown in fig. 8.6. This measurement has been done by injecting withe noise only in the frequency band from 0 to 2.5 Hz and avoiding to excite rotations around any horizontal axis (tilts). Since the accelerometer is placed quite far from the center of the vessel, it is sensible also to tilt movements. When tilts are excited (see fig. 8.7), three peaks one order of magnitude higher than the others, will appear at 431 ± 6, 756 ± 6 and 969 ± 6 mHz.

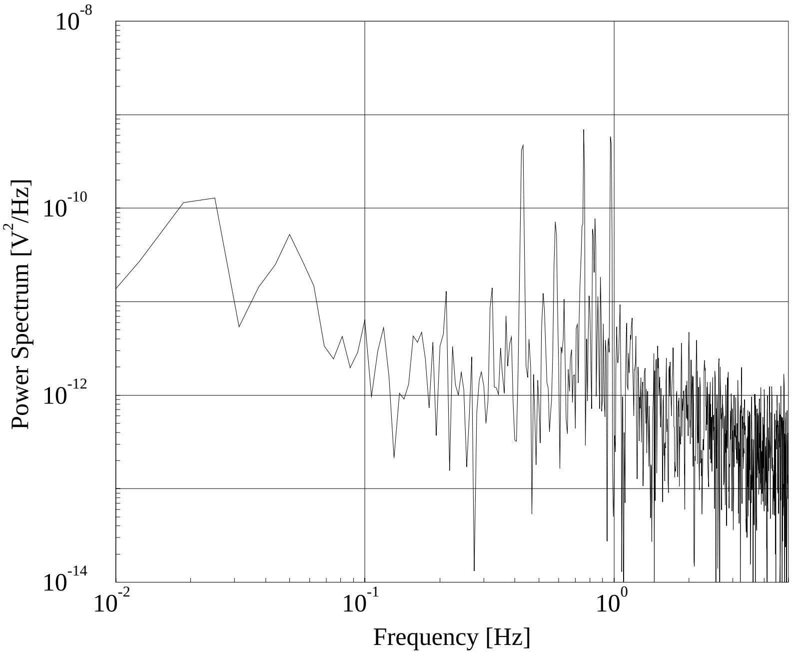

Figure 8.7: *Low frequency power spectrum of the accelerometer (in vertical direction) placed on the steering filter with tilt excited.*

It is difficult to say exactly which modes are responsible of these resonances because of strictly coupling between horizontal and tilt modes, as we will show below.

8.3 Horizontal dynamics

Following the scheme of the previous section, let us analyze the horizontal dynamics. In the horizontal tranfer function (HTF) steering filter–marionetta the structures due to the three suspension wires suspending the optical bench dominate the scene above 20 Hz (see fig. 8.8). Below this frequency the curve goes like $\left(\frac{f_0}{f}\right)^2$ with $f_0 \simeq 600$ mHz. The measurements are affected by the same problems as for the vertical ones, but we are confident that the general behaviour of the HTF, at least below 20 Hz, is readable from them. By multiplying the HTF filter 0–steering filter by the HTF steering filter–optical bench we obtain the HTF of the entire chain shown in fig. 8.9: an attenuation of $10^5 - 10^6$ is expected above 5 Hz.

At low frequency the power spectra of accelerometers exhibit the peaks of the main

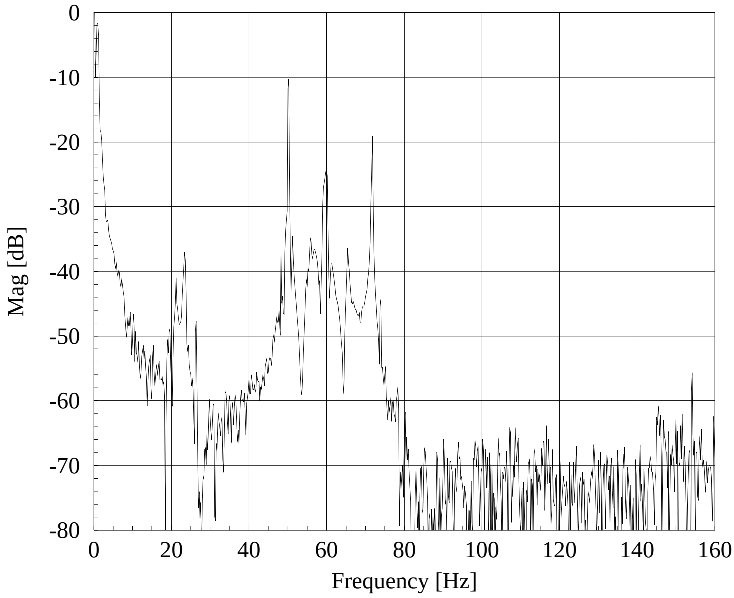

Figure 8.8: *Horizontal transfer function steering filter →marionetta.*

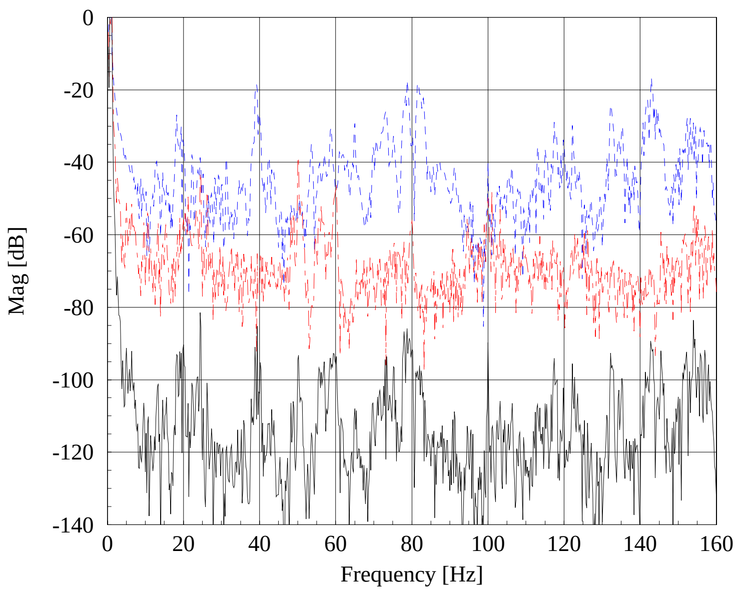

Figure 8.9: *Horizontal transfer function filter 0 → optical bench (solid line) obtained by multiplying the single stage HTFs which are also shown (dashed lines).*

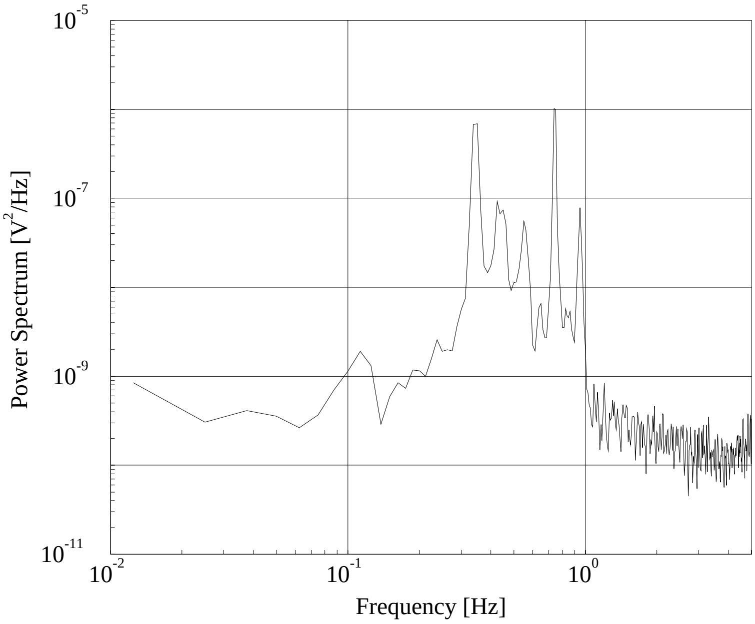

Figure 8.10: *Low frequency power spectrum of the accelerometer (in the horizontal direction) placed on the steering filter.*

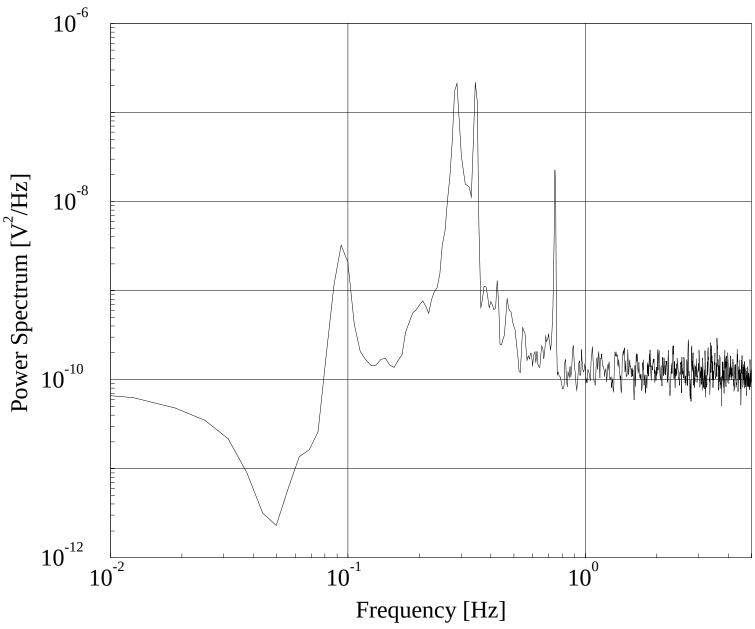

Figure 8.11: *Low frequency power spectrum of the accelerometer (in the horizontal direction) placed on the filter 0.*

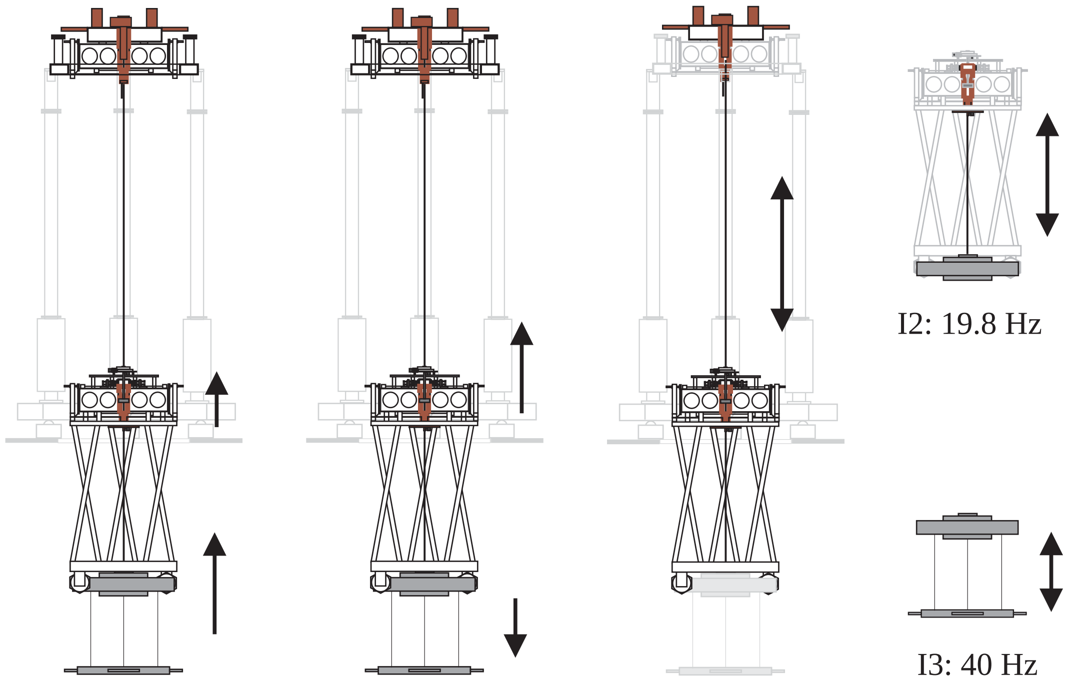

Figure 8.12: *Vertical modes*

modes of the chain. Three of the peaks in fig. 8.10 have frequencies very close to that of tilt mentioned above, so we attribute them to the coupling between horizontal and tilt motions. The remaining two resonances, at 350 ± 12 mHz and 550 ± 12, can be ascribed to a pure pendulum motion. The main resonance of the inverted pendulum at 94 ± 6 mHz is visible in the power spectrum of the accelerometer placed on the filter 0 (see fig. 8.11) where we also find a peak at 287 ± 6 mHz which misses in the spectra of the other elements of the chain. This peak is due to rotation of the filter 0 around the vertical axis against the return torque of the inverted pendulum.

8.4 Modes of the chain

The modal analysis of the superattenuator chain is very important for the electro–mechanics control of the system. The identification of the normal modes has been performed by using the measurements described above and by observing directly the motion of the chain elements. The short superattenuator tower can be regarded as a chain of six rigid bodies (2 filter bodies, 2 movable parts, marionetta and optical bench) connected by elastic elements (blade springs, suspension wires, centering wires). With a simple calculation (number of rigid bodies $\times$ number of degrees of freedom) we find that there must be 36 normal modes, without considering high order vibrational modes of the elastic elements; this number can be strongly reduced if we limit our analysis below ten Hz and we consider as rigid connections all the suspension wires (only in vertical direction) and the centering wires (only in horizontal directions). Assuming a cylindrical symmetry of the system the number of normal modes we have to identify is reduced to 12:

4 pendulum modes;

2 vertical modes;

2 rotations around a horizontal axis (tilt);

4 rotations around the vertical axis.

We can consider this 12 modes as the real *modes of the whole chain* and the others at higher frequencies as *internal modes of a single stage,* since the latter ones essentially involve just the two bodies connected by the elastic element (e.g. crossbar mode concerns a filter body and the movable part of the upper stage) inducing negligible displacement to the other items of the chain.

The shape of the vertical modes are sketched in fig. 8.12 where we also show the modes at higher frequency due to the suspension wires. In the mode V1 (@ 337 mHz) the steering filter, the marionetta and the optical bench move in phase; the steering filter moves in anti–phase with respect to the marionetta and the optical bench in the mode V2 (@ 812 mHz). The modes I1, I2 and I3 are due to the suspension wires acting as springs between the objects they connect.

From the measurements mentioned in previous sections, it is clear that there are modes involving pendulum motion as well as tilts and an exact description of such modes is hardly deducible. In fig. 8.13 we show our conclusions about pendulum and rotational modes after measuring, with a chronometer, the period of the following oscillations:

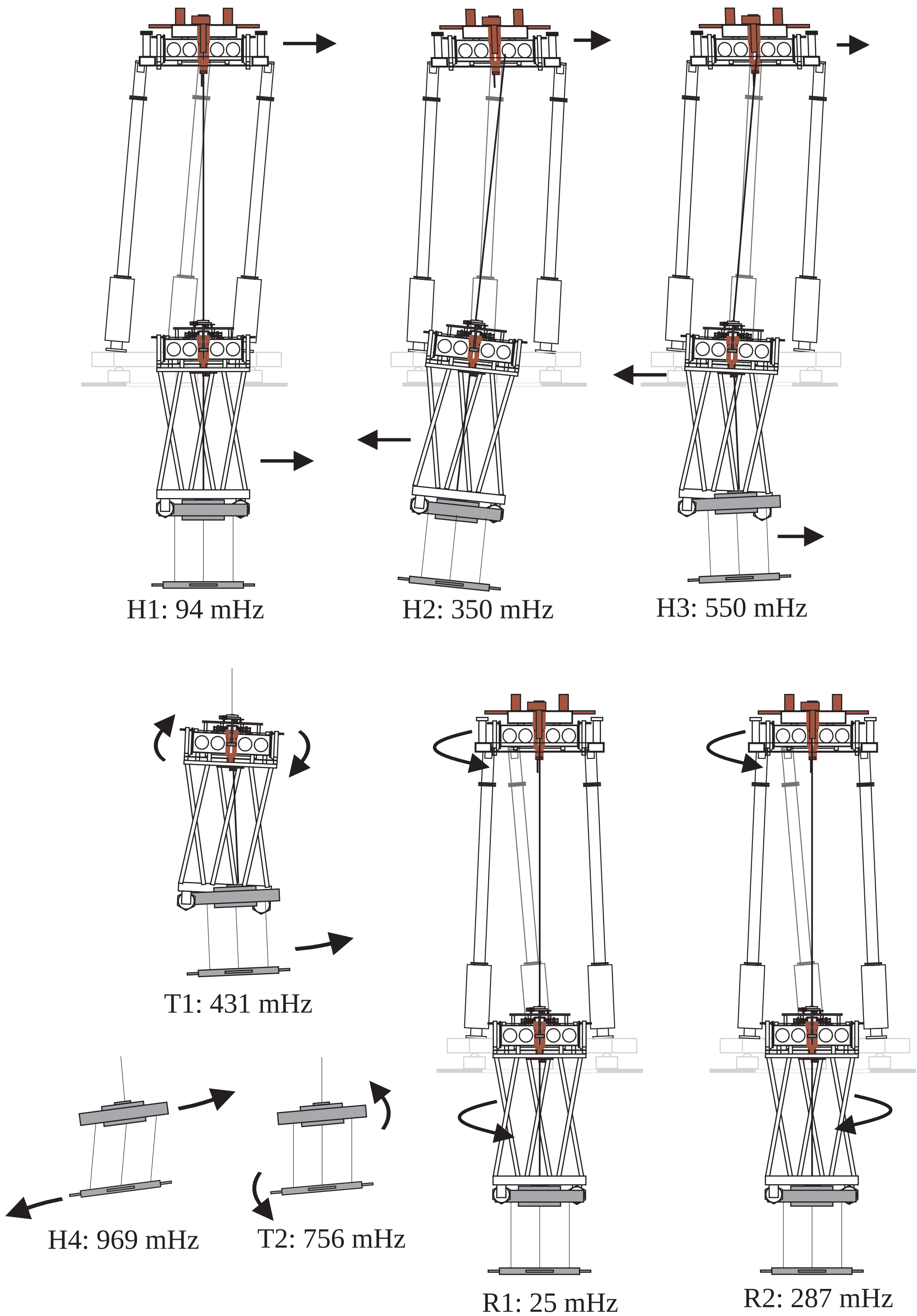

Figure 8.13: *Pendulum and rotational modes*

tilt of steering filter: 2.3 ± 0.05 s, 435 ± 10 mHz;

tilt of marionetta and optical bench in phase: 1.3 ± 0.05 s, 770 ± 30 mHz;

pendulum of marionetta and optical bench in anti–phase: 1.05 ± 0.05 s, 950 ± 45 mHz;

rotation of all the chain in phase: 40 ± 1 s, 25 ± 1 mHz.

The modes H1 (@ 94 mHz), H2 (@ 350 mHz) and H3 (@ 550 mHz) can be considered pure pendulum motion since their peaks appear only in the horizontal power spectra of the filter 0 and the steering filter. The peaks of modes T1 (@ 431 mHz), T2 (@ 756 mHz) and H4 (@ 969 mHz) are also present in the vertical power spectra, so they should involve both pendulum and tilt movements. The prefix H or T in the above classification means that they are "mainly due to" horizontal (pendulum) or tilt oscillations. For instance, the period of mode T1 is measured by tilting the steering filter but the recoil of the marionetta–optical bench seems to be a pendulum motion. Also the recoil of the filter 0 is horizontal because it cannot tilt.

For what concerns rotations around the vertical axis, we cannot see the mode in which the steering filter rotates in anti–phase with respect to the marionetta and the optical bench because the marionetta has a small rotational range: its rotation is limited by the coils mounted on the structure extending from the steering filter. The amplitude of permitted oscillations is not large enough to allow us to take a measurement of their period. For the same reason, we cannot say anything about the mode in which the marionetta and the optical bench rotate in anti–phase.

Chapter 9

Performances of the VIRGO superattenuators

In the previous chapters we have seen how to get rid of some limitations to the performances of the VIRGO superattenuator. In particular, we have described how to improve the attenuation through the magnetic antisprings so to obtain the seismic isolation starts from about 3 Hz (chapter 5). The internal vibrations due to the resonance of blade springs and suspension wires have been suppressed by means of passive dampers (chapter 6). Finally, in order to overcome the problem of creep, we have identified in the Maraging steel the best material for the realization of the most stressed components of the superattenuator (chapter 7).

In chapter 6 an indirect evaluation of the vertical transfer function of the superattenuator prototype has been produced. Apart from that indirect measurement, we will not be able to fully appreciate the performances of the superattenuator until the 3 km Fabry–Perot interferometer starts working, since it is the only instrument sensitive enough to measure the small residual motions of the suspended mirrors.

On the other hand, encouraging indications that the suspension specifications are fulfilled are deduced from analyzing the data coming from the *Central Interferometer* commissioning.

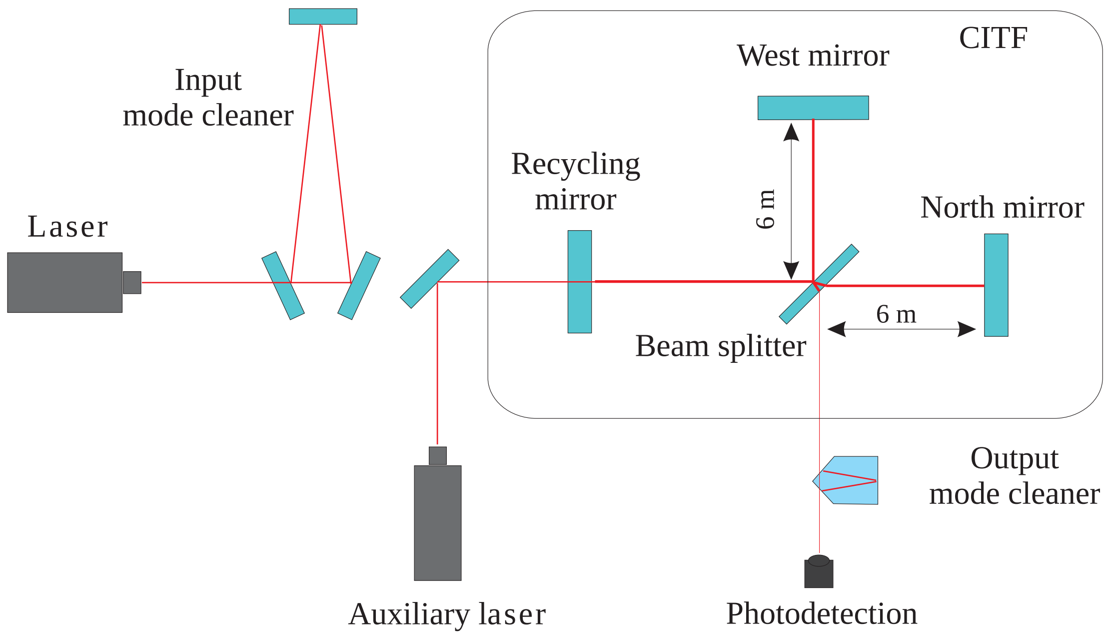

Figure 9.1: *Optical scheme of the Central Interferometer. In the first part of the commissioning phase, an auxiliary laser source was used, since a parallel commissioning was carried out on the injection system.*

9.1 The Central Interferometer

The Central Interferometer (CITF) is the 6 m recycled Michelson interferometer made up of the beam splitter, the recycling mirror and the input mirrors of the two Fabry–Perot cavities, used in this case as end mirrors (see fig. 9.1). All the components of the interferometer, used for the preliminary commissioning or the detector (injection system, vacuum system, electronics, mechanics, etc.), are nearly identical to the ones to be used in the final apparatus. The only important differences concern mirror dimensions (reduced size in the CITF) and specifications. A description of the CITF can be found in [64].

CITF (as well as VIRGO) works in feedback. This means that the interferometer is kept on the dark fringe and any deviation from the destructive interference induced by differential variations of the two arm lengths (or by optical noise) is compensated for by the feedback correction signal. In the CITF the compensation is made by moving the West mirror through the coils placed on the reference mass which act on the facing magnets fixed to the back of the mirror (see chapter 4.5). In absence of detectable gravitational signal, in the low frequency range where the feedback gain is high, the spectrum of West mirror compensation displacement is essentially the sensitivity of our apparatus. The full CITF has been successfully locked, achieving a displacement sensitivity around 10^{-16} m/$\sqrt{\text{Hz}}$ above 1 kHz, of a few 10^{-15} m/$\sqrt{\text{Hz}}$ at 100 Hz and of a few 10^{-13} m/$\sqrt{\text{Hz}}$ at 10 Hz.

9.2 Attenuation Performances

A measurement of the attenuation performance of the Superattenuator has been made by using the CITF. The measured upper limit of residual seismic noise at the mirror level turns out to be smaller than the thermal noise floor expected to limit the antenna sensitivity in the low frequency region.

Below a few tens of Hz (where seismic isolation is crucial), the displacement sensitivity of the CITF is not negligible (of the order of 10^{-13} m/$\sqrt{\text{Hz}}$), even if it is far from the sensitivity expected for VIRGO ($10^{-17} - 10^{-18}$ m/$\sqrt{\text{Hz}}$).

The measurement procedure consists of exciting the chain suspension point by sinusoidal forces in the low frequency range and using the interferometer to measure the residual excitation of the suspended mirror. As mentioned above, this can be measured by the feedback voltage applied to the reference mass coils of the West mirror in order to keep the interferometer locked on the dark fringe. The calibration between applied DC voltage and corresponding mirror displacement (about 12 μm per V) has been measured with an accuracy of a few percent[65]. A line in the spectrum of the reference mass coil voltage that has the same frequency as that of the excitation applied to the top stage can be attributed to compensation for a residual excitation that has been partially transmitted, throughout the suspension chain, to the mirror.

In the horizontal plane the top stage is excited by injecting current into the three coil–magnet actuators used for the inertial damping. The excitation lines are digitally set by using the client program to implement inertial damping digital filters. The three LVDT sensors and the three accelerometers provide two independent measurements of the displacement of the suspension point in the horizontal plane. The measurements by different sensors at frequency lines turn out to be equal with an accuracy of a few percent. On the contrary, the noise floor of the accelerometers is much smaller than the LVDT one in the interesting band.

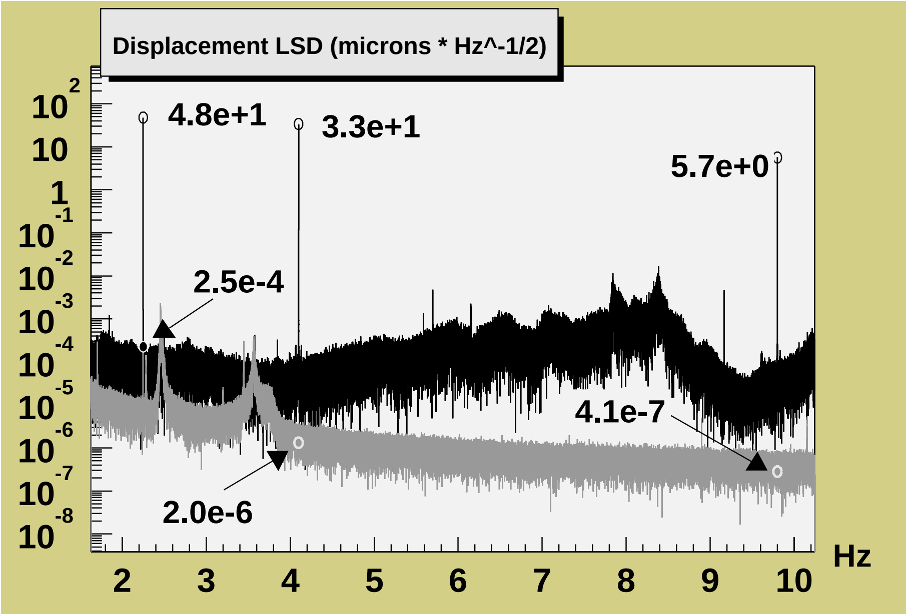

Figure 9.2: *Linear spectral density of the horizontal displacement along the beam direction of the chain suspension point, as measured by the top stage accelerometers (black line) and of the mirror (gray line). The two curves have been done using a 10485 s long data bench. The amplitudes of the three excitation lines (2.25, 4.1 and 9.8 Hz) are kept constant during all the acquisition time.*

The strategy to measure the effects of vertical vibrations on the interferometer is the same. The two coil–magnet actuators assembled on filter 0 are used to excite the suspension point of the filter chain in the vertical direction. Two accelerometers and an LVDT sensor monitor its vertical motion in three independent ways. Once again, the measurements by different sensors at the line frequencies are equal within an accuracy of a few percent, even if the noise floors are different.

9.2.1 Horizontal attenuation

The suspension point of the West chain was excited for a few hours along a given horizontal axis, with the CITF locked. Three lines at 2.25 Hz, 4.1 Hz and 9.8 Hz were applied at the same time with amplitudes of a few tenths of Volt, limited by the saturation of our sensors. The data coming from the top stage sensors were acquired at 50 Hz, while the correction voltage at the mirror level was acquired at 10 kHz and then decimated off–line at 50 Hz (after a steep anti–aliasing filtering). The linear

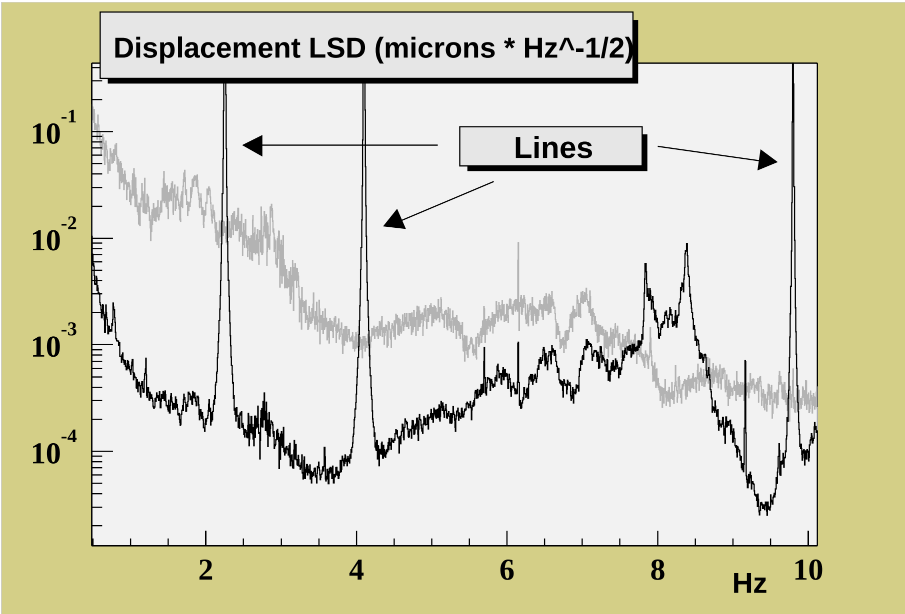

Figure 9.3: *Linear spectral density of the horizontal seismic displacement of the ground (gray line) compared with the linear spectral density of the horizontal seismic displacement of the top stage as measured by inertial damping accelerometers (black line). The spectra are averaged 10 times taking into account ten benches of about 166 s (corresponding to a frequency resolution of* $6 \cdot 10^{-3}$ *Hz). This procedure makes the noise floor much smoother with respect to the previous case.*

spectral density of the horizontal displacement of the suspension point along the beam axis is plotted in fig. 9.2, compared with the linear spectral density of the residual mirror displacement. It is important to remember that, while the linear spectral density of the noise floor is independent on the integration time, the linear spectral density at the frequencies where lines appear increases with its square root. In our case, where an integration time of 10,485 s has been considered (corresponding to a spectral bin width of $9 \cdot 10^{-5}$ Hz), only the line at 2.25 Hz can be detected at the mirror level. Due to the steep Superattenuator attenuation, the residual displacement at higher frequency lines is very small, below the CITF noise floor. At these frequencies, inside the VIRGO detection band, only upper limits of horizontal transmission can be provided.

Frequency (Hz)	*Top Displacement (m Hz$^{-1/2}$)*	*Mirror Displacement (m Hz$^{-1/2}$)*	*Transmission Top–Mirror*	*Transmission Specifications*
2.25	$4.8 \cdot 10^{-5}$	$2.5 \cdot 10^{-10}$	$5 \cdot 10^{-6}$	—
4.1	$3.3 \cdot 10^{-5}$	$\leq 2 \cdot 10^{-12}$	$\leq 6 \cdot 10^{-8}$	$< 1.5 \cdot 10^{-8}$
9.8	$5.7 \cdot 10^{-6}$	$\leq 4 \cdot 10^{-13}$	$\leq 7 \cdot 10^{-8}$	$< 1 \cdot 10^{-8}$

The two upper limits are sufficient to state that the residual seismic noise in the band is, in the worst case, of the same order of magnitude of the thermal noise floor. However, it is important to stress that, in our experiment, the excitation was applied to the filter chain suspension point. The inverted pendulum reduces the transmission of seismic vibrations from the ground to the chain suspension point, increasing the attenuation performance of the superattenuator. In fig. 9.3, horizontal ground seismic noise (measured by a commercial accelerometer fixed on the floor close to the suspension) and horizontal vibrations of chain suspension point are compared. One can see that an additional attenuation is provided at almost all frequencies. At only around 8 Hz (where flexural modes of the inverted pendulum legs induce peaks in the top stage displacement spectrum) this extra attenuation does not take place. Looking at the bins close to the excitation lines the reader can infer what is the typical horizontal seismic displacement of the chain suspension point at line frequencies (once the lines are switched off). Multiplying the value of the linear spectral density of the horizontal displacement of the chain suspension point (measured also when the lines are off) by the transmission upper limits listed in the previous table, one obtains:

Frequency (Hz)	*Top Displacement* (m Hz$^{-1/2}$)*	*Transmission Top–Mirror*	*Mirror seismic Displ.(m Hz$^{-1/2}$)*	*Mirror thermal Displ.(m Hz$^{-1/2}$)*
4.1	$7 \cdot 10^{-11}$	$\leq 6 \cdot 10^{-8}$	$\leq 4 \cdot 10^{-18}$	$9 \cdot 10^{-17}$
9.8	$9 \cdot 10^{-11}$	$\leq 7 \cdot 10^{-8}$	$\leq 6 \cdot 10^{-18}$	$< 9 \cdot 10^{-18}$

* *artificial line off.*

The upper limit for residual seismic noise at 4 Hz (i.e. at the beginning of the VIRGO detection band) is about a factor 20 smaller than the thermal noise floor. Since the superattenuator transmission is a steep function of the frequency, to put a so stringent limit at 4 Hz means to be confident that, at higher frequency, seismic noise is completely negligible (even if the upper limit put by our experiment at 10 Hz is of the same order of magnitude of thermal noise).

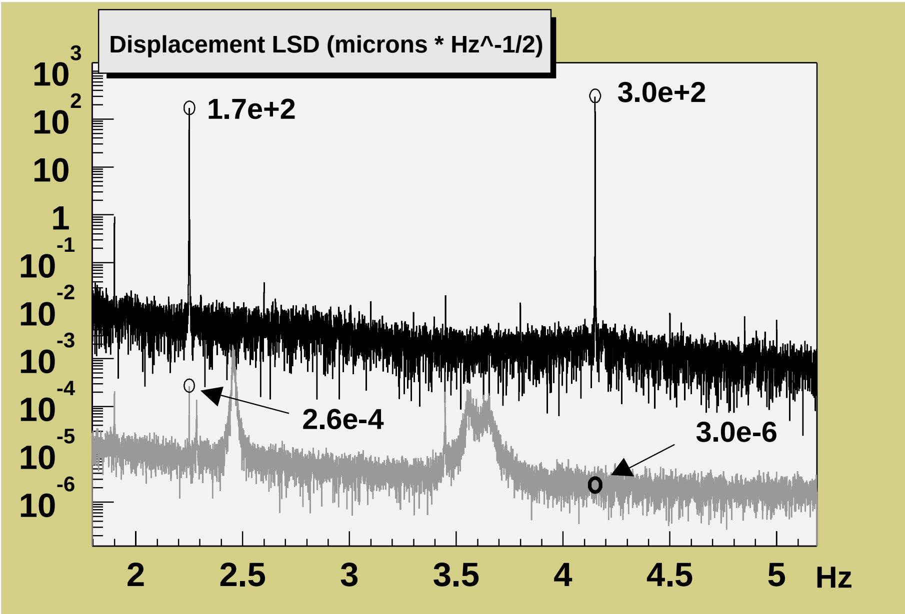

Figure 9.4: *Linear spectral density of the vertical displacement of the chain suspension point, as measured by the top stage vertical accelerometers, (black line) and of the mirror along the beam direction (gray line). The two curves have been obtained using a 2620 s long data bench with excitation lines at 2.25, and 4.15 Hz. The amplitudes of the excitation lines are kept constant during all the acquisition time.*

9.2.2 Vertical attenuation

According to the above argumentation, in the vertical experiment we have decided to concentrate almost all the allowable excitation on a line around 4 Hz (exactly 4.15 Hz). Our aim is to detect the line at the mirror level (or, at least, to put a more severe upper limit on the chain transmission). Another excitation line is placed at 2.25 Hz with a reduced amplitude, since the detection of this line at the mirror level is guaranteed by the not negligible transmission of filter chain at this frequency.

The linear spectral density of the vertical displacement of the suspension point is plotted in fig. 9.4, compared with the linear spectral density of the residual mirror displacement along the beam. The spectra has been computed on 2620 s (corresponding to a spectral bin width of $3.8 \cdot 10^{-4}$ Hz). The data are treated in the same way of the horizontal case. Despite our efforts, only the line at 2.25 Hz is transmitted to the mirror level enough to be detected. Since we are measuring mirror displacements along the beam axis, the vertical–horizontal coupling factor is already included in our

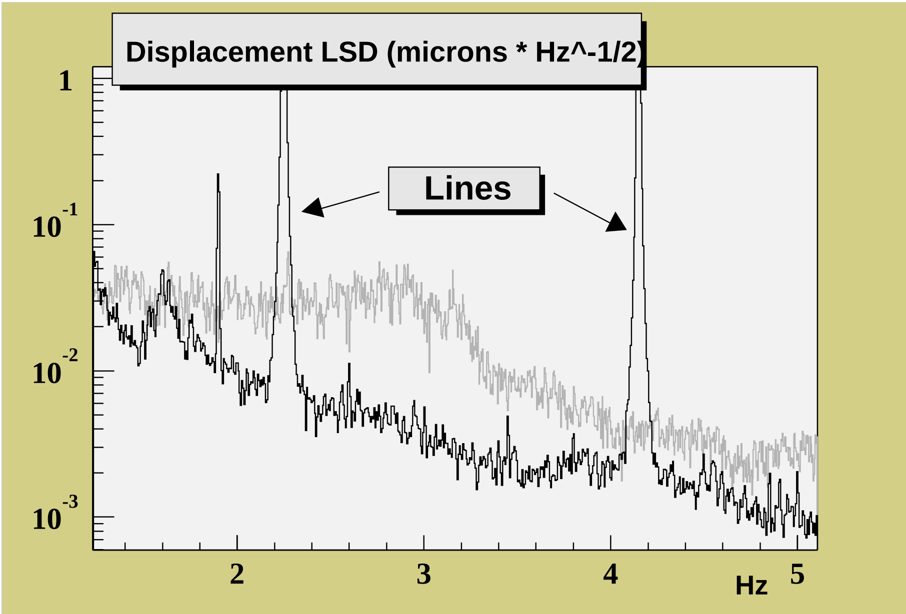

Figure 9.5: *Linear spectral density of the vertical seismic displacement of the ground detected by a commercial accelerometer placed on the floor close to the suspension (gray line) compared with the linear spectral density of the vertical seismic displacement of the chain suspension point as measured by inertial damping accelerometers (black line). The spectra are computed following the same procedure described in the caption of fig. 9.3.*

measurement. The results are:

Frequency (Hz)	*Top Vertical Displ.(m Hz$^{-1/2}$)*	*Mirror Horizontal Displ.(m Hz$^{-1/2}$)*	*Transmission Top(V)–Mirror(H)*	*Transmission Specifications**
2.25	$1.7 \cdot 10^{-4}$	$2.6 \cdot 10^{-10}$	$1.5 \cdot 10^{-6}$	—
4.15	$3.0 \cdot 10^{-4}$	$\leq 3.0 \cdot 10^{-12}$	$\leq 6 \cdot 10^{-8}$	$< 1.5 \cdot 10^{-8}$
9.85	$3.0 \cdot 10^{-5}$	$\leq 6 \cdot 10^{-13}$	$\leq 2 \cdot 10^{-8}$	$< 1 \cdot 10^{-8}$

* *Vertical–horizontal coupling factor included.*

The upper limit at 9.85 Hz has been placed by another dedicated experiment, with excitation energy concentrated around this frequency.

The upper limits are small enough to show that residual vertical seismic vibrations of the mirror, transmitted in the beam direction, are of the same order of magnitude of the thermal noise floor. Again, the attenuation of the pre–isolator stage has not been taken into account. However, in the vertical direction, the additional attenuation is not so large (see fig. 9.5), since we have just an additional mechanical filter (instead of the ultra–low frequency inverted pendulum). An upper limit of residual seismic noise in the interferometer is given by the product of the vertical seismic displacement of the chain suspension point (measured by the vertical accelerometers on the top stage) and the transmission upper limit just measured. The results are:

Frequency (Hz)	*Top Vertical* Displacement ($m\ Hz^{-1/2}$)*	*Transmission Top vertical – Mirror horiz.*	*Mirror seismic Hor. Displacement ($m\ Hz^{-1/2}$)*	*Mirror thermal Hor. Displacement ($m\ Hz^{-1/2}$)*
4.15	$2 \cdot 10^{-9}$	$\leq 10^{-8}$	$\leq 2 \cdot 10^{-17}$	$9 \cdot 10^{-17}$
9.85	$1 \cdot 10^{-9}$	$\leq 2 \cdot 10^{-8}$	$\leq 2 \cdot 10^{-17}$	$< 9 \cdot 10^{-18}$

** artificial line off.*

The seismic noise upper limit at 4 Hz is thus well below the thermal noise floor.

9.2.3 Low frequency vertical–horizontal coupling factor

The vertical–horizontal coupling factor has been estimated as follows: the vertical superattenuator dynamics in the frequency range of the resonances is well modeled by a chain of six point–like mass oscillators. The six masses (filters) and the six vertical stiffnesses (of the blade–magnet antispring system) are the model parameters. A direct accurate measurement of the filter masses was performed during the assembly operations. On the contrary, the spring stiffnesses cannot be well known a priori. Indeed, due to the complex magnetic antispring system, the stiffness strongly depends on the temperature and on the filter setting point (see chapteer 5). Once the tower is under vacuum these values can be different with respect to the open–air situation (where a direct measurement would be possible).

However, the six main frequencies of the chain normal modes can be measured accurately by the top stage accelerometers. Then, the exact values of the stiffnesses of the single filters, at the time of our vertical experiment, can be recovered by means of a numerical algorithm. The exact superattenuator vertical transfer function is estimated by inserting the values of the masses and of the stiffnesses in the SIESTA simulation code[41]. Taking into account all the superattenuator items, the simulation code computes the superattenuator transfer function at any frequency. Comparing the simulation results with the partial experimental data obtained by measuring the transfer functions on single stages (see section 6.4), an agreement between simulation and reality within 10% is provided.

The vertical transmission estimated by the simulation turns out to be $2.9 \cdot 10^{-5}$ at 2.25 Hz, while the measured vertical transmission (already multiplied by vertical–horizontal coupling factor) is $1.5 \cdot 10^{-6}$. The ratio of the last two numbers provides thus an estimate of the vertical–horizontal coupling factor of about 5%. Taking into account all error sources (calibration, simulation–reality agreement, precision of our measurement, etc.) an error of the order of ten percent can be assumed.

9.3 Mirror displacements along the beam

As discussed in section 4.1, dynamical limitations impose that the compensation displacement of the mirrors, to keep the interferometer on the dark fringe, cannot exceed one micron above 100 mHz. The linear spectral density of the compensation displacement along the beam direction, exerted on the West mirror to keep the CITF locked, has been measured and is plotted in fig. 9.6. The integral of the spectrum, providing the rms computed starting from a given frequency, is also shown.

The displacement compensating for residual differential motions of the interferometer mirrors, is induced by the correction currents driving the coils mounted on the reference mass. The measurement of the displacement has been done by monitoring the correction signal then, using a calibration factor of $5 \cdot 10^{-6} m/V$ for the voltage to displacement conversion, by multiplying the displacement by the transfer function of the system reference mass–mirror (a pendulum with a resonant frequency of 0.6 Hz).

The observed rms compensation displacement along the beam, in the band of the horizontal resonances (above 100 mHz) is found to be well below one micron. It is worth reminding that the locking of the CITF is made by sending the correction signal only on the reference mass actuators. When the three–stage control described in section 4.1 is performed, the very–low frequency motion will be compensated from the top of chain, while the active control at the payload level will be able to compensate for the small swing occurring above 100 mHz without injecting noise into the detection band.

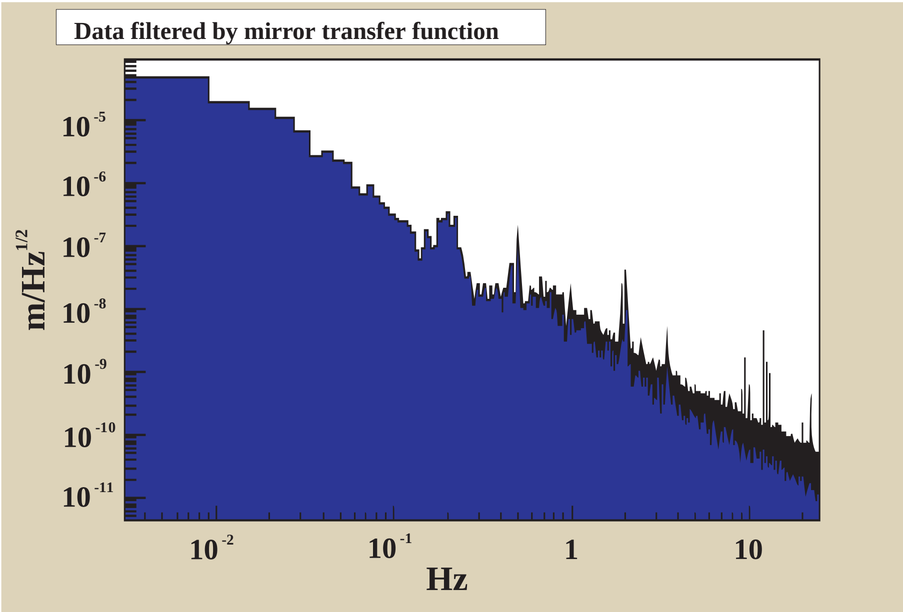

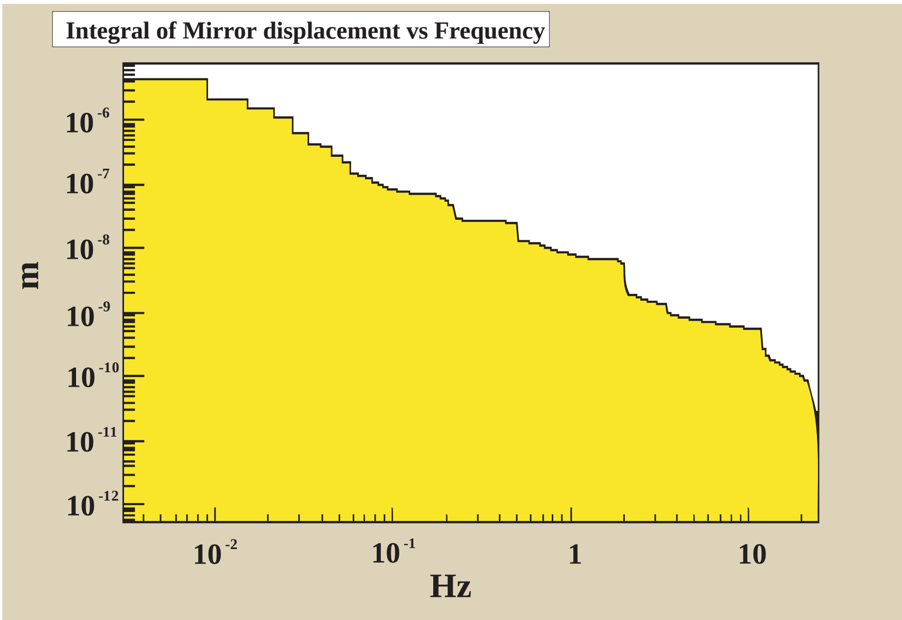

Figure 9.6: *Linear spectral density of the West mirror displacement along the beam direction (upper plot) and its rms computed starting from a given frequency (lower plot).*

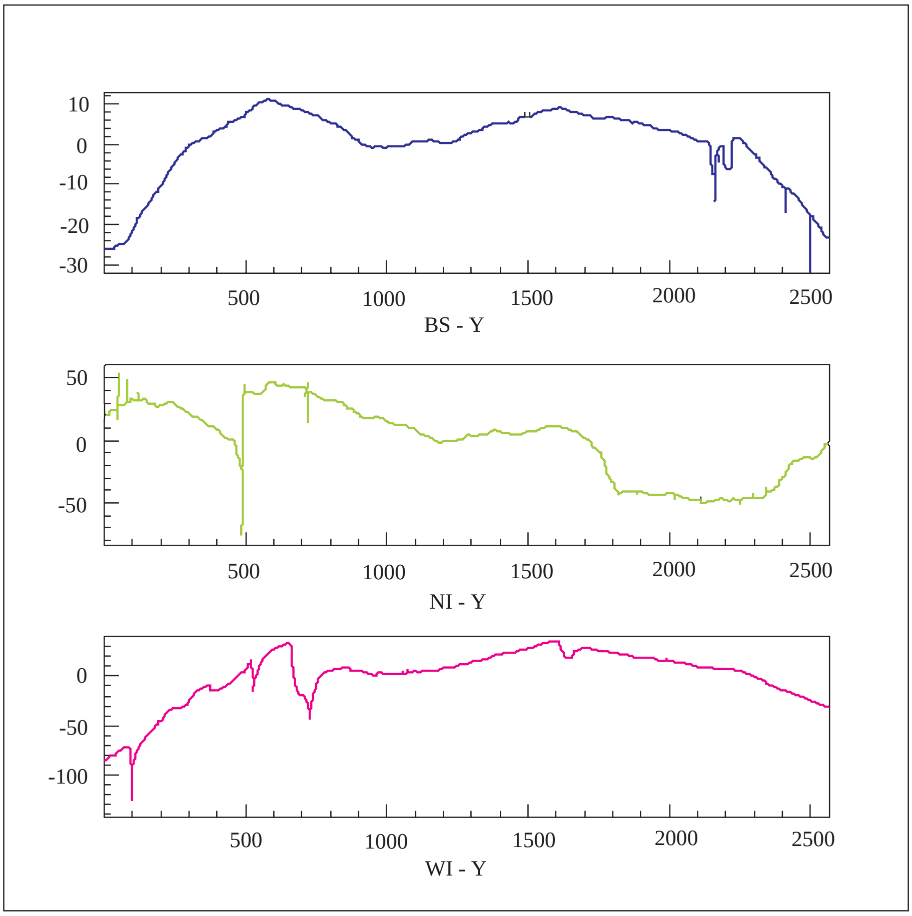

Figure 9.7: *From top to bottom, the vertical position (in μm) of the mirrors of the Beam Splitter, of the West Input and of the North Input tower. Each point is is the mean on 100 s of 1 Hz–sampled data.*

9.4 Mirror thermal drift

The VIRGO central building exhibits an excellent thermal stability. The suspensions, each located in a vacuum chamber experience small thermal excursions (around one tenth of degree peak to peak on time scales of days). The dependence of the mirror vertical position on temperature has been measured to be a few mm per Celsius degree, depending on the suspension under study. We remind that the thermal dependence of the vertical position of the mirror crucially depends on the vertical frequency of the chain mechanical filters, varying from one tower to the other. The vertical position of the mirrors of the Beam Splitter, of the West Input and of the North Input tower has been monitored for about three days by three CCD cameras, used for the angular control of the interferometer. The three time plots (expressed in microns) are displayed in fig. 9.7. Each point is the mean on 100 s of the mirror vertical position (acquired at 1 Hz). The offset values have been subtracted.

Conclusion

Here is a brief summary of the main results of this work.

- The magnetic antispring system has been fully characterized. The devices have been mounted and tuned on each VIRGO mechanical filter. Their effectiveness in lowering the main vertical resonant frequencies of the superattenuator has been proved.
- The dampers mounted on the VIRGO mechanical filters have been characterized. They suppress the filter internal modes to the required level.
- An indirect measurement of the vertical transfer function of the suspension prototype has been provided by combining the transfer functions measured on single stages. This preliminary measurement meets the specifications for the vertical seismic noise attenuation.
- The Maraging steel is a good solution to the creep problem. The best heat treatments for the components made of this material have been determined. The dislocation motion responsible of creep can be inhibited by applying to each blades a few load–unload cycles.
- The dynamics of the Mode Cleaner short tower has been experimentally studied and the main resonant modes of the chain have been measured.
- Exciting the suspension top stage around 4 Hz we have observed that the residual mirror motions is well below the Central Interferometer noise floor. This result allowed us to state that the VIRGO suspensions meet their main specification, i.e. that the residual seismic displacement of the mirrors along the beam is well below the thermal noise floor.
- Compensation displacements smaller than one micron on time scales of tens of seconds have to be applied on the West Input mirror to keep the Central Interferometer locked. This small values of the low frequency swing of the interferometer mirrors guarantee that it is possible to control the interferometer without injecting noise into the antenna detection band.

Bibliography

[1] C. Møller: *The theory of relativity*, Claredon Press, Oxford (1955)

[2] L.Landau, E.Lifshitz: *Theorie du Champ*, Editions de Moscou, Mosca

[3] C.W.Misner, K.S.Thorne, J.Wheeler: *Gravitation*, W.H.Freeman Eds., S. Francisco (1973)

[4] A.Einstein: *Ann. der Phys.*, **49**, 796 (1916)

[5] R.A.Hulse, *Rev. Mod. Phys.*, **66**, 699–710 (1994)

[6] J.H.Taylor: *Rev. Mod. Phys.*, **66**, 711–719 (1994)

[7] H.V.Shapiro, S.A.Teukolsky: *The physics of compact object*, J.Wiley & Sons Eds., New York (1984)

[8] K.S.Thorne: Gravitational radiation, in *300 years of gravitation*, S.W.Hawking, W.Israel Eds., Cambridge University Press, New York, cap 9, 330–458 (1987)

[9] K.S.Thorne: Gravitational waves from compact bodies, in *Proc. of IAU Symposium 165, Compact Stars in Binaries* (1995)

[10] J.H.Taylor et al.: *Astr. Journ. Supl.*, **88**, 529 (1993)

[11] D.G.Blair: Resonant–bar detector, in *The detection of gravitational waves*, D.G. Blair Eds., Cambridge University Press, New York, cap 4, 73–99 (1989)

[12] L.R.Forward: *Phys. Rev. D*, **17** (2), 379–390 (1978)

[13] A.Giazotto: *Physics Report A*, **182** (6), 367–424 (1989)

[14] W.Wincler: A Michelson interferometer using delay lines, in *The detection of gravitational waves*, D.G. Blair Eds., Cambridge University Press, New York, cap 11, 269–305 (1991)

[15] R.W.P.Drever: Fabry–perot cavity gravity–wave detectors, in *The detection of gravitational waves*, D.G. Blair Eds., Cambridge University Press, New York, cap 12, 306–328 (1991)

[16] J.Y.Vinet, B.Meers, C.N.Man, A.Brillet: *Phys. Rev. D*, **38**, 433–447 (1988)

[17] A.Brillet et al.: Advanced tecniques: recycling and squeezing, in *The detection of gravitational waves*, D.G. Blair Eds., Cambridge University Press, New York, cap 15, 369–405 (1991)

[18] M.Bernardini, S.Braccini, C.Bradaschia, C.Casciano et al.: *Class. Quantum Grav.*, **15**, 1–24 (1998)

[19] H.B.Callen, T.A.Welton: *Phys. Rev.*, **83** (1), 34–40 (1951)

[20] P.R.Saulson: *Phys. Rev. D*, **42** (8), 2437–2445 (1990)

[21] C.Zener: *Elasticity and anelasticity of metals*, University of Chicago Press, (1948)

[22] J.Y.Vinet et al.: *Phys. Rev. D*, **56**, 6085 (1997)

[23] A.Abramovici et al.: *Science*, **256**, 325 (1992)

[24] C.Bradaschia et al.: *Nuc. Instr. and Meth. A*, **289**, 518 (1992)

[25] A.Brillet et al. The VIRGO Project, *Proc. TAMA Workshop on Gravitational Wave Detection, 12–16 November 1996 (Saitama, Tokyo)* ed K.Tsubono (Tokyo: Tokyo University Academy Press) (1997)

[26] K.Danzmann et al.: *GE0600: Proposal for a 600 m Laser–interferometer Gravitational Wave Antenna* (Max Planck Institut für Quntenoptik internal report), MPO 190 (1994)

[27] K.Kuroda et al.: in *Proceedings of the 1st International Conference on GW: Sources and Detectors*, Eds: F.Fidecaro, I.Ciufolini, World Scientific, Singapore (1997)

[28] D.McClelland, D.G.Blair, R.J.Sandeman: AIGO: A Southern Hemisphere Second Generation Gravitational Wave Observatory, in *Proceedings of the 7th Marcel Grossmann Meeting on General Relativity* , Part B (Stanford Univ. July 1994), Eds: R.T.Jantzen, G.M.Keiser, Series ed. F.Ruffini, World Scientific Pub. Co, 1415–1417 (1996)

[29] W.M.Folkner et al.: LISA Mission Concept Study, *JPL Publication* 97–16 (1998); see also http://lisa.jpl.nasa.gov

[30] The Virgo collaboration: VIRGO Final Design(1997)

[31] R.Flaminio, H.Heitmann: *Phys. Lett. A*, **214**, 112-122 (1996)

[32] M.Punturo: The VIRGO sensitivity curve, *VIRGO internal report* VIR–NOT–PER–1939–51 (1999); see also http://www.virgo.infn.it/senscurve

[33] M.Beccaria, G.Cella, A.Ciampa, E.Cuoco, G.Curci, A.Viceré: *VIRGO internal report*, NTS 096/024 (1996)

[34] B.J.Meers: *Phys. Rev. D*, **38**, 2317–2326 (1988)

[35] K.A.Strain, B.J.Meers: *Phys. Rev. D*, **66**, 1391–1394 (1991)

[36] É.É. Flanagan: *Phys. Rev. D*, **48**, 2389 (1993)

[37] M.Maggiore: *High–energy physics with gravitational waves experiments*, gr–qc/9803028 (1998)

[38] B.Allen: The stochastic gravity wave background: sources and detection in *Proc. of the Les Houches School on Astrophysical Sources of Gravitational Waves*, Eds. J.A.Marck and J.P.Lasota, Cambridge University Press (1996)

[39] M.Gasperini: *String theory in curved spacetime*, World Scientific, Singapore (1998)

[40] G.Losurdo, M.Bernardini, S.Braccini, C.Bradaschia, C.Casciano et al.: *Rev. Sci. Instrum.*, **70** (5), 2507–2515 (1999)

[41] B.Callon et al.: *Astropart. Phys.*, **10**, 639 (1999)

[42] E.D'Ambrosio et al: *VIRGO internal report*, VIR–NOT–PIS–1390–129 (1999)

[43] M.Beccaria, M.Bernardini, E.Bougleux, S.Braccini, C.Bradaschia, C.Casciano et al.: *Nuc. Instrum. and Meth. A*, **394**, 397–408 (1997)

[44] C.Casciano: *La sospensione delle componenti ottiche di VIRGO: caratteristiche di attenuazione e sorgenti di rumore interno*, Tesi di Laurea, Pisa (1997)

[45] PHILIPS, Datsheet of Ferroxdure 330 (FXD 330), in *Handbook of PHILIPS Components* (1991)

[46] S.Braccini, C.Casciano, R.De Salvo, F.Fidecaro: On the stability of the superattenuator, *VIRGO internal report*, VIR–NOT–PIS–4600–031 (1996)

[47] S.Braccini, C.Casciano, R.De Salvo, F.Fidecaro: Temperature stabilization requirement of the VIRGO towers, *VIRGO internal report*, VIR–NOT–PIS–4600–032 (1996)

[48] S.Braccini, C.Casciano, R.De Salvo, F.Fidecaro: Elimination of the hydraulic adjustment of the filter suspension offset, *VIRGO internal report*, VIR–NOT–PIS–4600–026 (1996)

[49] S.Braccini, C.Casciano, R.De Salvo, F.Fidecaro, L.Holloway, G.Losurdo, J.Nicholas, F.Paoletti, F.Waharte: Damping properties of the vertical oscillations of the VIRGO superattenuator filters, *VIRGO internal report*, VIR–NOT–PIS–4600–109 (1996)

[50] S.Braccini, C.Casciano, R.De Salvo: Blades and crossbar dampers, *VIRGO internal report*, VIR–NOT–PIS–4600–108 (1996)

[51] G.Ballardin, L.Bracci, S.Braccini, C.Bradaschia, C.Casciano et al.: *Rev. Sci. Instrum.*, **72** (9), 3643–3652 (2001)

[52] A.S.Norwick, B.S.Berry: *Anelastic relaxation in crystalline solids*, Academic Press, New York (1972)

[53] D.Hull, D.J.Bacon: *Introduction to dislocations*, Pergamon Press (1983)

[54] J.P.Hirth, J.Lothe: *Theory of dislocations*, J.Wiley & Sons Eds, New York (1982)

[55] S.Braccini, C.Casciano, R.De Salvo,F.Paoletti, F.Fidecaro: Evidence of creep in the superattenuator mechanical filters, *VIRGO internal report*, VIR–NOT–PIS–4600–044 (1996)

[56] S.Braccini, C.Casciano, R.De Salvo, A.Gennai, L.Holloway, G.Losurdo, J.Nicholas, F.Paoletti, V.Rubino, F.Waharte: Measurements of creep on the mechanical filter blades: improvements with Maraging steel, *VIRGO internal report*, VIR–NOT–PIS–1390–087 (1997)

[57] M.Beccaria, M.Bernardini, S.Braccini, C.Bradaschia, G.Cagnoli, C.Casciano et al.: *Nuc. Instrum. and Meth. A*, **404**, 455–469 (1998)

[58] S.Malik, S.Braccini, R.De Salvo, A.Gennai,F.Paoletti, R.Valentini: Study of creep in maraging steel suspension wire, *VIRGO internal report*, VIR–NOT–PIS–4600–044 (1996)

[59] G.Cagnoli et al.: *Phys. Lett. A*, **237**, 21–27 (1997)

[60] S.Braccini, C.Casciano, F.Cordero, F.Frasconi, G.P.Gregori, E.Maiorana, G.Paparo, R.Passaquieti, P.Puppo, P.Rapagnani, F.Ricci, F.Ricci: *Phys. Lett. A*, **301**, 389–397 (2002)

[61] S.Braccini, C.Casciano et al.: *Meas. Sci. Technol.*, **11**, 467–476 (2000)

[62] F.Cordero, F.Corvasce, R.Franco, G.Paparo, E.Maiorana, P.Rapagnani, F.Ricci, S.Braccini, C.Casciano et al.: *Journal of Alloys and Compounds*, **310**, 400–404 (2000)

[63] S.Braccini, C.Casciano, V. Dattilo, R.De Salvo, G.T.Feng, F.Frasconi, G.Gennaro, R. Passaquieti, R.Valentini: Material tests for the suspension subsystem, *VIRGO internal report*, VIR–TRE–PIS–4600–129 (1997)

[64] F.Acernese et al.: *Class. Quantum Grav.*, **19**, 1421 (2002).

[65] R.Flaminio et al.: Calibration Investigation, *VIRGO internal report*, VIR–NOT–LAP–1390–204 (2002)

[66] S.Braccini: Measurements of suspension performances, *VIRGO internal report*, VIR–NOT–PIS–1390–191 (2002)

Acknowledgments

First, I want to thank Stefano Braccini, Franco Frasconi and Roberto Passaquieti, their scientific support and their friendship have been fundamental for me.
Thanks to Adalberto Giazotto.
Thanks to all the Pisa VIRGO group, especially to the people of the Suspension group for their support.
Thanks are due to Mario Favati, Federico Paoletti and Furio Vignoli for their helpful technical assistance.
Finally, thanks to my family to which I dedicate this work.